January 2015

Design of an Embedded Fluorescence Imaging System for Implantable Optical Neural Recording

Giovanni Barbera
Purdue University

Graduate School Form 30
Updated 1/15/2015

PURDUE UNIVERSITY
GRADUATE SCHOOL
Thesis/Dissertation Acceptance

This is to certify that the thesis/dissertation prepared

By Giovanni Barbera

Entitled

Design of an Embedded Fluorescence Imaging System for Implantable Optical Neural Recording

For the degree of Doctor of Philosophy

Is approved by the final examining committee:

Prof. Eugenio Culurciello
Co-chair

Prof. George T.C. Chiu
Co-chair

Dr. Da-Ting Lin

Prof. Justin Seipel

To the best of my knowledge and as understood by the student in the Thesis/Dissertation Agreement, Publication Delay, and Certification Disclaimer (Graduate School Form 32), this thesis/dissertation adheres to the provisions of Purdue University's "Policy of Integrity in Research" and the use of copyright material.

Approved by Major Professor(s): Prof. Eugenio Culurciello

Approved by: Prof. Anil Bajaj 10/16/2015

Head of the Departmental Graduate Program Date

DESIGN OF AN EMBEDDED FLUORESCENCE IMAGING SYSTEM FOR IMPLANTABLE OPTICAL NEURAL RECORDING

A Dissertation

Submitted to the Faculty

of

Purdue University

by

Giovanni Barbera

In Partial Fulfillment of the

Requirements for the Degree

of

Doctor of Philosophy

December 2015

Purdue University

West Lafayette, Indiana

To my family

TABLE OF CONTENTS

LIST OF TABLES

LIST OF FIGURES

Figure Page

Figure Page

Figure Page

Figure Page

ABSTRACT

Barbera, Giovanni. PhD, Purdue University, December 2015. Design of an Embedded Fluorescence Imaging System for Implantable Optical Neural Recording. Major Professors: George T.C. Chiu, School of Mechanical Engineering and Eugenio Culurciello, Weldon School of Biomedical Engineering.

The brain is the most complex and least understood biological system known to man. New imaging techniques are providing scientists with an entirely new perspective on the study of the functional brain at a neural circuit level, enabling in-depth understanding of both physiological processes and animal models of neurological and psychiatric diseases which currently lack effective treatments. These new tools come at the cost of meeting the challenges associated with the miniaturization of the hardware for *in vivo* recordings

Here we propose a miniaturized wearable device which enables to record neuronal activations with single cell resolution in rodents for *in vivo*, long term studies of neural activity in virtually any region of the brain.

Additionally, we introduce new techniques for processing a new set of data and mining the relevant information from the recorded neural activity. The proposed image preprocessing techniques include image registration, automatic cell detection and calcium transient extraction algorithms designed for real-time hardware implementation, anticipating the application of single cell neural recordings jointly with optogenetic stimulation in a feedback control loop.

The new developed tools were applied to the study of the neural activity in the direct and indirect pathways on the dorsal striatum and their role in locomotor activity, a controversial topic due to the lack of techniques for selectively and independently study these neural circuits with sufficient detail. Our findings challenge the long standing classical model for D1 and D2 neurons, showing how neural activity in the

indirect pathway cannot be explained as inhibitory for locomotor activity. Through the application of a k-means based clustering algorithm we propose a new model for the direct and indirect pathway role in locomotion, and demonstrate the remarkable heterogeneity in striatal D1 and D2 cell populations. The study of acute cocaine effect as a mean for pharmacologically increase locomotor activity further proved the diversity in the response of D1 and D2 neurons within the same cell population.

Finally, through the application of machine learning algorithms, we show how neural activity in the dorsal striatum (particularly D2 neurons) can be used as a good predictor for behavior in open field tests.

1. INTRODUCTION

Recent advances in the fields of Bioengineering, Optics and Neuroscience are enabling scientists to approach the study of the brain at a neuronal circuit level in novel ways [1–3], offering new tools for untangling the intricate mechanisms relating specific neural activity patterns with their behaviorally relevant function, with the ultimate goal of finding more effective solutions to many neurological and psychiatric diseases which still lack effective treatments.

1.1 Brain Imaging Techniques

Traditionally the main approach adopted for recording and stimulating neural circuits is through the use of microelecrodes, which are suitable for capturing the high firing rate (up to kHz), low voltage signals typical of neural action potentials (APs). Multi-Electrode Arrays (MEAs) however suffer intrinsic limitations, particularly due to the inability of electrical recording and stimulation to target a specific family of neurons, as the electrical signal propagates in a broad region around the electrode insertion site, affecting simultaneously heterogeneous families of neurons. Furthermore, implanting electrodes in the brain is invasive (it damages the tissue under study), and the quality of the signal degrades overtime.

Non invasive imaging techniques which allow a full three-dimensional monitoring of brain metabolism are functional magnetics resonance (fMRI) and positron emission tomography (PET), however they suffer from major limitations, as they only provide indirect measurement of neural activity, they lack in both spatial and temporal resolution, and they required head fixation.

The development of genetically encodable neural indicators and actuators [4–7] are laying the basis for novel optical imaging techniques, such as optogenetic stimulation, voltage sensitive dye imaging (VSDI) and calcium imaging, which are less invasive in that they do no require penetration of the cell membrane, and yet they provide a mean of investigating the dynamics of large number of cells down to single neuron, single action potential resolution.

1.1.1 Voltage Sensitive Dyes

VSDI is a well established technique in Neuroscience [8–10], showing two particularly desirable properties for the study of neural activity: the molecules of the voltage sensitive dye bind to the external surface of the membrane without penetrating the cell or altering its function, and the variation in the optical signal generated, which changes linearly with the area of the membrane of all stained cells [11], has a fast dynamics, with micron spatial resolution and sub-millisecond precision [12], which make them suitable for measuring single action potentials [10, 13].

Nonetheless several challenges need to be faced in the recording of the fluorescence signal: even though the change in membrane voltage are fairly substantial (in the order of 100mV), the intensity of the electric field decreases exponentially moving away from the membrane due to the dielectric screening of the surrounding polarized material [14], thus a displacement of even few nanometers of the voltage sensitive molecule could have a detrimental effect on the measured change in potential. Also, VSDs often require a strong light source in order to produce detectable changes in fluorescence, and this can produce oxygen free radicals which might damage the membrane and kill the cell. Additionally, most VSD molecules have a charge, and their placement on the membrane can alter its electrical properties. Even worse, many VSD can cause pharmacological side effects and can have considerable toxicity for the neuronal cells [15].

1.1.2 Calcium Imaging

Calcium sensitive dyes (CSDs) are used to monitor the intracellular calcium level [10, 16–18], which in neurons is a fundamental messenger related to several key processes such as action potentials. Since the development of the first calcium probes [16] there has been an ongoing improvement which led to the first generations of fluorescent calcium indicators quin-2 [16] and fura-2 [17], which significantly improved the change in fluorescence and allowed for quantitative measurements of the intracellular calcium levels. In 1997 protein-based genetically encoded calcium indicators (GECIs) were introduced [19], allowing the creation of transgenic mice expressing the indicator in specific cellular subtypes.

Despite some limitations related to the use of calcium dyes (e.g. they are not direct indicators of action potentials, their dynamics is slower compared with VSDs [13], and they can act as a buffer for intracellular calcium level [20]), calcium imaging is still widely adopted for in vivo brain imaging: consistent long-term measurements of the dynamics of wide-field GECIs are reported in [21] and [22] for anesthetized mice. Laser scanning methods (confocal or two-photon microscopy) are traditionally used to monitor neuronal activity in deeper regions of the brain [23], but these techniques are limited to the low bandwidth of the scanning method.

Recent advances in the instrumentation for calcium signals detection led to the development of miniaturized microscopes for tethered in vivo experiments in behaving animals using a miniature epifluorescence microscope [24–27] and a miniature MEMS based two-photon microscope [28]. With the present work we seek to push forward the scope of feasible in vivo experiments in fully unconstrained behaving animals with the introduction of a miniaturized, untethered, self-contained and mass-producible brain imaging system.

1.1.3 CMOS Image Sensors

The significant improvements in CMOS technology over the last decade [29] are opening the way to new generations of low power, miniature imagers, already widely employed in mobile devices and cameras, whose image quality and noise figures are fast approaching the ones of their larger, power-hungry counterpart, CCD image sensors. The dramatic improvement in the noise performance of CMOS imagers is due to the introduction of two main design concepts in the pixel architecture: the active pixel sensor (APS) [30, 31] and the pinned photodiode (PPD) [32, 33].

The APS (Fig. 1.1a) was made possible by advances in microlithography techniques in the early 1990's, which allowed one or more active elements to be integrated in the pixel, typically 3 − i.e. source follower, reset gate and selection gate −. The main advantage of this pixel architecture is that the charge of the photodiode is buffered in the source follower transistor, whose voltage can be read in a non-destructive way. This introduces multiple benefits compared with the passive pixel architecture, firstly because the active transfer of the charge from the photodiode to the source follower transistor significantly reduces the readout time and suppresses

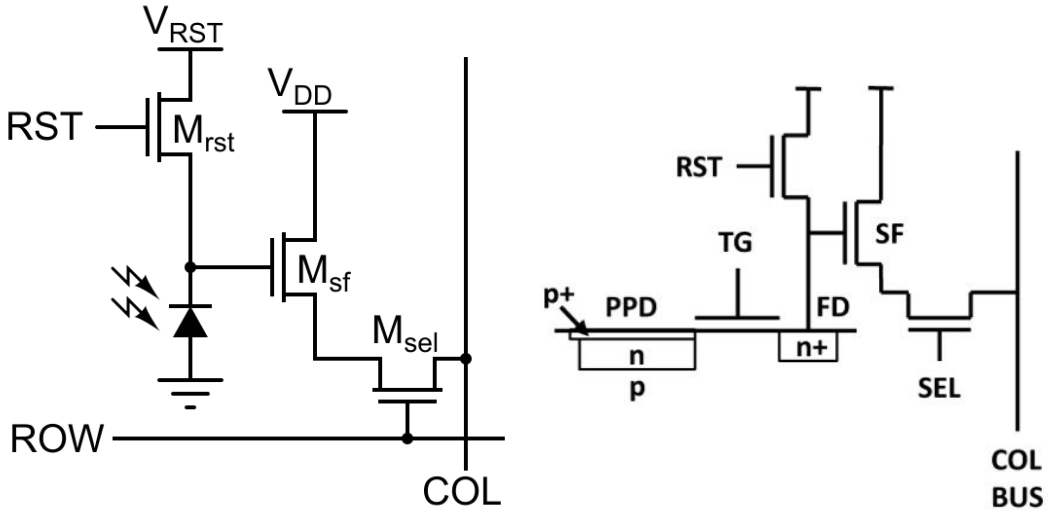

(a) (b)

Figure 1.1. (a) 3T APS. (b) 4T APS with pinned photodiode [33].

the noise generated in the readout circuit; secondly, it allows to use correlated double sampling (CDS), which suppresses the reset noise (and reduces fixed pattern noise) by sampling the charge of the photodiode twice and taking their difference.

The pinned photodiode APS (Fig. 1.1b), also referred to as 4T APS for the introduction of a fourth transistor, the transfer gate, became de facto the standard for most pixel architectures as it considerably reduces the dark current compared with the 3T pixel. The introduction of the transfer gate separates the floating diffusion node from the photodiode, allowing for true correlated double sampling and fixed pattern noise reduction. Pixel is reset by turning on both the reset gate and the transfer gate, setting both the floating diffusion and the photodiode to V_{DD} level. The photodiode starts to integrate the charge as soon as the transfer gate is turned off, separating it from the floating diffusion node. Then the readout phase starts by toggling the reset gate on and off to reset the floating diffusion, whose voltage level (reset level) is immediately transferred to the source follower and stored in the column circuit; at this point the photodiode charge (signal plus reset level) is also buffered on the source follower by turning on the transfer gate and stored in the column circuit. The difference of these two values give the true signal value, suppressing the reset noise and reducing the FPN. The use of the pinned photodiode provides a potential barrier to protect the signal from surface defect noise, lowering significantly the dark current and enabling a full charge transfer to the floating diffusion area thus avoid lag in the image.

1.2 Goals and Contribution

The final goal of this work is to produce a fully working miniature device for in vivo fluorescence imaging, to be applied, along with novel image processing tools, to biologically relevant issues. A miniature microscope and a tethered and untethered data acquisition system were designed and tested with both in vitro and in vivo exper-

iments, showing capabilities which approach the performance of bench top imaging systems.

The system has then been used to study neural activity in the dorsal striatum, and the implementation of novel data analysis and image processing techniques has allowed to study with unprecedented detail the role of direct and indirect pathway in locomotor activity. The introduction of a k-means based clustering algorithm and machine learning methods for neural data analysis have demonstrated for the first time the functional diversity of neurons in the dorsal striatum, which suggests an organization in spatially and functionally compact clusters with heterogeneous activity. These findings challenge the classical rate-based model of the direct and indirect pathways and indicate the need for an in depth study at a single cell level of these neural circuits for a better understanding of their joint physiological function and their role in locomotor activity.

2. DESIGN OF A MINIATURE HEAD-MOUNTABLE IMAGING SYSTEM

The imaging system consists of a miniature epifluorescence microscope, a CMOS image sensor, LED light source and data acquisition system. The final goal of this thesis is to develop a miniaturized wireless system which can be worn by the animal without any type of constraint and with minimal burden for the rodent. This will significantly expand the range of possible behavioral experiments, which currently suffer major limitations from the device being tethered or too bulky to be worn by small rodents.

2.1 Microscope

Three different epifluorescence microscope prototypes were tested (only the third one is presented here), in order to minimize size and weight, to reduce autofluorescence and to allow for a more accurate positioning of the optics. The last prototype weights 2.4g and measures 14mmx15mm (on the image sensor side) and 23mm overall height. Both the top and bottom sides of the microscope are threaded to allow for adjustments of the GRIN lens and imaging plane. Initial prototypes were 3d printed in RenShape SL 7820 black resin (25μm precision), but additional coating was necessary to reduce autofluorescence; the final prototype was manufactured in aluminum with direct metal laser sintering to eliminate this issue.

2.1.1 Optical Pathway

The blue light emitted by the LED (Cree XLamp XPEBLU-L1-0000-00Y01, 465nm-485nm) is focused with the collimating lens, filtered by the excitation filter, which proved to be necessary after initial testing (Pixelteq CO674-43 bandpass filter, 426nm ± 50nm, 3mmx3mmx1.1mm), and directed to the GRIN lens and the specimen by the 45° dichroic mirror (Semrock FF495-Di03, 5mmx5mm). The emitted light which passes through the dichroic mirror is then filtered by the emission filter (Pixelteq 102386376 bandpass filter, 510nm ± 20nm, 3mmx3mmx1.1mm) and focused on the imaging plane by the achromatic lens (Edmund Optics #63-690). The CAD design of the microscope and an image of the aluminum prototype are shown in Fig. 2.1. With a 500μm GRIN lens (NEM-050-06-08-520-DS) the field of view is 160μ.

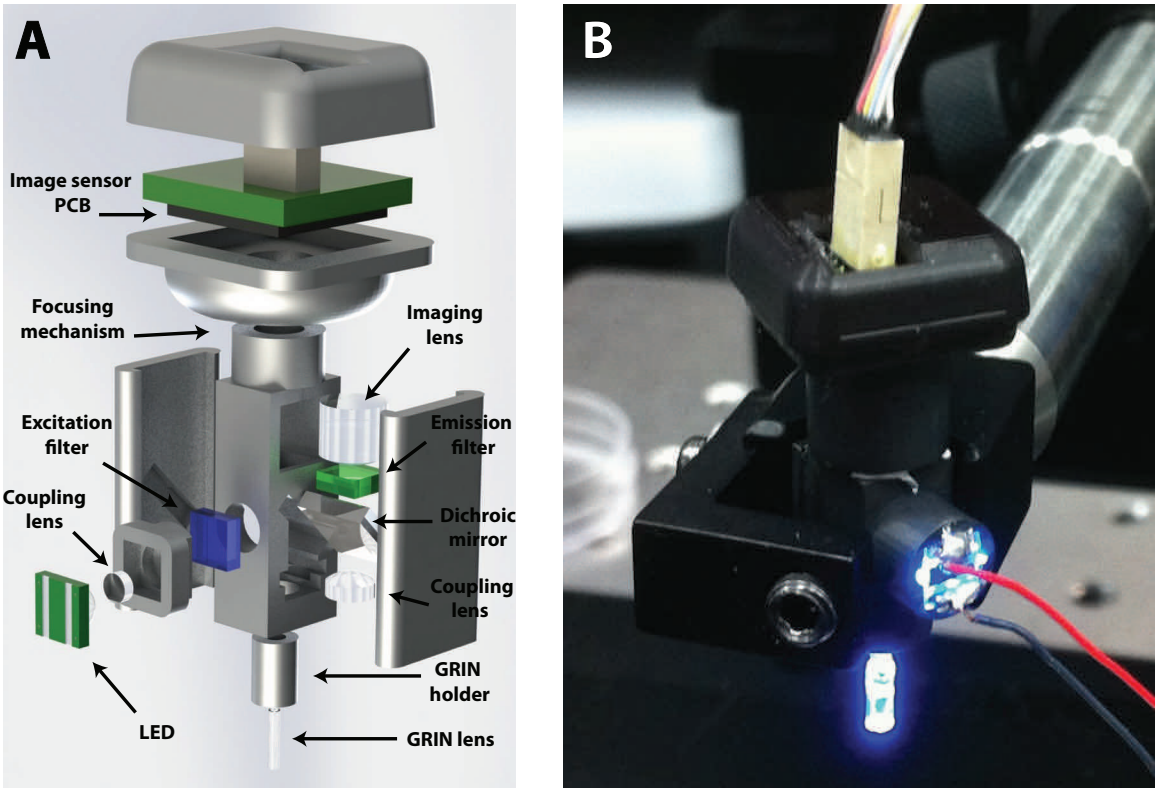

Figure 2.1. Third prototype of the microscope. (A) Exploded view showing optics, light source and imaging sensor. (B) Aluminum version of the assembled microscope.

2.1.2 Light Source

Light emitting diodes (LEDs) are becoming increasingly popular as light source for both fluorescence imaging and optogenetic control [34], due to their small size (scalable down to 5μm), wide range of wavelength, reduced price and ease of integration in the system. However thermal management is a key parameter that need to be controlled both for a stable intensity of light delivered to the target and for heating of the tissue under study (although this is a more serious limitation for injectable optogenetic probes [35–37]).

Stable light delivery can be obtained trough active cooling of the light source [38], however this approach introduces additional weight and impediment for the animal, and it is not viable in a wireless implementation of the imaging system.

2.1.3 Image Sensor

The system presented is intended to be used for two different fluorescence imaging techniques: voltage sensitive dye imaging (VSDI) and calcium imaging. The former has the most stringent requirements for the image sensor in terms of speed, SNR and dynamic range: single action potential resolution is attainable by recording the fluorescence response of the dye molecules injected in the brain area under study to a change in transmembrane voltage [39–41]. Action potentials reflect in typical change in fluorescence $\Delta F/F$ between .1% and 1%, although recent dyes show an improvement in performance [42]. Calcium imaging captures a slower dynamics and is typically used in longer term experiments (minutes to days or weeks of recording), but it provides larger swings in the fluorescence signal to be measured.

Aptina MT9V022 [43] was chosen for the sufficiently high frame rate (240fps) and SNR (up to 48dB with 4x raw and column binning), and the flexibility to choose between a higher resolution (up to 752x480) and a low resolution/high SNR through on-chip row bin − and off-chip column bin. Additionally, it offers a one lane LVDS

serial communication to stream the 10bit data, and this reduces the total number of connections to the control board to 10.

A custom made PCB (11mmx11mm, Fig. 2.2a) was designed to host the image sensor, with a minimum number of discrete components for proper functioning of the sensor. The performance of the system is evaluated in the final setup that will be used in the experiments, with the image sensor PCB mounted in the microscope and connected to a custom made data acquisition system based on the OpalKelly XEM3010 FPGA board.

The dark current was measured for different integration times (Fig. 2.2c) both with and without on-chip 4x row binning (column bin calculated off chip by the programmable logic), after 90 minute of sensor operation inside the microscope to stabilize the temperature. Temporal noise and dark signal non uniformity are filtered by averaging 40 consecutive frames at full resolution and 500 with row and column bin.

To test the detectability of changes in fluorescence for VSDI recordings, the sensor was uniformly exposed to a green LED light modulated with a precisely controlled current source. The minimum detectable light change was 5.5LSB, corresponding to a ΔF/F of 0.65%; by averaging patches of pixels this value can be further decreased, and, with a 4x4 pixel average, changes in intensity of 0.23% could be detected (Fig. 2.2b).

Comparison with state-of-the art miniature fluorescence microscopes is reported in Table 2.1.

Table 2.1. Comparison of the proposed system with current state of the art miniature fluorescence imaging systems.

	Resolution	Pixel size	SNR	Power	Fps	Weight	Interface
[27]	132x124	-	-	2.4 mW	70	11.5 g	Wireless
[26]	640x480	5.6μmx5.6μm	47 dB	-	36	1.9 g	Tethered
[38]	32x32	34μmx74μm	61 dB	12 mW	900	10 g	Tethered
This work	752x480	6μmx6μm	48 dB	320 mW	240	2.4 g	Wireless

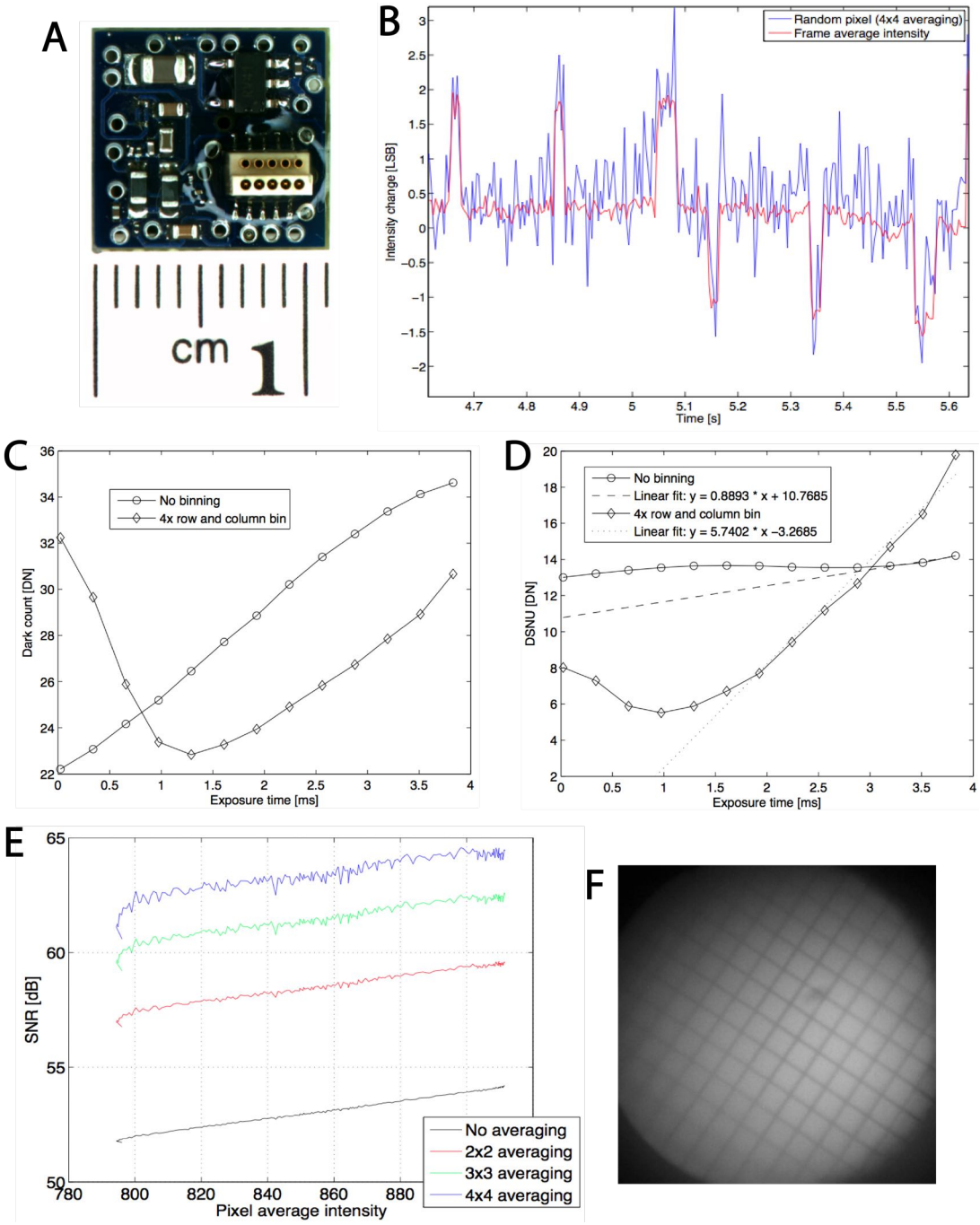

Figure 2.2. The image sensor. (a) The custom PCB hosting the CMOS sensor. (b) Detection of 3 positive and 3 negative spikes in light intensity using 4x4 pixel average, mean value (near saturation) removed. (c) Dark current measured at different exposure times. (d) Dark signal non uniformity for different exposure times. (e) SNR measured for different pixel averaging. (f) Sample image taken with the microscope on a target with 10μm spaced grid.

2.2 Data Acquisition System

A tethered image acquisition system, shown in its final version in Fig. 2.3a was designed to test the performance of the microscope with both in vitro and in vivo calcium imaging experiments. The design and testing of an untethered, standalone imaging platform is currently under development, and presented in the section below. Both systems can be controlled through a graphical user interface which allows to stream video in real time and change experimental settings such as sensor parameters, LED intensity or data acquisition mode, as explained below.

The tethered system consists of a custom PCB which hosts the LED driver, voltage regulators and image sensor interface, and it interfaces with an OpalKelly XEM3010 FPGA board. A USB connection allows real time data acquisition, video streaming and adjustment of experimental parameters from a host computer through a custom C++ graphical user interface called NeuView (Fig. 2.3b).

(a) *Microscope and data acquisition board* (b) *The software user interface NeuView.*

Figure 2.3. Tethered data acquisition system.

2.2.1 System Architecture and Hardware Modules

All the signals required to run and configure the image sensor and to coordinate the video stream transfer to the host computer are generated by the Spartan-3 XC3S-1500 FPGA mounted on the XEM3010 board. All the hardware modules are implemented

in Verilog, compiled under Xilinx ISE and programmed to the FPGA through a USB 2.0 interface. An overview of the system architecture is shown in Fig. 2.4: a 32MB SDRAM is used as storage for the incoming data from the image sensor, and a custom PCB is connected to the two 80-pin GPIO headers. The daughter board hosts the deserializer for the incoming serial data from the sensor, the A/D and D/A converters, the LED driver, the voltage regulators and a 30-pin connector to communicate with the external devices. The onboard PLL is used to generate the three main clocks used by the FPGA to synthesize all the clock frequencies required in the design. Specifically, the three clock domains used in the FPGA are 100Mhz for the SDRAM controller, streaming state machine and to synthesize the clocks for I^2C, DAC and ADC, 80Mhz for the data transfer with the host computer and 26.6Mhz for the image sensor.

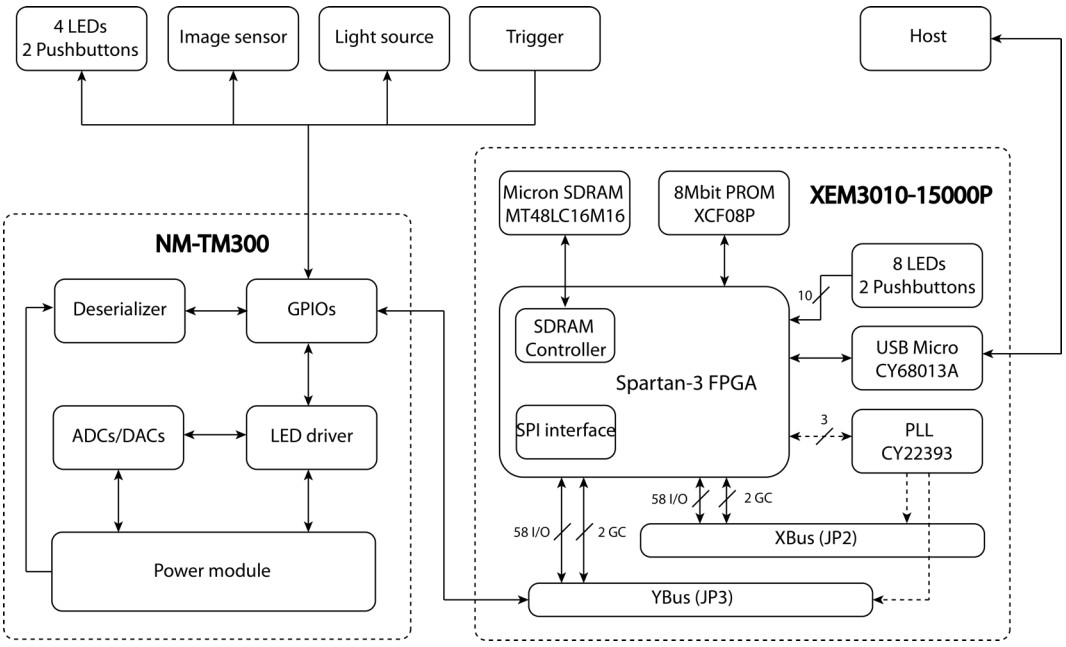

Figure 2.4. Architecture of the tethered system NM-T300.

Streaming live images from the image sensor in real time is a requirement for the system, since before each experiment it is necessary to finely adjust the focusing of the microscope and check the image quality. To this end a frame transfer control module

was designed to regulate the image streaming between the FPGA board and the host computer through the USB 2.0 interface. The steady throughput of this interface is not sufficient to stream continuously high speed images, thus for the experiments the data is saved to the onboard SDRAM first and transferred to the host computer upon conclusion of the experiment.

2.3 Wireless System

The wireless data acquisition system is designed to provide a standalone recording unit capable of streaming data to the remote host. This would allow to perform novel studies on freely behaving animals, but it also introduces important constraints in terms of maximum size and power consumption. One key parameter in coping with these limitations is the choice of the programmable logic used to control the image sensor, light source and wireless communication with the host. Implementing the hardware on FPGA offers several advantages, including low cost, versatility, modularity and not least the possibility of implementing efficient onboard image processing algorithms.

Although Xilinx and Altera remain the two main players in the FPGA market, Microsemi is expanding and after acquiring Actel can now count on their series of low power FPGAs IGLOO, IGLOO2, IGLOO nano and SmartFusion, which are competing for the lowest power and smallest footprint FPGA on the market. In this particular design the IGLOO series was chosen as it supports up to 4 LVDS serial lanes, up to 4 PLL modules for frequency synthesis, Flash*Freeze technology and reduced size with a 4mmx4mm footprint in its smallest package.

Specifically, the AGL400V5-CSG196 was chosen as it meets the requirements in terms of minimum number of IOs, serial lane support and PLL module for clock synthesis. The AGL400 offers several advantages which are particularly desirable in the design of a miniature, low power device for biomedical applications. The flash technology allows for non-volatile memory writing, resulting in less components

required to power up and initialize a standalone system, which is instantly ready at boot. Flash*Freeze technology offers an ultra low power mode (32μW) which can be quickly ($< 1\mu$ s) entered/exited while still retaining all registers and non-volatile memory information. The higher density devices (including the CSG196 package) have 6 usable Clock Conditioning Circuitry (CCC) blocks one of which features a PLL logic block, and they offer good support for multiple clock domains up to 250Mhz. In the CS196 package there are 143 single ended I/Os and up to 35 differential pairs (for each differential pair the number of available I/Os decreases by 2). In the current configuration a total of 94 single ended I/Os and 1 differential pair are used. As for the memory, AGL400 features 54 1-Kbit blocks of dual port SRAM for a total of 6912 bytes of embedded memory which will be used to implement the FIFOs for saving the image data to external SDRAM and for wireless data streaming. It also provides 1Kbit of flash non-volatile memory.

2.3.1 System Architecture

Although IGLOO FPGAs offer good debugging capabilities, the need to have easy access to all the relevant signals and to be able to quickly program and communicate with the board requires the the design of a prototyping board for testing and debugging, which will then be miniaturized. The estimated size of the miniature system is 15mmx25mm with the components arranged in two stacked 4 layer PCBs. The system architecture, shown in Fig. 2.5, includes the following elements:

- FPGA: The AGL400V5-CSG196 is the only control logic and regulates the data transfer between the camera, the external SDRAM, SDCard and wireless interface.
- External SDRAM: 16MB external SDRAM to store experimental data.
- SDCard: used to save the external SDRAM content after each experiment, or to save each frame in long capture (low fps) mode.

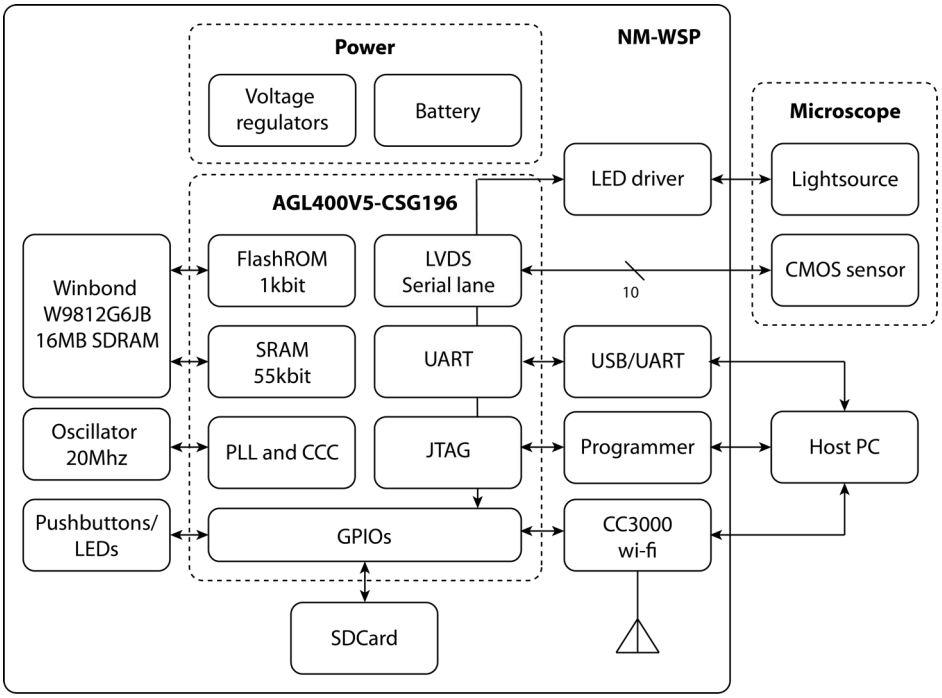

Figure 2.5. Architecture of the prototyping board NM-WSP.

- Programming connector: It interfaces with the FlashPro4 programmer to quickly upload the synthesized program into the FPGA.
- Wireless interface: implemented on the CC3000 module.
- Deserializer: used to convert the 10-bit serial data from the image sensor. In the prototype board both serial and parallel data are available to the FPGA for testing purpose, whereas only the serial interface will be present in the miniature system.
- Image sensor interface: allows to transfer data and power the image sensor module through the 10-pin Omnetics connector.
- GPIO header: a connector to easily access 60 GPIOs from the device (prototype PCB only)

- JTAG header: a 10-pin JTAG header is used to program the device through the FlashPro4 programmer.
- LED/buttons: 8 LEDs and 4 pushbuttons are used for debugging purpose and to reset the device and the wifi interface (prototype PCB only).

2.3.2 Power

Power consumption is one of the key factors in the design of the board, as the resources in the final design will be limited due to restrictions in weight and size of the device. The NM-WSP board can be powered either through an external 5V power source or with a 5V battery. The input can be selected through the jumper JP1 on the board. The 5V power source is regulated with an LTC3533 DC/DC converter, which has better efficiency than linear regulators (above 94% during normal device operation at 200mA). The LTC3533 switching frequency is set to 1Mhz, and it provides regulated 3.3V delivered to the camera module, wi-fi module, AD/DA converters, FPGA banks and deserializer. The schematic for the DC/DC voltage converter is shown in Fig. 2.6.

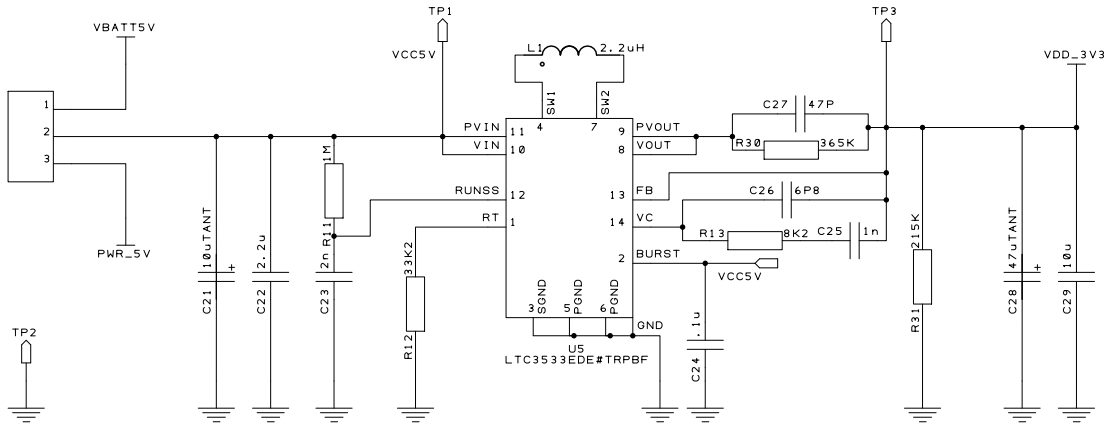

Figure 2.6. Schematic of the DC/DC voltage regulator.

The core voltage for the AGL400 can be either 1.2V (lower power consumption) or 1.5V (better performance). However during the programming of the device the core power needs to be 1.5V. For this reason, in order to avoid the introduction of additional power switching elements, it was chosen the model with 1.5V core voltage, which is delivered to the device through a LT3080 linear regulator. The use of a linear regulator as opposed to a switching regulator is justified by the limited amount of current on the voltage rail (only drawn by the FPGA). The power dissipation is marginal in this case, and the choice of a liner regulator allows a simpler design and less PCB components.

2.3.3 FPGA Routing

IGLOO FPGAs use 4 different routing architectures: ultra-fast local resources, efficient long-line resources, high speed very long line resources and VersaNet global networks. VersaNet should be used to route clocks, resets and any global line which requires low skew or high fan-out.

IGLOO devices provide 54 global pins (3x3 per quadrant/chip location) to access 18 global networks (3x4 regional for each quadrant and 6 global), which are used in the design to drive clocks and reset signals. There are two types of global networks: chip global networks, which can be accessed by VersaTiles anywhere on the device (name starting with GC, GF, respectively, East and West), and quadrant global networks (name starting with GA, GB, GD and GE, respectively, NorthWest, NorthEast, SouthEast, SouthWest), which can only drive the signal inside their own quadrant.

Each global input buffer can be driven either by 3 hardwired connection for the single-ended I/O or by 2 dedicated differential I/O (which need to connect to Gxy0 and Gxy1) and a single-ended connection on Gxy2, or by an internal clock signal. The three global input pins to the northwest quadrant is shown in Fig. 2.7. Any of the three I/Os can be connected to a global network in single-ended configuration (and the remaining two can be regular I/O), but only 0 and 1 can be used for LVDS

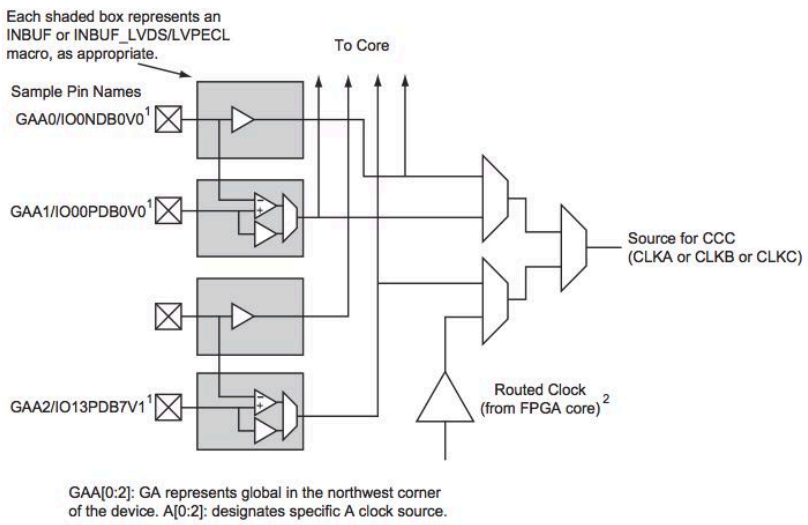

Figure 2.7. Global input pins for the same clock source A in the northwest quadrant.

and LVPECL, and the remaining third can be used as regular I/O. Th unused global pins are automatically configured as inputs with pull-up resistors if they are not used are regular I/Os.

In order to source an external clock the first option is to hardwire the clock to a global input (and the multiplexer tree shown above). If a CLKBUF macro is initiated, the clock input can be placed in any of the dedicated global input pin. However the choice of the pin location will determine whether the clock will use a chip global network (GC, GF locations) or a quadrant global network (GA, GB, GD, GE). Alternatively, also regular I/Os and internal signals are allowed to access global networks through the CLKINT macro or through a promotion of the signal to the global network in the PDC (this however could create layout issues). Similarly, global signal can be demoted to regular nets in PDC.

It is also possible to assign a clock to a spine (also called local network) through PDC or MVN. In this case the clock is automatically demoted to a regular net before being sent to the local network.

When using Synplify in the design synthesis no more than 6 global buffers are inserted in the net list by default, all of them in the chip network. Automatic assignment however can be overwritten using PDC and assigning manually global nets.

When using the PLL (located in the GF global net) only two of the three global resources can be used in that net. It is also possible to restrict a global network to a particular area of the chip, by restricting it from reaching into the scope of a spine.

2.3.4 Clocking Resources

In AGL400 there are 6 Clock Conditioning Circuitries (CCCs) − located at the four chip corners and in the middle of the east and west chip sides − used to implement frequency multiplication/division, phase shift and delay operations. Each CCC can implement up to three independent global buffers, or a PLL function with up to three global outputs. It is possible to configure each CCC either through flash configuration with the programming bitstream or through an asynchronous shift register interface which can be dynamically changed during device operation. The first mode will be used in the current design, as there is no need to dynamically change global clock networks. Each CCC provides three global routing networks (GLA, GLB, GLC), whose location can be chosen between the three I/O in the same CCC location. The CCCs in the 4 quadrant global networks only drive signals in their own quadrant (which spans a quarter of the chip area), whereas the CCCs in the middle west and east sides of the chip can drive the clock anywhere on the chip.

A global buffer can be placed in any of the GLA, GLB or GLC locations. Each global buffer can be driven by:

- 3 single ended I/Os
- 2 differential I/Os
- The FPGA core

If an internal signal needs to drive a global network, the CLKINT macro is used to connect the signal to the routed clock input of the network's MUX tree. It is also possible to connect directly a global I/O or an internal signal to a global quadrant/network through the macros CLKBUF, CLKBUF_LVPEC/LVDS and CLKINT. These macros do not use the PLL and do not provide clock delay functionality. If a programmable delay is required, the clock can be routed to the programmable delay core (3 in each of the CCC blocks) through these CLKDLY macro before connecting to the global/quadrant network. This macro does not use the PLL, but it generates an output clock with a phase shift which depends on the user defined delay value. CLKDLY can be driven by a INBUF macro, directly from the FPGA core, or by an I/O routed through the FPGA regular fabric (this requires the use of the macro PLLINT). It is possible to use up to three CLKDLY macros with independent clock frequency and delay in a CCC where the PLL is absent or not used. In the GF location, when the PLL is used and outputs to a single global network, the two remaining global clock networks can be connected either to two global inputs or to two CLKDLY macros.

In cases where frequency synthesis is required, the PLL (only present in the GF location) can be used to generate up to three global clocks, which can be then connected to global networks. The PLL macro provides 5 derived clocks (three independent global output clocks and two core outputs to local routing networks[1]) form a single reference clock. The clock input can be from a global input pin, from a regular I/O pin or from the FPGA core. In the current design the 20Mhz external oscillator is used as a clock input hardwired to the global input pin GFA0 on pin G2 (acceptable input clock frequencies range from 1.5Mhz to 350Mhz). To prevent toggling of the PLL outputs during power up the POWERDOWN signal of the PLL macro should be held low.

[1]The global output clocks are named GLA, GLB and GLC; the core output YB and YC are identical to GLB and GLC, respectively, except for a higher selectable final delay.

If the external feedback is implemented, the PLL core must receive the EXTFB from an INBUF macro located at the same location of the PLL. All the PLL parameters such as delays and shift values can be set by the user through SmartGen.

The input to any of the CCC blocks or global/quadrant global networks can be chosen to be at any of the three global input pad locations: if the input is single ended, any of the three global input pad (first, second or fourth) can be used, and the other three are assigned to regular I/Os; if differential input is used, it is assigned to the first and second input, and the third is assigned to a regular I/O. However a global I/O pad does not need to feed a global network, it can also be assigned to regular I/O. If the input to a CLKDLY block is hardwired to a global pin, any of the 9 pins for each specific location can be chosen; in the case of PLL input however (only available in location GF), only one of the three global pin locations GFA0, GFA1 or GFA2 can be used. Alternatively, the clock can be sourced from any regular I/O pin on the device (referred to as external I/O clock sourcing), providing great flexibility in selecting the clock location, but at the cost of introducing additional delay, as the signal does not connect directly to the CCC reference clock input. Finally, the clock can be sourced internally from the FPGA core, by instantiating the routed signal with a PLLINT macro before connecting to the CCC clock input.

2.3.5 PCB Layout

For debugging purpose, power measurement and initial testing, a 110mmx80mm 4 layer PCB was designed around the IGLOO AGL400 FPGA (Fig. 2.8). The main connections for interfacing with the prototype board are shown in Fig. 2.9: the system can be powered either through a 5V adapter or from a battery, and the data from the camera can be routed either through the onboard 10-bit deserializer or directly to the FPGA through the LVDS serial lane. Two 40-pin connectors provide access to most of the internal signals for debugging and testing, and a USB/UART module is available for communicating with the FPGA from a host computer. A JTAG connector is used

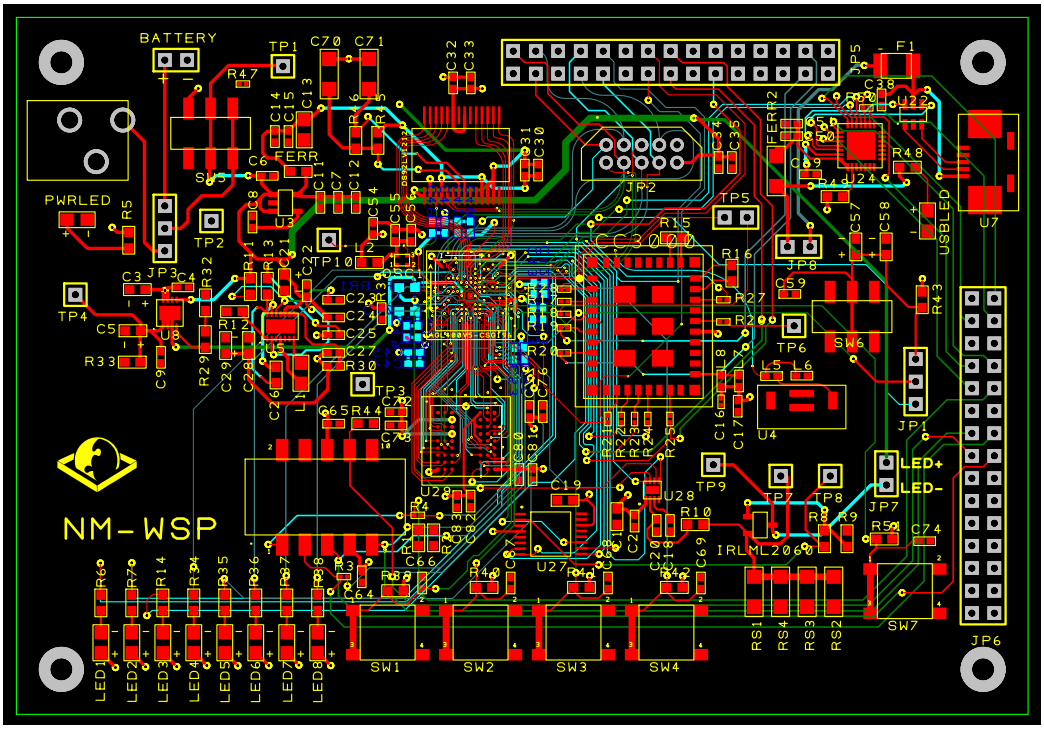

Figure 2.8. Outline of the 4 layer PCB used as testing and debugging platform for the IGLOO AGL400.

either for regular debugging or to program the FPGA through the Actel FlashPro4 Programmer. Additionally, the board hosts the SDRAM module, wifi interface (TI CC3000), LED driver and control circuit, 4 pushbuttons and 8 LEDs for debugging purpose as well as several test points for probing power rails and signals of interest.

The PCB prototype is shown in Fig. 2.10.

The .5mm pitch of the BGA grid used in the FPGA CSG196 package requires some stringent tolerances for the PCB printing, reported in Table 2.2.

2.4 Software Interface

A C++ graphical user interface, called NeuView, was written to provide the user access to the image sensor control parameters. A screenshot of the streaming view is shown in Fig. 2.3b. The software is designed to provide a common framework for

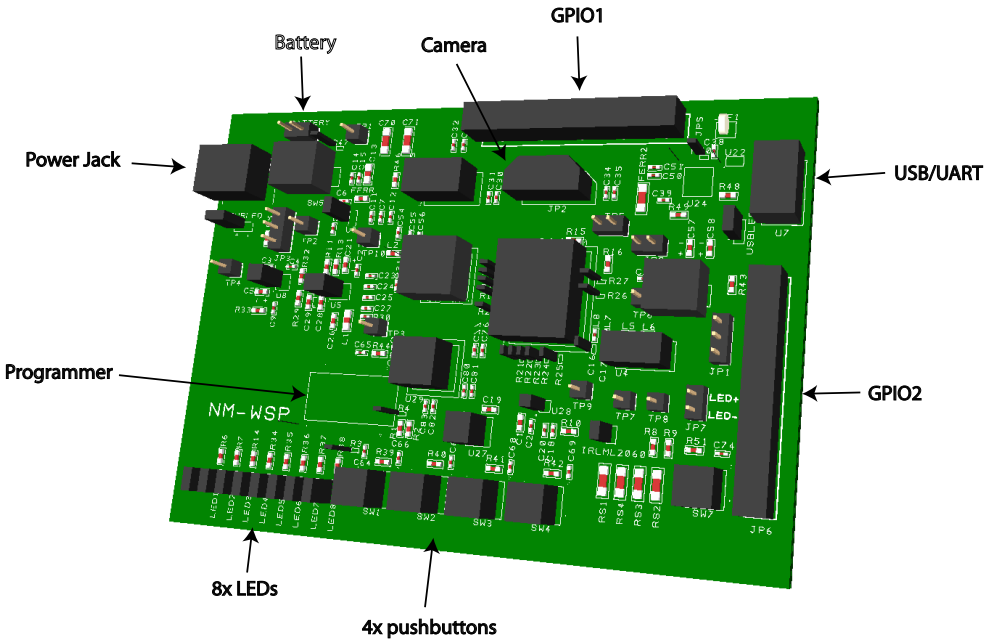

Figure 2.9. 3D render showing the component side of the IGLOO AGL400 PCB and its main connections.

Table 2.2. Minimum specification required for PCB fabrication.

Number of layers	4
Panel size	5”x3.1”
Minimum plated hole drill size	0.006”
Minimum pad diameter to hole size	0.004”
Minimum track size inner layers	0.00275”
Minimum track size outer layers	0.00275
Minimum pads/tracks spacings	0.004
Number of vias	350
Number of drilled holes	450

different experimental setups, and it can be used both for the tethered and for the wireless system.

In the tethered setup the data is streamed from the OpalKelly board through the USB port in two different modes:

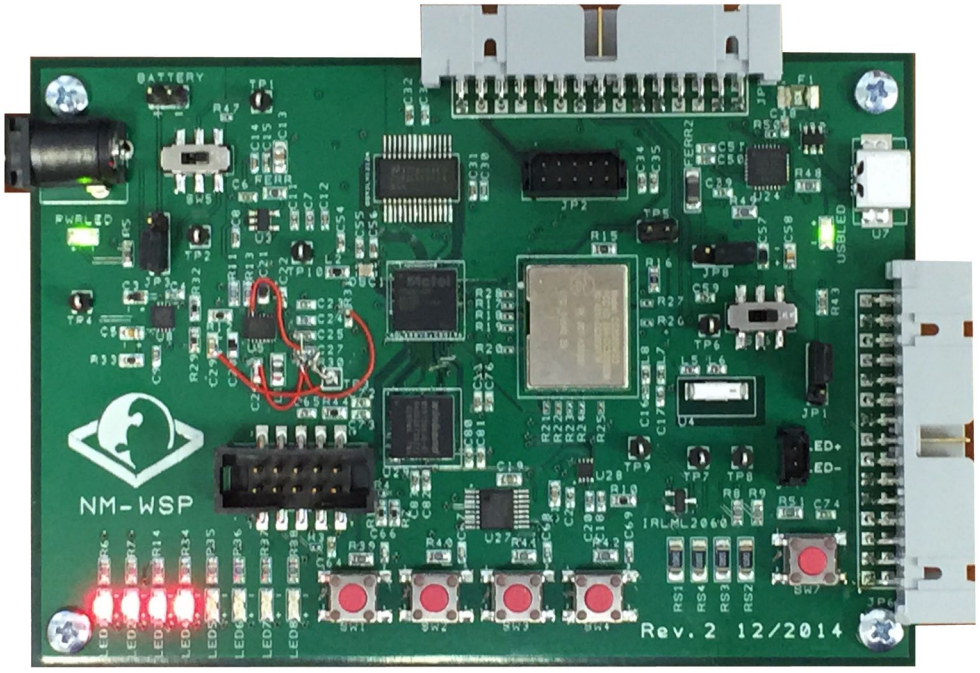

Figure 2.10. The prototype NM-WSP board.

- Continuous streaming. Each frame is continuously saved by the programmable logic which uses the onboard SDRAM as a circular buffer. The address of the beginning of the last full frame is constantly refreshed, and and when the host is ready for receiving a frame it initiates the transfer; once the full frame is transferred to the host it is sent to the unpacker which interprets the data and displays it on screen, and another transaction can be initiated. The achievable throughput is 1MB/s, and this data transfer method can be used either for streaming only (in which case the frame on the host SDRAM is constantly overwritten), or for recording: in this case every frame received is saved to the host ram or alternatively, for long experiments which require more than 2GB of data, directly to disk.

- Consecutive frames. When higher throughput is required for the experiment (in the case of VSDI for example), it is possible to fill the onboard SDRAM with

consecutive frames and subsequently transfer the entire SDRAM content to the host. This guarantees that no frame is dropped even at hight frame rates.

In the wireless implementation the frames can be routed by the slave (device side) to the onboard SDRAM, to the onboard SDCard or directly to the master (host side) through the CC3000 wifi interface, for which a common hardware module was written both for the master and the slave (Fig. 2.11). After device initialization a mask command is sent to the device in order to mask unsolicited events such as ping or keep alive, which would send the module into an error state. Then if the smart_config button is held down the system enters in a configuration mode to set the connection parameters such as Access Point (AP) and IP address (this is a one time only configuration process). After reboot the device will try to automatically connect to the AP.

The wireless communication is implemented with the UDP protocol, as it introduces the least amount of overhead to each packet transmission, thus optimizing the transfer speed. However the absence of handshaking between transmitter and receiver requires the implementation of a protocol to regulate the data transfer and packet loss. This is done on the receiver (master) side by monitoring the control bits of the data packet. Each packet is 1463 bits wide, including a header which includes frame number and packet number inside the same frame, 1450 bytes of pixel data (725 16-bit consecutive raw pixel values) and a 3 byte end of data code.

The wifi system has been initially tested on a Spartan6 based Xula2 FPGA board (Xess Corp.) for continuos streaming and it was possible to reach a steady transfer speed of 220kB/s.

2.5 System Performance

The full system has been tested and validated both in vitro and in vivo, demonstrating the concrete benefits of its application to the study of neuronal circuits.

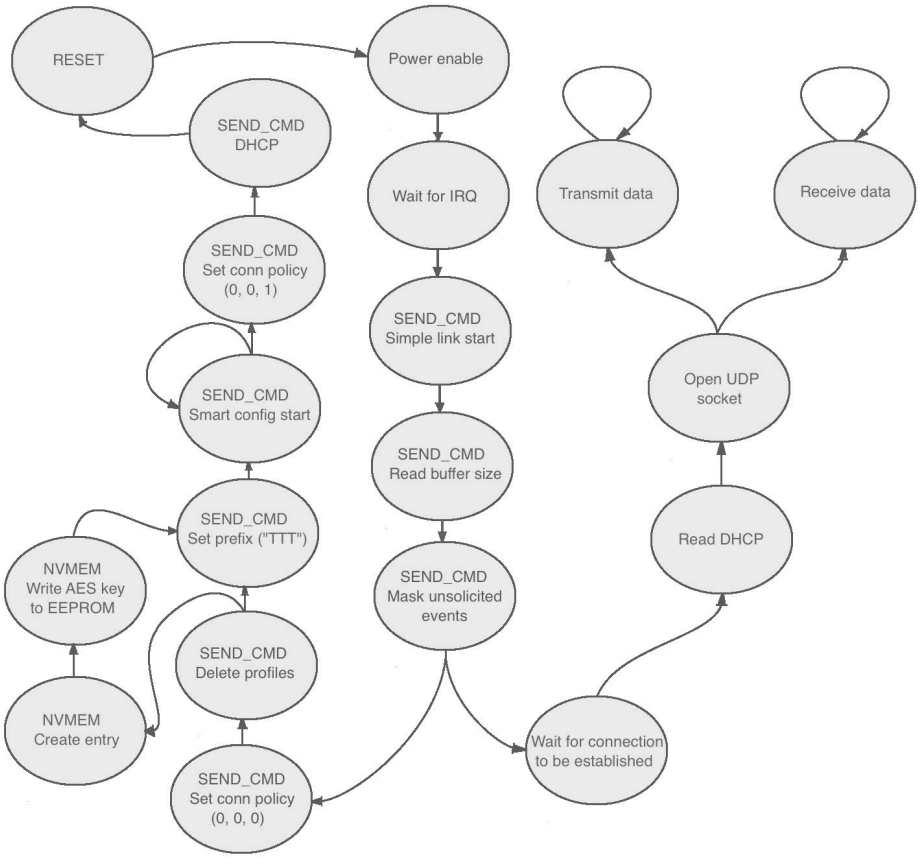

Figure 2.11. State machine for the wifi communication: the slave (device side) streams the data to the master (host side).

The results are expected to be qualitatively identical for the wireless system, as the imaging interface will be the same.

2.5.1 In Vitro Testing

The optimization process for the microscope led to the design of three different generations, each one addressing specific issues: in the first generation the material chosen could not guarantee an acceptable precision and was not suitable for the accurate alignment of the optics. Furthermore, a better focusing mechanism for the gradient index (GRIN) lens was needed.

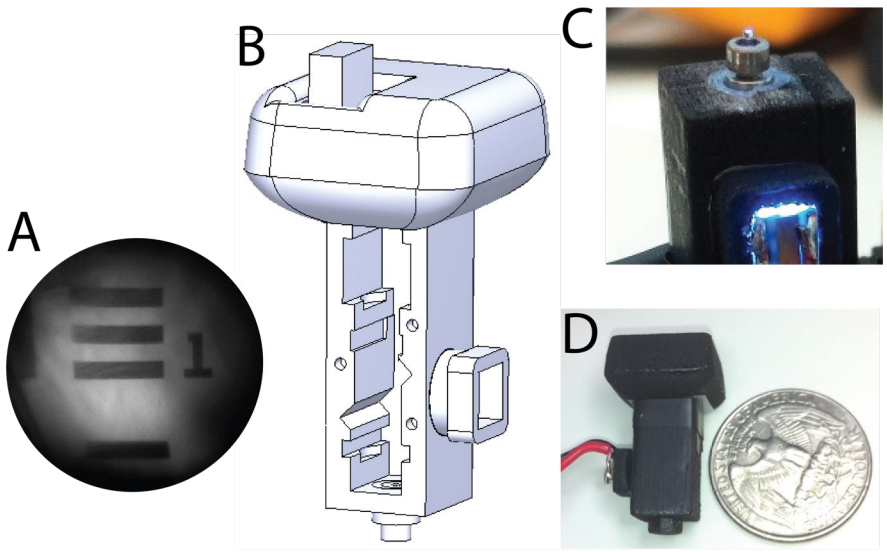

Figure 2.12. Microscope prototypes. (a) Image of a 1951 USAF target taken with the second generation microscope. (b) CAD model of the first prototype. (c) Aluminum focusing mechanism for the GRIN lens installed in the second generation microscope. (d) Fully assembled first generation microscope.

With the second generation an aluminum focusing mechanism was introduced on the objective side of the microscope (shown in Fig. 2.12c), and better alignment of the optics enabled to focus and capture images of a target (Fig. 2.12a). However the correct lens placement was challenged by the shape of the body, which did not allow easy access to certain areas inside the body. Another major concern was the autofluorescence of the black resin, which produced a high background fluorescence, as can be seen from the images of a Thy-1 YFPH mouse brain slice (Fig. 2.13).

Additionally, at high intensities, light leakages were recorded through the microscope body, and the introduction of an excitation filter became necessary due to the wavelength shift in the high power LED.

The third prototype solved all these issue, and with calcium indicators it was able to produce in vitro results whose quality is approaching the one of benchtop imaging systems.

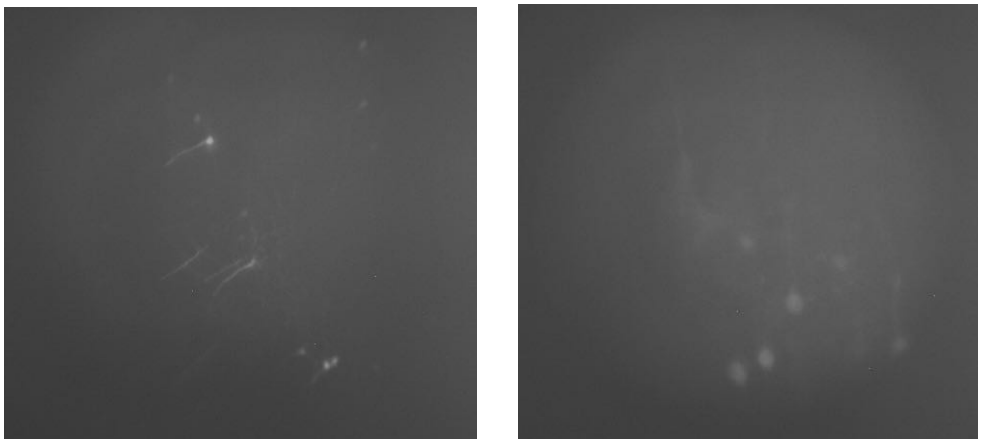

(a) *Witout GRIN objective lens.* (b) *With GRIN objective lens.*

Figure 2.13. Two images of a Thy-1 YFPH mouse brain slice, taken with the second generation microscope. Background fluorescence and light leakages from the body were issues to be solved.

Fig. 2.14 shows two images acquired from a brain slice of a Thy-1 YFPH mouse with third generation microscope.

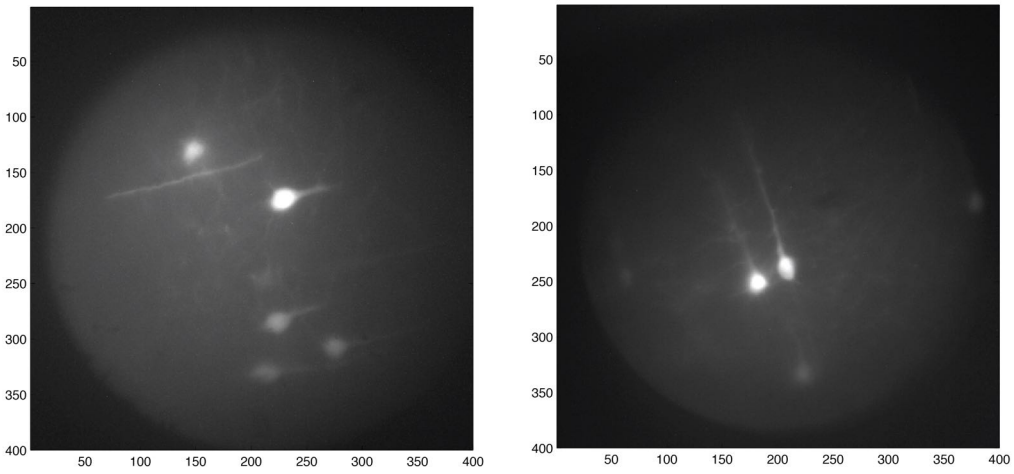

Figure 2.14. Two images of Thy-1 YFPH mouse brain slice taken with the third generation microscope. Both the cell body and proximal dendrites could be easily visualized using the miniature microscope, demonstrating that the miniature microscope allows acquisition of biological relevant fluorescent signals from brain tissues.

2.5.2 In Vivo Testing

After obtaining satisfactory results from testing the microscope in vitro, the tethered system was tested on freely moving transgenic mice expressing the calcium indicator GCaMP6. Three weeks after the GRIN lens implant it was possible to record and clearly identify neuronal action potentials as reported by the genetic calcium indicator. A time sequence of the experiment is reported in Fig. 2.15. Single cells can be identified and the local fluoresce quantified according to the labeling of Fig. 2.16. The time series of the recorded signal for each cell location are shown in Fig. 2.17.

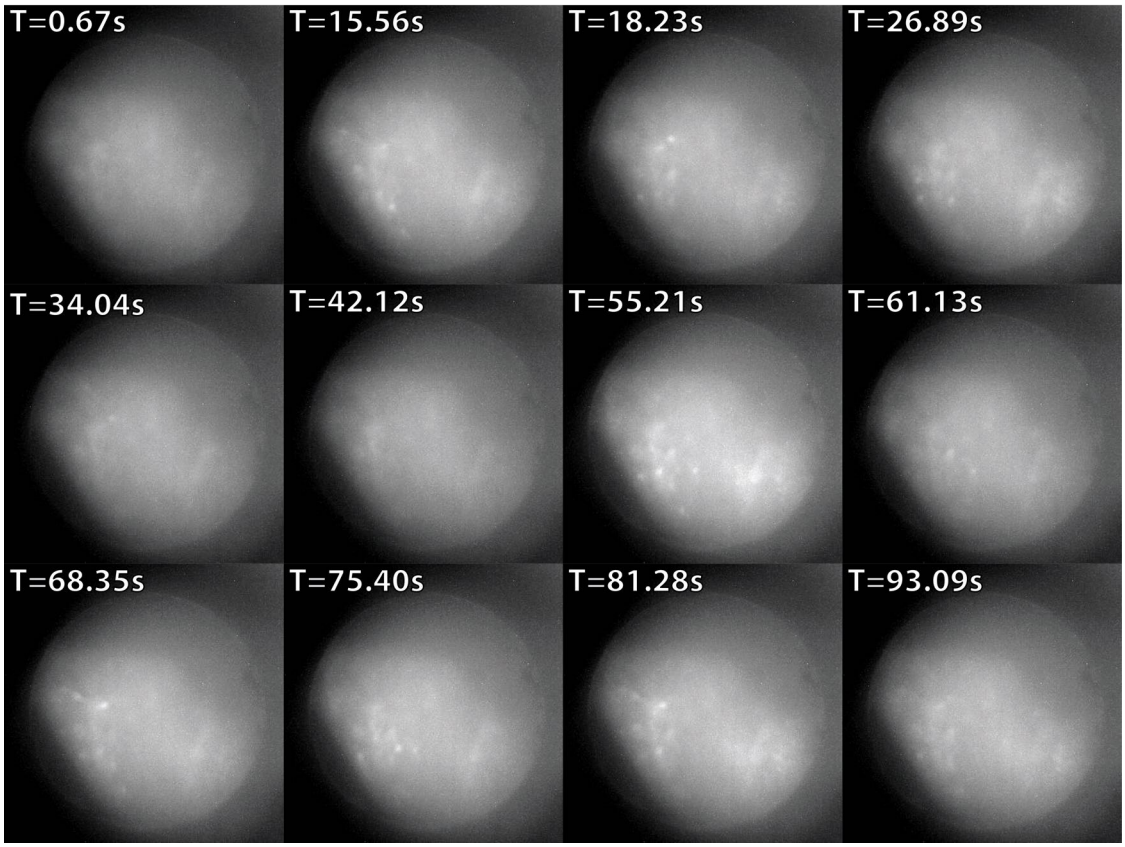

Figure 2.15. Time sequence of a 100s in vivo recording of a GCaMP6 stained neurons in the dorsal striatum of a freely moving mouse, 3 weeks after GRIN lens implant. Single action potentials with different temporal patterns can be clearly identified across the frames.

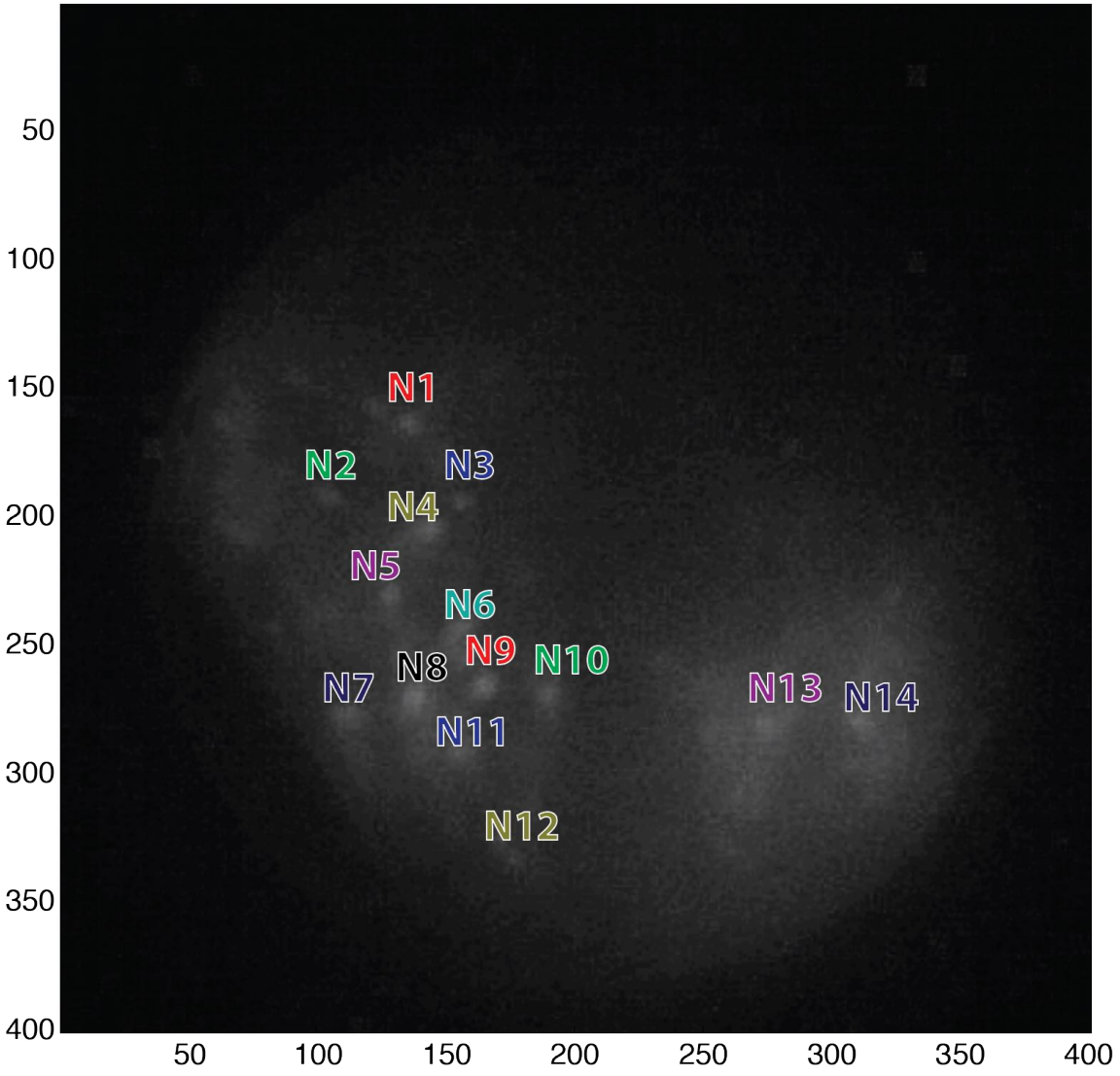

Figure 2.16. Neuron labeling for the in vivo experiment. Cell locations are identified in the image by taking the difference between the maximum and average pixel intensity across the frames, at a single pixel level.

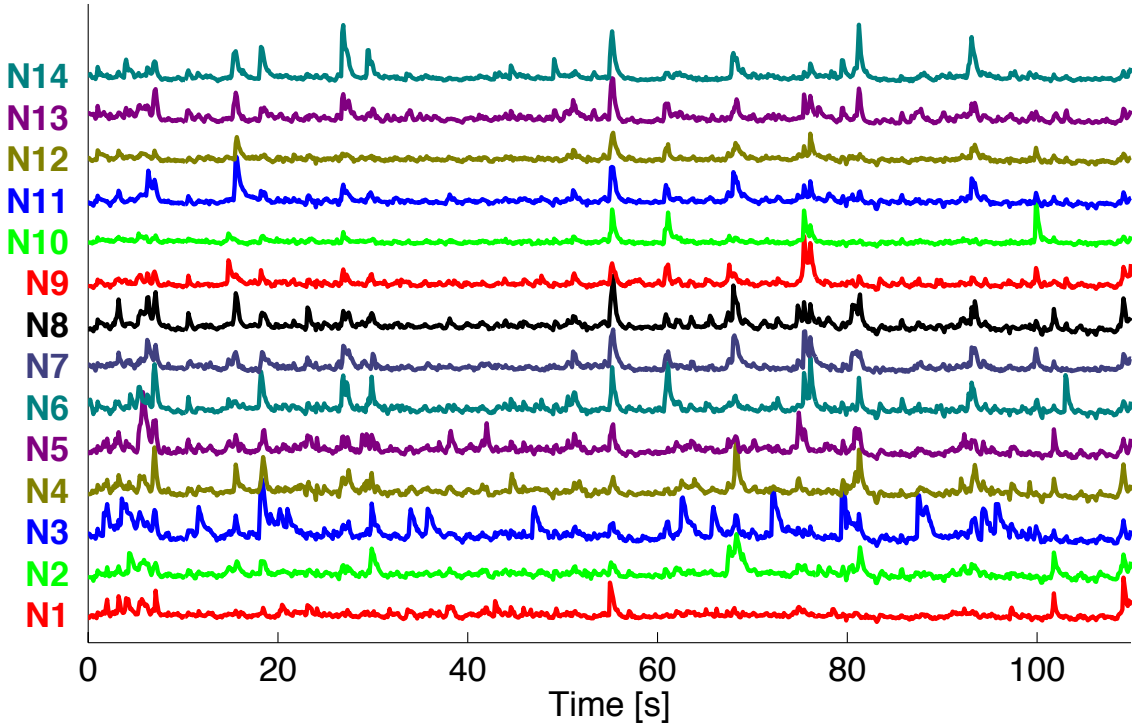

Figure 2.17. Time series of the fluorescent signal recorded for the different cell locations as labeled in Fig. 2.16. From each signal is removed the average background value of a 100x100 square pixel region centered at the centroid of the cell.

3. METHODS FOR CALCIUM IMAGING DATA ANALYSIS

In vivo wide field calcium imaging offers an unprecedented insight into the functioning of intact neuronal circuits, however it also poses several challenges which need to be addressed for a correct interpretation of the neural activity information and the understanding of its underlying biological principles and implications.

A crucial step in the interpretation of a neuronal population's activity is the preprocessing of the raw data and the extraction of individual cells' calcium traces, that is all the calculation involved in the extraction of the individual calcium traces from the raw image sequence.

In this section we present the state of the art of the data processing techniques in calcium imaging and propose new tools for the analysis and interpretation of neuronal activity at a population and single cell level. This chapter is structured as follows: the first section introduces the techniques commonly used for preprocessing the raw images, including image registration, cell detection and calcium trace extraction. Then an optimized algorithm for real time implementation is presented along with experimental data.

In the second part of this chapter the most common clustering methods are discussed, with particular focus on k-means algorithm, experimental clustering validation procedures and their application to calcium traces analysis.

Next, the relation between neural activity and behavior is explored, through the adaptation of machine learning algorithms and statistical methods to neural activity data analysis to decode behavioral states and variables and examine their relation with neuronal activity events and patterns.

Finally, we consider the study of neural synchronization as a tool for assessing network properties and connectivity.

3.1 Preprocessing

Preprocessing of the raw image sequences includes all the steps necessary to convert the raw data recorded from the microscope into a set of time sequences associated with single cell calcium transients. Three main steps are involved: image registration, automatic cell detection and calcium trace extraction.

3.1.1 Image Registration

Recording of neural activity with calcium imaging and voltage sensitive dyes often suffer from linear transformations of the images within the same set of data or across different experiments, mainly due to motion artifacts and variations in the imaging system position. Since in most imaging systems the microscope can be mounted with high angular precision, we will focus on lateral displacements only. Due to the large amount of data collected in optical neural recordings, it is necessary to use an automated algorithm which can provide a common spatial frame of reference for analyzing and correlating neural activity.

A comprehensive list of the main criteria for the classification of medical image registration algorithms are well discussed in [44]. The most important parameter to consider for choosing the proper image registration algorithm is the type of transformations which the images undergo. Due to the nature of the images produced with the system under study, in the present work we focus on the correction small rigid transformation, specifically small lateral displacements.

The primary statistical tool used as a metric of comparison between images or between similar features within images is cross-correlation [45]. Given a pair of images

T and I (where T could be a sub-portion of the image), their normalized cross-correlation can be written as:

$$C(u,v) = \frac{\sum_x \sum_y (T(x,y) - \mu_T)(I(x-u, y-v) - \mu_I)}{\sqrt{\sum_x \sum_y (I(x-u, y-v) - \mu_I)^2 \sum_x \sum_y (T(x,y) - \mu_T)^2}} = \frac{Cov(I,T)}{\sigma + I\sigma_T} \tag{3.1}$$

It is important to notice that due to the sensitivity of cross correlation to changes in light intensity and exposure conditions, a normalization is required, and this often accomplished by subtracting the mean from both images and dividing by their standard deviation. The cross-correlation function $C(u,v)$ will have a peak in the (u,v) location corresponding to the spatial translation between the two images I and T.

One of the main drawbacks of this approach is the number of computations required, since all possible combinations of x and y translations for the given domain need to be computed. This makes cross-correlation based algorithms suitable for small rigid or affine transformations only, and in general not convenient for being implemented in hardware for real time applications. Furthermore, the dependency on local lighting conditions (such as the simultaneous activation of a cell population, or the contribution of background activity from out of plane neurons), makes this approach not well suited for our purpose.

Frequency based image registration techniques [44, 46–48], on the other hand, offer excellent rejection of frequency-dependent and correlated noise, and they can be efficiently implemented in hardware through FFT. The main link between space and frequency domain transformation analysis is the Correlation Theorem, according to which the Fourier Transform of the correlation of two images is the product of the Fourier Transform of the first image and the complex conjugate of the Fourier Transform of the second.

Fourier methods can be divided into three categories: phase correlation, cross power spectrum and power cepstrum methods.

The phase correlation method [49] is based on the Fourier Shift Theorem: consider two images f_1 and f_2, and let f_2 be a translation of f_1 by (x_0, y_0), that is:

$$f_2(x, y) = f_1(x - x_0, y - y_0), \tag{3.2}$$

and let $F_1(\omega_x, \omega_y) = \mathfrak{F}(f_1(x, y))$ and $F_2(\omega_x, \omega_y) = \mathfrak{F}(f_2(x, y))$ be their Fourier transforms. Then, for the Shift Theorem:

$$F_2(\omega_x, \omega_y) = F_1(\omega_x, \omega_y) e^{-j(\omega_x x_0 x + \omega_y y_0)}, \tag{3.3}$$

or, in terms of their normalized cross power spectrum:

$$\frac{F_2(\omega_x, \omega_y) F_1^*(\omega_x, \omega_y)}{|F_2(\omega_x, \omega_y) F_1^*(\omega_x, \omega_y)|} = e^{-j(\omega_x x_0 + \omega_y y_0)}. \tag{3.4}$$

In principle, the inverse Fourier transform of the cross power spectrum is then the Dirac delta centered in (x_0, y_0):

$$\mathfrak{F}^{-1}\left(e^{-j(\omega_x x_0 + \omega_y y_0)}\right) = \delta(x_0, y_0). \tag{3.5}$$

A remarkable property of this method is that the phase of the cross power spectrum is not sensitive to noise associated with a narrow frequency band (such as slow spatial changes in intensity)[1]. Furthermore, it is independent of any type of gain or multiplication factor, including blurring kernels, which are simplified by the normalization term in Equation (3.4).

In reality, the images to be analyzed are discrete downsampled representations of f_1 and f_2, and these results are only valid for integer values of image shifts x_0 and y_0. Although the average cell diameter in the dorsal striatum is 20 μm (which corresponds to a minimum of 8 pixels using a wide field 1mm GRIN lens), image-to-image

[1]White noise on the other hand would introduce inaccuracies in the peak location, as the entire frequency spectrum is affected.

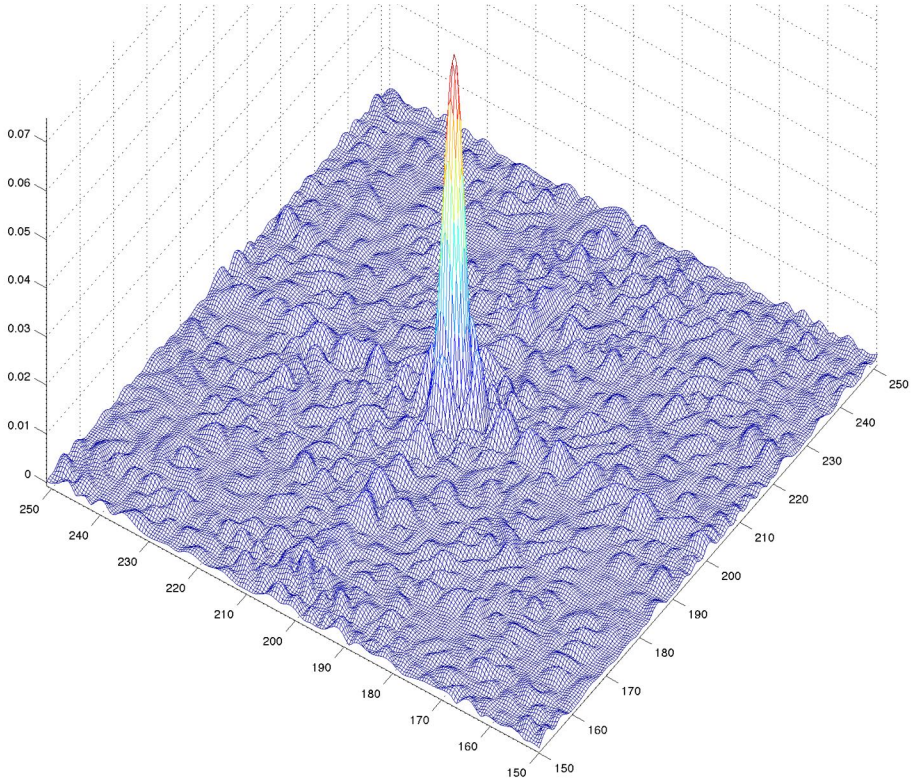

Figure 3.1. The peak of the interpolated inverse Fourier Transform of the cross correlation function between two sequential frames.

registration to the nearest pixel would not allow sufficient precision to accurately identify the neurons over long periods of time.

The raw image data often does not include automatically recognizable features (e.g. blood vessels or labeled cells), and the dominant low frequency components of the image do not contribute to identify small phase differences in the cross-correlation. The most common preprocessing technique used to highlight cell activity is to subtract the background (or the average single pixel value) from each frame. However after such operation two frames taken only few hundreds of milliseconds apart can be too different to provide detectable peaks in their cross-correlation function. For this reason we chose to calculate the relative displacement between sequential images,

which requires robustness and sub-pixel accuracy. The incremental sub-pixel image shift is then integrated across all frames and rounded to the nearest integer.

The most natural and common extension of the phase correlation method to sub-pixel precision image registration is through interpolation of the cross correlation function [50,51]: this is done by interpolating with a cubic spline the inverse transform of the cross correlation function as calculated in Equation (3.4). A typical peak of the interpolated function is shown in Fig. 3.1.

A typical pair of sequential frames before and after preprocessing is shown in Fig. 3.2.

3.1.2 Automatic Cell Detection

In the present work we focus on the study of D1 and D2 neurons in the dorsal striatum. The overall uniformity and consistency in shape of the observed neurons suggests to apply a selective filter matching the average cell size. Current state of the art approaches to identify active regions according to their spatial and temporal correlation use ICA or PCA analysis (or a combination of both). This approach however is computationally expansive and therefore its scope is limited to an off-line data analysis. The proposed method aims at a providing a computationally efficient way of dynamic identification of firing cells with the ultimate goal of real-time hardware implementation on FPGA. The development of such an algorithm would not only reduce the computational time associated with data analysis but most importantly it would enable real-time feedback control for application of optogenetic neural stimulation.

The nature of calcium images makes it difficult to formulate a generic procedure for cell identification robust to changes in cell size, light intensity, background illumination, light scattering in the brain tissue, and other sources of noise. The measured light intensity, even in frames belonging to the same experimental dataset, can be heterogeneous and of difficult interpretation.

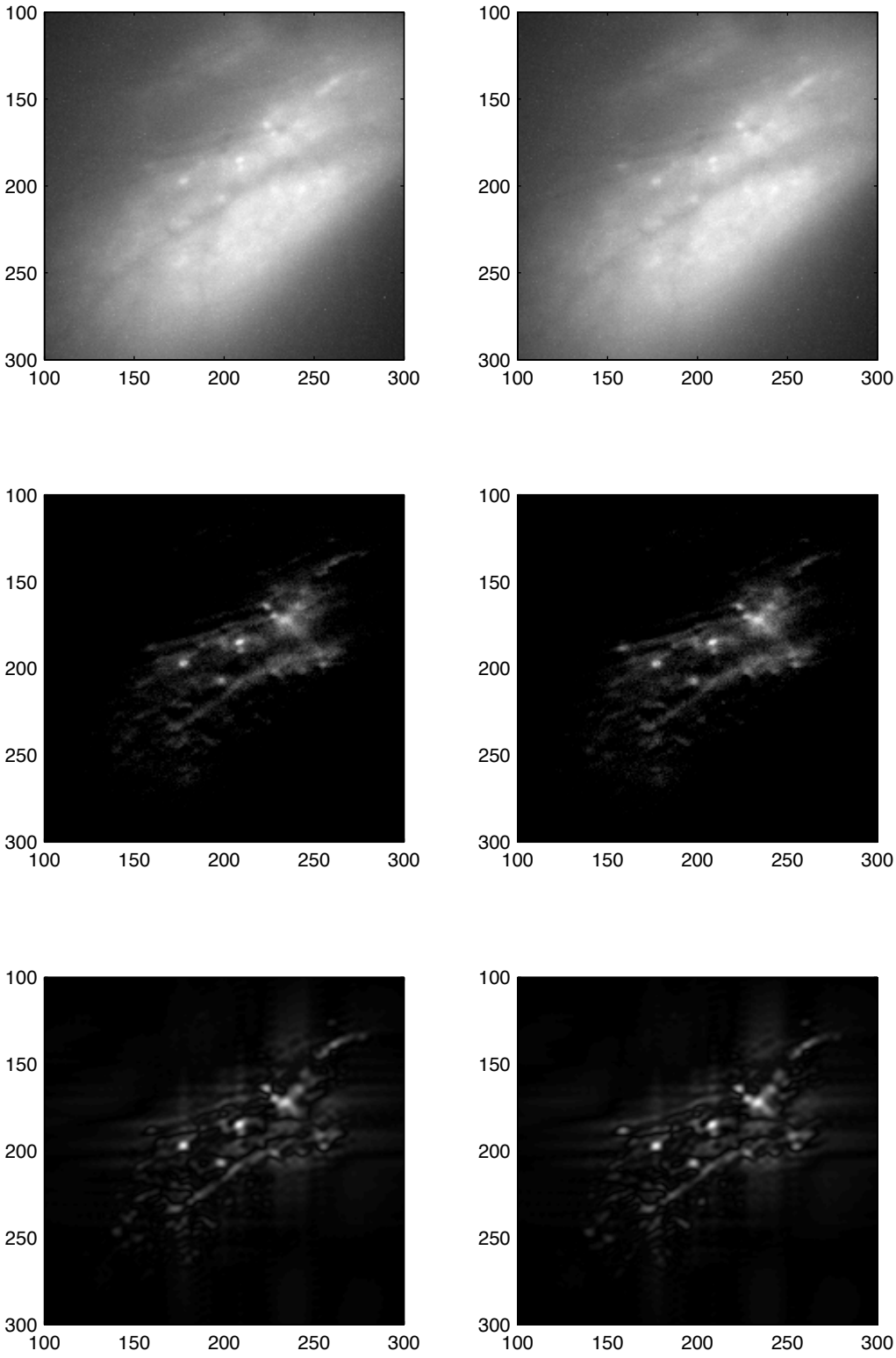

Figure 3.2. Two sequential images as captured by the image sensor (top row), after background subtraction (middle row) and and after bandpass filtering (bottom row).

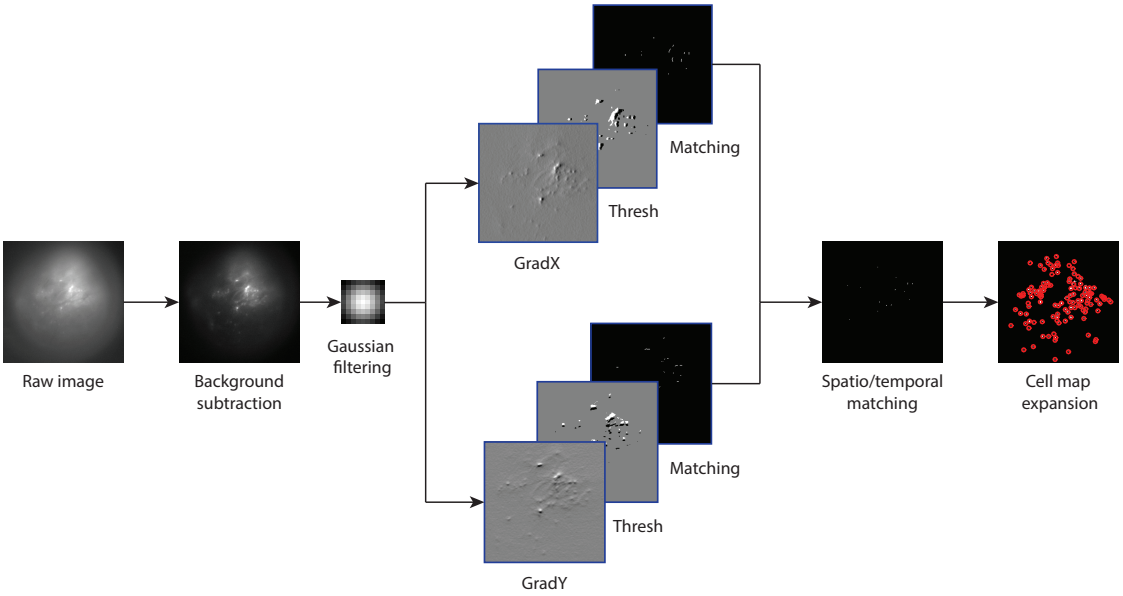

Figure 3.3. Workflow of the cell identification algorithm. After background subtraction and gaussian filtering for high frequency noise removal, the x- and y- gradient components are calculated in parallel; a threshold is then used to detect positive and negative peaks, and a spatial filter is applied to detect specific patterns. The resulting possible cell locations are then spatially (x- y-) and temporally matched to create the instantaneous map of the identified cells, which is finally incorporated into the overall cell map.

The proposed cell identification algorithm is outlined in Fig. 3.3 and applied sequentially to each frame, constructing a dynamic neuronal map as more cells are activated. This approach allows to identify neurons even if they are only activated once during the entire experiment, but the importance of robustness to noise (especially against false positives and stability of the image) is crucial.

First the background is removed from each frame by subtracting the minimum value of each pixel calculated across the first 300 frames. This helps to identify neural activity and reduces fixed pattern noise. The frame is then filtered with 3x3 gaussian filter to reduce high frequency noise before derivation. The gradient components are then calculated separately, by computing the image derivative row-wise and column-wise. A threshold is applied to each component of the gradient to identify positive

and negative changes in light intensity: the edges of a cell are typically characterized by the sequence of a positive and a negative peak in the spatial derivative of the light intensity, as shown in Fig.3.5 below. The proposed cell identification algorithm scans rows and columns for matching such a pattern. The identified cell are then cross-compared between the x-, y- and temporal component for improving the accuracy.

FIg. 3.4 shows typical line and column pixel values observed in the raw data (after background subtraction): using solely the pixel intensity information would not yield reliable information about the cell size and position, mainly due to the issues related with changes in background fluorescence, out of plane cell activity, and simultaneous activation of entire populations of neurons. A more distinct pattern emerges from

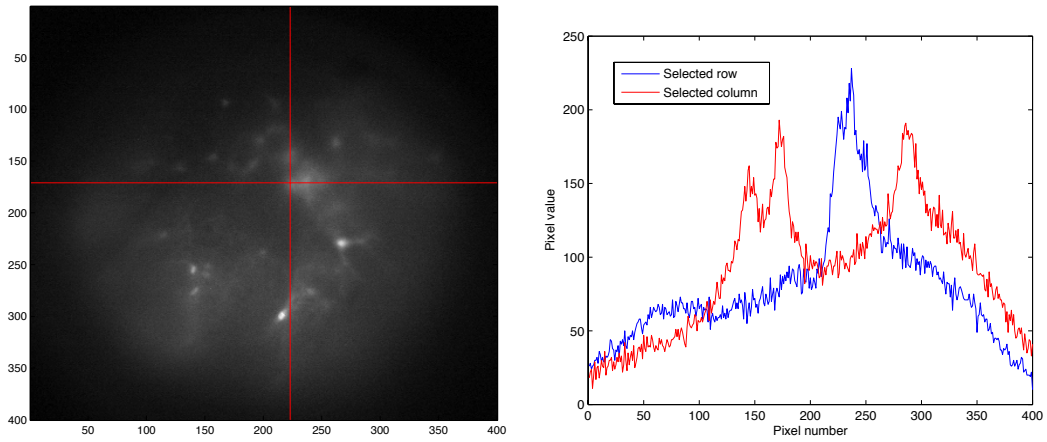

(a) (b)

Figure 3.4. (a) Raw image after background subtraction, highlighting selected row and column in red. (b) Pixel values for selected row (blue) and column (red).

the analysis of the spatial derivative of the pixel intensity (as shown in Fig. 3.5): for each active neuron a clear positive spike followed by a negative spike in both gradient components can be detected. The width of the window used to match the pattern determines the tolerance of the cell size, and should be set according to the expected neuronal density and average size.

The result of this incremental neuronal map is shown in Fig. 3.6 The underlying idea could also be implemented using spatial convolution to match more complex cell

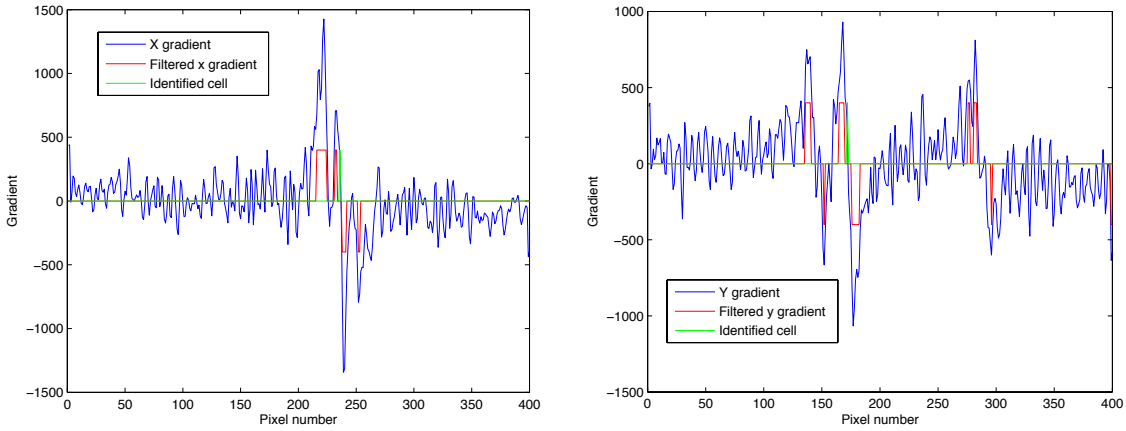

Figure 3.5. X- (left) and Y- (right) components of the gradient of the pixel intensity values for the considered line and column.

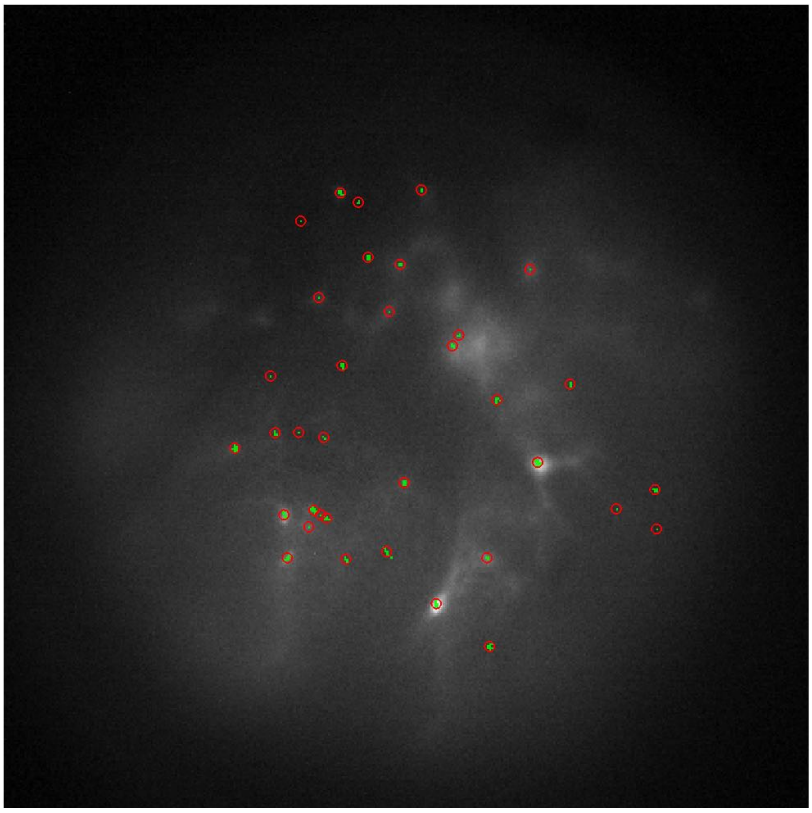

Figure 3.6. Output from the cell identification algorithm: the green mask represents a positive match of the neuronal pattern in the x and y gradient and in the time sequence.

shapes, however this choice would impact the performance in terms of computational cost, and did not show substantial improvement in the accuracy of the algorithm for the dataset under study.

3.1.3 Calcium Traces Calculation

Once the map of all active cells is available, individual calcium traces can be calculated. Due to the nature of epifluorescence imaging, background fluorescence is inevitable and needs to be accounted for when extracting the individual calcium traces.

A commonly adopted method for extracting neural activity information is the one proposed in [52]: after defining a ROI, the neural activity is expressed as the ratio between the average subtracted mean intensity of the ROI ΔF and the local baseline fluorescence baseline F, defined as the temporal average (or minimum value) in the ROI across all frames. Further temporal filtering is typically applied to smooth the fluorescence trace with a cutoff frequency of 5-10Hz.

The subtraction of temporal average, although it can be an effective way to reduce slow drifting of the overall baseline activity, is not effective in eliminating the contribution from the fluorescence signal generated by out of plane neurons, due to their similar temporal dynamics.

Additionally, any kind of temporal filtering will affect the calcium transient shape and rise time, which is particularly undesirable when studying network synchrony and simultaneous neural activations.

To overcome these limitations we propose a new method which simultaneously reduces the contributions from the baseline shifting and out of plane neural activity without applying any temporal filtering.

First, the ROI is chosen as the smallest circular region enclosing the cell body only (this hypothesis only holds in the case where the fluorescence protein is expressed in the soma, and there is no interested in capturing neural activity along the axons).

In the case of medium spiny neurons in the dorsal striatum, the diameter of the ROI was set to 20 μm, which was enough to encircle the somas of all the detected active neurons. The average activity in the soma is then calculated for each time instant as the average pixel value for each pixel in the ROI. Using the maximum value instead of the average pixel value of the ROI could improve the robustness to the precision of the cell localization algorithm, but it also introduces high sensitivity to contamination from neighboring cells, and this should be avoided in the case of densely populated regions. Similarly, the reference fluorescence is calculated as the average of the minimum pixel values for the N pixels in the ROI:

$$F = \frac{1}{N} \sum_{i=1}^{N} \min f_i(t). \tag{3.6}$$

Next, an annular region is defined as the intersection between the ROI and a larger circle of radius R centered on the cell body, as shown in the inset of Fig. 3.7. The small radius is set to be the same size or few μm larger than the ROI radius, and R is set to 33 μm, although variations on the choice of R did not show significant differences in the resulting calcium traces.

For each time point the average pixel value across the background subtracted M pixels belonging to the annular region is used as a measure of the background fluorescence F_{back} and subtracted from the average cell body activity in the calculation of the fluorescence trace:

$$\Delta F = F_{ROI} - F - F_{back}, \tag{3.7}$$

and the total calcium trace is expressed as $\Delta F/F$. This prevents the activity of individual cells on the annular region to affect the calcium trace calculation while removing contributions from background fluctuations and out of plane cell activations.

Finally the temporal average of the each calcium trace is calculated excluding any fluctuations above and below twice the RMS value of each 5 minute experiment (typically constituted by the calcium transients), and this temporal average is subtracted from each trace.

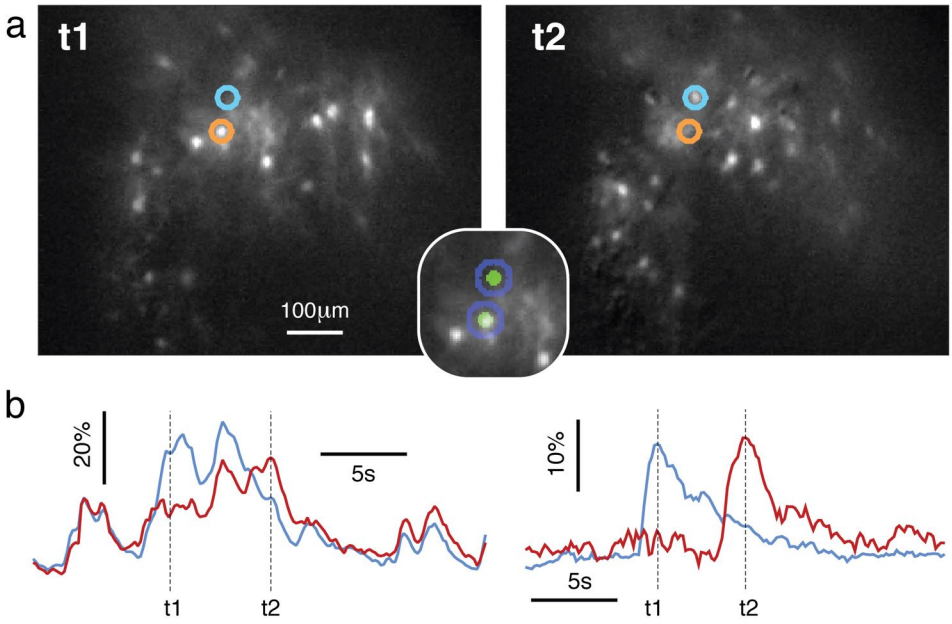

Figure 3.7. **a**, detail of the field of view in two separate time instants $t1$ and $t2$, highlighting two different cells and, in the inset, their respective ROI and reference annular region. **b**, the calcium traces $\Delta F/F$ for the two highlighted neurons as calculated with the proposed algorithm (solid lines), and the average F_{ROI}/F.

3.1.4 Decoding Action Potentials

In calcium imaging recordings the dynamics of calcium transients are typically one order of magnitude slower than the underlying AP spikes, however as this imaging technique is becoming more powerful in neural ensemble connectivity analysis, several decoding methods have been proposed to reconstruct with different levels of accuracy and complexity the underlying APs dynamics. The simplest way to infer the underlying action potentials from the calcium trace is by thresholding the time derivative of the $\Delta F/F$ trace, which has been proven to be a reliable method for detecting APs up to 50Hz in neocortical brain slices [53].

A typical ΔF/F calcium trace is characterized by a series of fast rising, slowly decaying transients over a constant baseline (Fig. 3.8). These transients are described to a good approximation as a simple convolution. With higher sampling rates it has

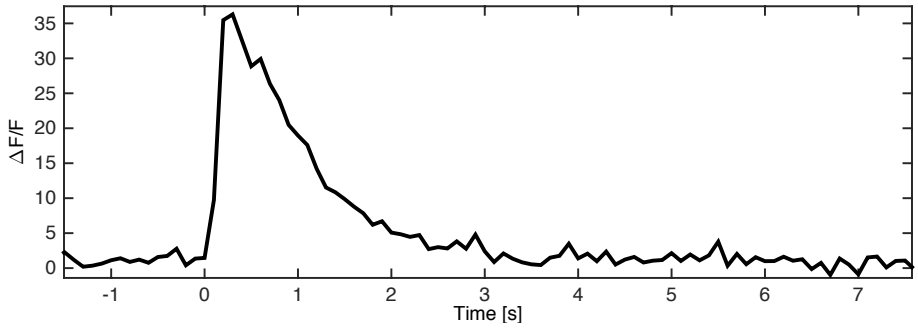

Figure 3.8. Typical transient observed in a fluorescence trace.

been proved by direct comparison of 2-photon calcium imaging and electrophysiological recordings that single APs up to 20Hz can be inferred from the fluorescent trace by iteratively "peeling" off single AP-evoked transients from the calcium signal [54].

3.2 Cell Clustering

One of the main advantages of calcium imaging over electrophysiological recordings is the ability to clearly distinguish and chronically track the activity of a large number of targeted neurons (several hundreds to a few thousands). This is reflected in the generation of very large datasets from which to mine qualitative information about neuronal circuit dynamics, cell-to-cell interaction and behavioral correlation.

An important step in assessing the recorded neural activity at a population level is to ask whether neuronal ensembles can be functionally clustered together according to some statistical parameters such as pairwise neural activity correlation, synchronous activation or correlation with behavioral data.

One of the most popular clustering techniques used in machine learning is the k-means algorithm [55–57] which has been applied to functional cell clustering in [58] and [59], showing in both cases a strong correspondence between functional and spatial clustering.

3.2.1 k-means Clustering

The most popular unsupervised partitional clustering algorithm in machine learning is k-means clustering. In the basic k-means algorithm [55, 56], given a dataset $\mathcal{D}$ of N M-dimensional observations $\mathcal{D} = \{\mathbf{x}_1, \ldots, \mathbf{x}_N\}$ and an arbitrary number of clusters k, each element of the dataset is iteratively assigned to the cluster $\mathbf{c}_i$ that minimizes an objective function J, which is typically the sum of squared distances of each data point to the assigned cluster:

$$J = \sum_{n=1}^{N} \sum_{k=1}^{K} r_{nk} \|\mathbf{x}_n - \boldsymbol{\mu}_k\|^2, \tag{3.8}$$

where r_{nk} assigns to each data point the closer centroid. After setting the number of clusters K, the initial centroids $\boldsymbol{\mu}_k$, $k \in \{1, \ldots, K\}$ and the objective function J, the EM steps are performed iteratively, until some stopping criterion is met:

- *Expectation* step: data points are reassigned to the cluster with the closer centroid.
- *Maximization* step: cluster centroids $\boldsymbol{\mu}_k$ are recalculated as the mean of all data points $\mathbf{x}_n$ belonging to cluster k.

The steps of the basic k-means algorithm are outlined below, and a graphical representation of the algorithm is shown in Fig. 3.9.

Algorithm 1 k-means

1: Randomly initialize cluster centroids $\boldsymbol{\mu}_k$
2: **repeat**
3: Assign elements to closest cluster:
$\mathbf{c}_i = \{j : d(\mathbf{x}_j, \boldsymbol{\mu}_i) \leq d(\mathbf{x}_j, \boldsymbol{\mu}_l), l \neq i, j = 1, \ldots, N\}$
4: Update cluster centroids:
$\boldsymbol{\mu}_i = \frac{1}{|\mathbf{c}_i|} \sum_{j \in \mathbf{c}_i} \mathbf{x}_j, \forall i$
5: **until** Convergence

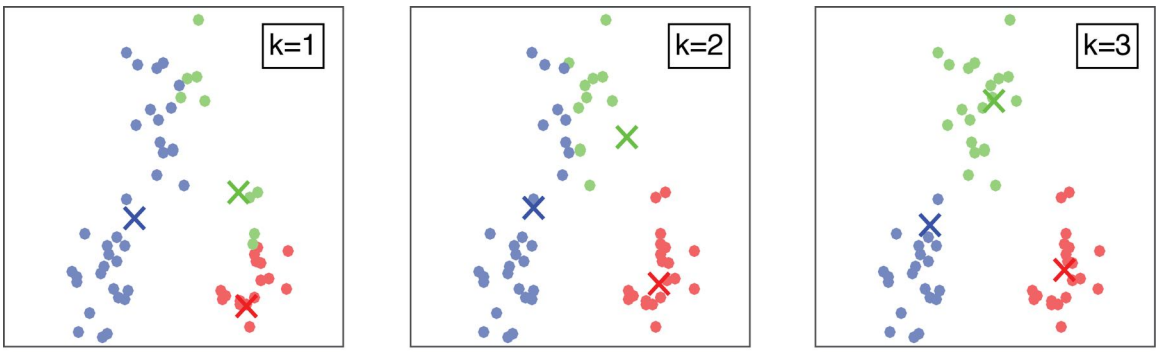

Figure 3.9. Illustration of three steps of the k-means algorithm applied to a two-dimensional dataset of 60 points. At each step the centroids are recalculated as the mean of all the members of their cluster.

Two key parameters in the k-means algorithm are the number of clusters k and the initial assignment of the centroids $\boldsymbol{\mu}_k$. Different configurations of the initial centroid positions can lead to different local minima of the cost function J, thus to different sub-optimal partitioning of the same input dataset $\mathcal{D}$. An efficient way of seeding the initial centroid positions is through the k-means++ D^2 weighting [60] algorithm, in which the centroids are initially placed sequentially with probability weighted on the squared distance from the closest previously chosen centroid (as opposed to the standard uniform distribution of the regular k-means). Efficient seeding and pre-processing of the data, such as whitening, has also been shown to have significant impact on the clustering results and convergence time [61].

In the analysis of calcium traces from large cell populations, we implemented a modified version of the k-means algorithm to group together functionally similar neuronal ensembles and analyze their overall activity, spatial distribution, behavioral correlation and activity change as an effect of acute cocaine injection.

Despite the deterministic nature of the k-means algorithm, the same dataset could yield different sub-optimum clustering solutions at each run due to the specific random initial seeding. This problem is typically addressed by iteratively applying the algorithm to the same dataset and choosing the best clustering solution, according

to the specific cost function used or a clustering evaluation index such as the Dunn's index or the silhouette function. The other main source of variability in the outcome of the k-means algorithm is the a priori choice of the number of clusters k. To address both issues we propose a modified meta-k-means algorithm [58], which improves the robustness to initial seeding and choice of k by iteratively applying the k-means algorithm both within the same dataset and across different randomly sampled datasets corresponding to the same experimental conditions.

3.2.2 Meta k-means

The idea behind the meta-k-means algorithm [58] is to use a two-step process to first find a set of clustering patterns which minimizes the cost function for the entire dataset (based on some specific initial conditions), and then merge these clusters together, based on the total occurrences of pairwise matching and the minimization of a clustering index.

Specifically, after running the k-means 1000 times on the entire dataset with different initial conditions seeded with k-means++ [60], a co-occurence matrix is constructed filling each entry with the total number of times two cells are clustered

Algorithm 2 Meta k-means

for i=1:1000 **do**
  Initialize cluster centroids $\boldsymbol{\mu}_k$ with k-means++
  repeat
    Assign elements to closest cluster:
    $\mathbf{c}_i = \{j : d(\mathbf{x}_j, \boldsymbol{\mu}_i) \leq d(\mathbf{x}_j, \boldsymbol{\mu}_l), l \neq i, j = 1, \ldots, N\}$
    Update cluster centroids:
    $\boldsymbol{\mu}_i = \frac{1}{|\mathbf{c}_i|} \sum_{j \in \mathbf{c}_i} \mathbf{x}_j, \forall i$
  until Convergence
end for
Generate co-occurence matrix and create meta-clusters
repeat
  Merge two most similar clusters
until $DI(k+1) > DI(k)$

together. Elements which are clustered together more than 80% of the times are grouped in meta-clusters, and the two most similar meta clusters are merged together until this operation does not further increase the Dunn's index of the clustering scheme.

Several limitations affect the applicability of this algorithm to a generic neural activity dataset: the main issue is the repeatability of the output clustering scheme for subsets of the same experimental dataset. The robustness of the clustering outcome for different subsamples of neural activity traces should be one of the key cluster quality measures, as cluster consistency is a fundamental requisite and justification for drawing any biologically relevant conclusion on groups of cells with similar activity. Even though the meta k-means shows good repeatability on the same dataset (Fig. 3.10a and Tab. 3.1), the co-occurence matrices associated with neural traces from different imaging sessions were significantly different, resulting in different final clustering schemes (Fig. 3.10b and Tab. 3.1).

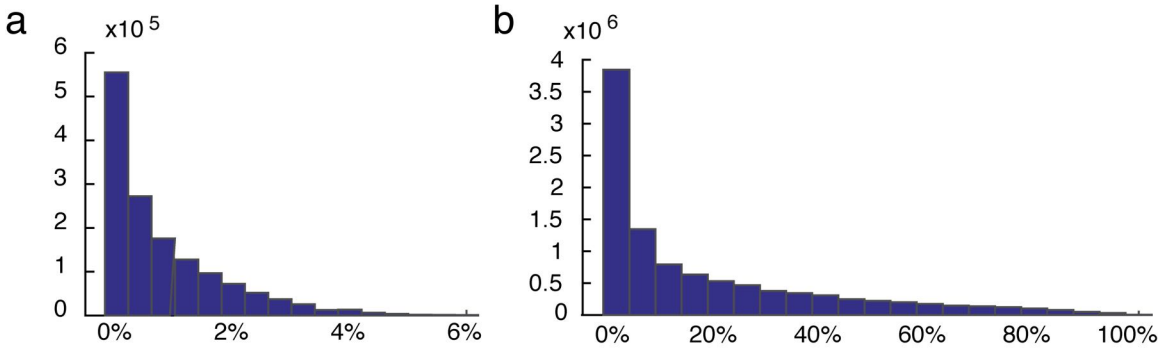

Figure 3.10. Distribution of the error for the meta k-means algorithm: the histograms show the distribution of the difference in absolute value (expressed in percentage) for every cell pairing of a representative D2 mouse within the same day (**a**) and across different days (**b**). The long tail in the inter-day distribution of the error indicates that the clustering algorithm finds similarity related to contingent experimental condition more than a partitioning scheme of general validity.

Another issue that arises in the application of the meta k-means algorithm to a generic dataset is the choice of k: in [58] was arbitrarily set to 3, whereas in [59]

Table 3.1. Mean and standard deviation (in percentage) of the absolute difference in each element of the co-occurence matrix generated with the meta k-means algorithm comparing the recordings in 5 different days: although the variation within the same dataset (diagonal terms) is less than 1% in average, the large difference in the co-occurrence matrix across different days suggests that this clustering approach is not suitable for finding common functional traits on the single cell activity which are not dependent on the contingent experimental conditions.

	D1	D2	D3	D4	D5
D1	0.99 ± 1.11	22.61 ± 24.34	20.04 ± 23.76	19.17 ± 21.11	20.56 ± 24.10
D2	22.61 ± 24.34	0.70 ± 0.83	22.73 ± 25.91	22.17 ± 23.31	22.35 ± 24.49
D3	20.04 ± 23.76	22.73 ± 25.91	0.90 ± 0.98	17.16 ± 19.49	19.48 ± 23.26
D4	19.17 ± 21.11	22.17 ± 23.31	17.16 ± 19.49	0.89 ± 1.09	18.46 ± 19.77
D5	20.56 ± 24.10	22.35 ± 24.48	19.48 ± 23.26	18.46 ± 19.77	0.81 ± 0.97

$k = 4$ produced more consistent results. However it is not clear what could be a good criterion for the choice of general validity.

Finally, the value of the threshold T for the co-occurence matrix also has a significant impact in the final clustering organization, not only in terms of number of elements that are left out of the meta-clusters, but also in terms of partitioning scheme. Its dependence on k makes its choice even more problematic, as setting it to an arbitrary percentage (the approach followed in [58]) would not be a robust solution for any dataset.

In the proposed algorithm we address these three issue proposing a solution which offers more consistent clustering both within the same dataset and across different experimental conditions (e.g. different mouse or cell types).

3.2.3 Proposed Algorithm

To improve the consistency across different datasets (e.g. single imaging session or single daily session), we chose a different approach by iteratively applying k-means algorithm to randomly sampled subsets of the dataset.

The cell clustering process presented here is comprised of two main steps: first the full dataset $\mathcal{D} \in \mathbb{R}^{N \times M}$ is segmented into 1000 subsequences of dimension $\mathbb{R}^{P \times M}$ with $P = 300$, corresponding to 30 s sequences of the neural activity for M cells. For each sequence the best clustering which minimizes the correlation between the calcium traces of each of the M neurons and the cluster centroid is found by iteratively applying the k-means++ algorithm for 100 different random seedings, and selecting the clustering solution which minimizes the cost function. This results in the generation of 1000 different clustering schemes from separate sequences within the same large dataset, which are used to create the pairwise co-occurrence map representing the percentage of times two cells are grouped in the same cluster. The proposed algorithm is summarized below.

Algorithm 3 Proposed algorithm

for i=1:1000 **do**
  Select sample from dataset
  for j=1:100 **do**
    Initialize cluster centroids $\boldsymbol{\mu}_k$ with k-means++
    repeat
      Assign elements to closest cluster:
      $\mathbf{c}_i = \{j : d(\mathbf{x}_j, \boldsymbol{\mu}_i) \leq d(\mathbf{x}_j, \boldsymbol{\mu}_l), l \neq i, j = 1, \ldots, N\}$
      Update cluster centroids:
      $\boldsymbol{\mu}_i = \frac{1}{|\mathbf{c}_i|} \sum_{j \in \mathbf{c}_i} \mathbf{x}_j, \forall i$
    until Convergence
  end for
end for
Generate co-occurence matrix
Calculate optimal threshold T and generate meta clusters

The effects of the dataset dimensionality reduction and the application of the meta k-means to sub-sequences of the entire dataset are a significant improvement in the inter-dataset cluster consistency (e.g. same experimental conditions across different days), which ultimately leads to a more robust clustering scheme. Despite a slight increase in the variability of the intra-dataset co-occurence matrix (Fig. 3.11a and Tab. 3.2, diagonal terms), the large inter-dataset variability observed with the

meta k-means is considerably reduced (Fig. 3.11b and Tab. 3.2, off-diagonal terms), resulting ultimately in the generation of more reliable meta clusters.

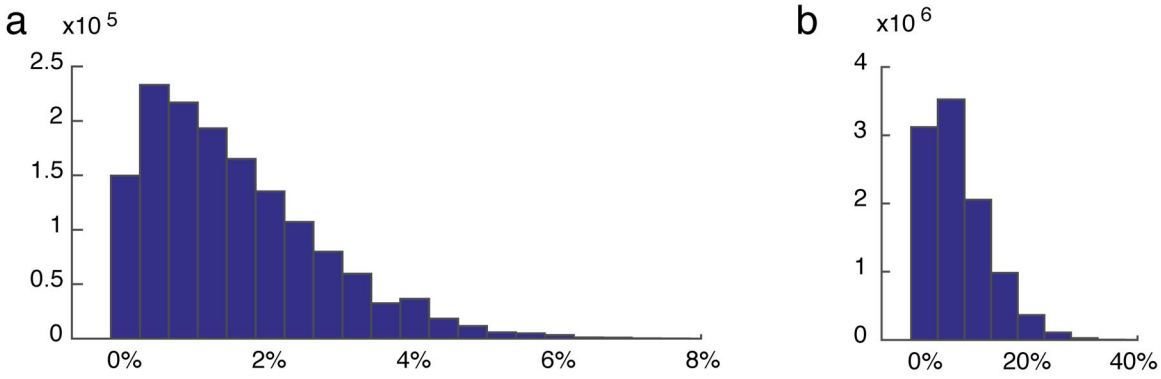

Figure 3.11. Distribution of the error for the proposed algorithm: the histograms show the distribution of the difference in absolute value (expressed in percentage) for every cell pairing of a representative D2 mouse within the same day (**a**) and across different days (**b**). The long tail in the inter-day distribution of the error indicates that the clustering algorithm finds similarity related to contingent experimental condition more than a partitioning scheme of general validity.

Table 3.2. Mean and standard deviation (in percentage) of the absolute difference in each element of the co-occurence matrix generated with the proposed algorithm, comparing the recordings in 5 different days: compared to the meta k-means algorithm (Tab. 3.1), the clustering consistency across different datasets (off diagonal terms) is significantly improved.

	D1	D2	D3	D4	D5
D1	1.53 ± 1.17	6.94 ± 5.28	7.15 ± 5.49	7.44 ± 5.75	7.24 ± 5.54
D1	6.94 ± 5.28	1.60 ± 1.21	7.55 ± 5.78	7.81 ± 5.96	7.34 ± 5.67
D3	7.15 ± 5.49	7.55 ± 5.78	1.55 ± 1.19	7.21 ± 5.64	7.04 ± 5.40
D4	7.44 ± 5.75	7.81 ± 5.96	7.21 ± 5.64	1.57 ± 1.21	7.33 ± 5.60
D5	7.24 ± 5.54	7.34 ± 5.67	7.04 ± 5.40	7.33 ± 5.60	1.52 ± 1.16

The minimization/maximization of some clustering index (such as the Dunn's index) as a mean to find the optimal k is an option only when very clear separation between cluster exists, which is typically the case only for synthetic datasets. In the case of neural activity analysis, one could not expect such a clear functional

demarcation between groups of neurons, and the local maxima/minima as a function of k would be too broad and sensitive to contingent aspects of the dataset be a reliable indicator of the optimal number of clusters (Fig. 3.12).

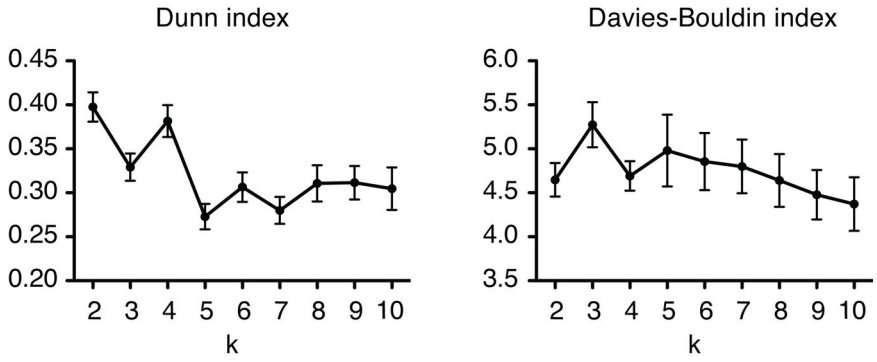

Figure 3.12. Dunn index and Davies-Bouldin index fail to recognize the number of clusters which best explain neural activity data. The low inter-cluster separation in real datasets results in broad peaks which cannot be reliably used to detect the optimal k^*. Error bars represent SD, N=20.

Before discussing different approaches in the choice of the number of clusters k it should be noted that a neuron cluster as defined here does not necessarily correspond to identifiable common anatomical or structural characteristics. In fact in this work neuronal clustering is solely based on the statistical description of single cell's neural activity, which is also the metric used to evaluate the clustering accuracy and compactness.

A typical choice when no a priori information is available is to set $k = \sqrt{M}$. For the dataset under study, even though the choice of a low value for k (< 5) could in some cases result in an irregular clustering (typically few large clusters or too many unclustered cells), the variability of the final clustering scheme was quite robust to the choice of k for values around $k = \sqrt{M}$, where the Rand index between different outcomes of the proposed clustering algorithm plateaus at its maximum value (Fig. 3.13).

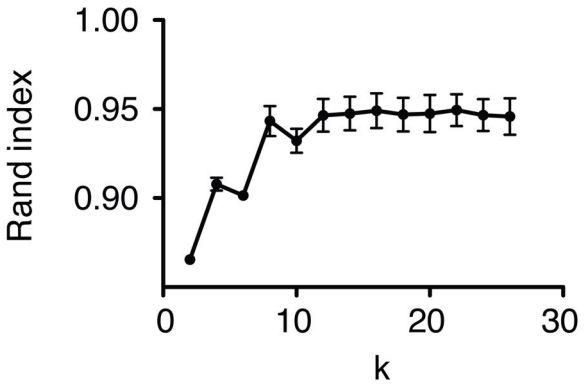

Figure 3.13. Average Rand index for the outcome of the proposed algorithm for different initial number of clusters k: the choice $k = \sqrt{M}$ was found to consistently yield similar results, where variations of k did not significantly impact the final clustering outcome. Error bars represent SEM, N=10.

The effect of T on the final clustering structure can be seen in Fig. 3.14a. Low values of T create one single meta-cluster with no unclustered cell (cells that are not consistently clustered with any other cell a sufficient number of times). As T increases so does the number of meta-clusters and unclustered cells (Fig. 3.14c), as well as the number of small clusters (with less than 3 neurons). Given the influence of T in the final clustering structure, it is important to establish heuristic methods to produce a clustering scheme that is consistent and robust to the choice of parameters and experimental conditions.

In our study we found that the choice $T = \arg\max_{T\in[01]} \frac{T_C}{NC}$ yields the most consistent results: the threshold index is chosen in order to maximize the total number of clusters T_C and penalize the number of unclustered cells NC.

The application of the proposed algorithm to the recorded neural dataset showed a significant overall improvement in consistency across different experiments (Fig 3.15), indicating better robustness to contingent experimental conditions. The adaptation of the meta k-means algorithm to the specific dataset under study produces more consistent clustering schemes when applied to the same dataset but considerably different partitioning schemes when applied to different dataset in similar experimental

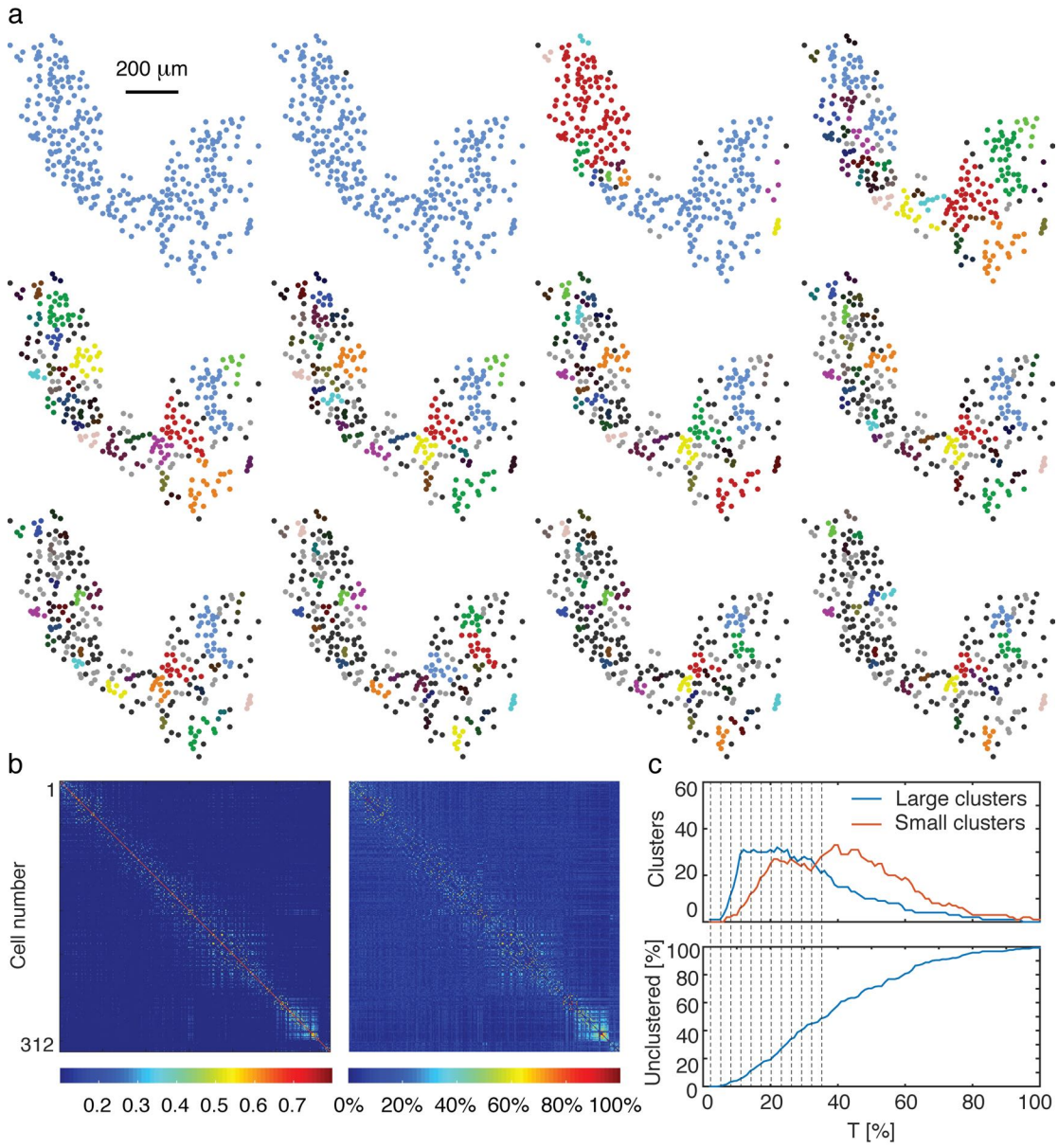

Figure 3.14. The effect of threshold T on clustering. **a**, 12 different clustering schemes generated with the 12 values of T highlighted by the dotted vertical lines in **c**. **b**, average pairwise correlation coefficient (left) and co-occurrence map (right), where each entry (i, j) represents the number of times cells i and j are clustered together. This co-occurrence map, as a result of the criterion used for the cluster update, resembles the average correlation matrix of the dataset. **c**, total number of clusters and small (less than 3 elements) clusters (top) and percentage of unclustered cells (bottom) as a function of the threshold T.

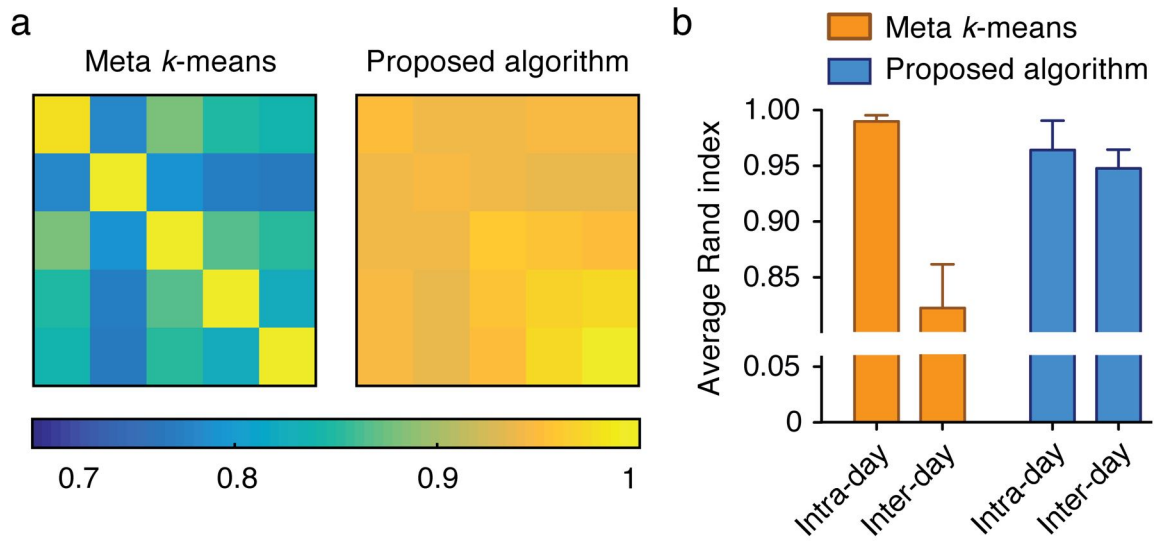

Figure 3.15. Comparison of the final clustering scheme of the proposed algorithm with the meta k-means. **a**, average Rand index for different runs of the clustering algorithm within the same dataset (diagonal terms) and across 5 different days (off-diagonal terms). Despite the high indices within the same dataset, the meta k-means algorithm has poor consistency for different datasets, indicating that it can only capture dataset-specific functional features of the neurons, but it fails to group cells according to a more general statistical description of the calcium traces. **b**, direct comparison of the average intra-dataset and inter-dataset Rand indices, showing a significant improvement in the overall consistency of the final clustering structure.

conditions, e.g., different days or imaging sessions. The reduction in dataset dimensionality and application of k-means to random samples of the full dataset avoids these type of overfitting of a specific dataset, capturing a more general statistical relation between single cell calcium traces.

The use of cell clustering is a way to simplify the analysis of neural activity of large cell populations and their effect on specific behaviors, based on the hypothesis that cells with similar calcium transients and highly correlated activity can be grouped together for reducing the data dimensionality. Under these circumstances, if there is no consistency between different datasets in similar experimental conditions, the validity of any biologically relevant conclusion derived from the considered clustering scheme is debatable. The proposed algorithm proved to be able to partition neurons

according to general statistical features which hold valid across all the considered imaging sessions, providing confidence to the faithfulness of the results derived from this type of analysis.

3.2.4 Cluster Validation

A crucial issue in clustering is how to evaluate the outcome of a specific clustering technique, or how to assess the effect of a parameter change − most importantly the number of clusters k − on the outcome of the clustering algorithm under study. This will ultimately define the quality and reliability of the data interpretation suggested by the chosen algorithm. In this section we discuss and compare the main cluster validation techniques, both in a general context and restricting the analysis to the case of neuronal functional clustering, by testing the proposed clustering method on both on synthetic datasets and real neural activity traces.

Cluster validity methods can be divided into three categories, depending whether they are based on external criteria, if the clustering results are compared to a reference dataset whose structure and partitioning are known, internal criteria, if the clustering assessment relies on quality measures calculated on the considered dataset only, or relative criteria, if different results are compared for different sets of parameters or clustering schemes [62, 63].

Although all three methods can be equally useful in assessing the clustering quality of a specific algorithm, some caution needs to be used especially when dealing with internal validation techniques, as the value of an index calculated on a single dataset might not translate in an absolute clustering quality measure in terms of data interpretation. In the present work we use both external validation techniques on a well defined synthetic dataset and internal validation methods on the real calcium traces for assessing the quality of the proposed clustering technique.

The fundamental assumption underlying most clustering validation methods is that elements belonging to the same cluster should have similar characteristics (ac-

cording to some chosen metric), and elements belonging to different clusters should be dissimilar. The quality of clustering is typically expressed through an index which penalizes inter-cluster similarities and promotes intra-cluster homogeneity, measured with the same metric used in the cluster generation algorithm. A typical procedure for finding the optimal number of clusters K^* is to plot the index as a function of the number of clusters and find local or global maxima or minima (depending on the specific index used). Some indices are independent of the number of clusters, but others show a trend (increasing or decreasing) as the number of clusters varies. In this case K^* can be found as a local minimum/maximum or knee on the index function. If no clear deviation from the trend exists it is possible that the underlying data does not present any well separated clusters.

Below are presented the most common clustering validation techniques and indices used in external, internal and relative criteria based methods.

Hubert's Γ Statistic. A common method for comparing clustering schemes in both external and internal criteria validation is the Hubert's Γ statistic, which compares the matrices X and Y as follows:

$$\Gamma = \frac{1}{M} \sum_{i=1}^{N-1} \sum_{j=i+1}^{N} X(i,j)Y(i,j), \tag{3.9}$$

where $M = N(N-1)/2$ is the total number of pairwise connections between neurons. When used with external validation methods, the X and Y matrices under comparison are the proximity matrix and the reference partition matrix for the dataset[2]. In the case of internal validation (i.e. when no reference partition matrix is available), the Hubert's Γ statistic typically correlates the proximity matrix of the dataset with a matrix containing the distances between the clusters datapoints i and j belong to. A

[2]In a partition matrix the ij-th element is 1 if datapoints i and j belong to the same partition, 0 otherwise.

high value of Γ denotes compact clusters, thus when using this metric to evaluate the optimal number of clusters K^* the index should be maximized.

Similarly, the normalized Hubert's Γ statistic, restricted to the range of ± 1, is defined as

$$\bar{\Gamma} = \frac{1}{M} \sum_{i=1}^{N-1} \sum_{j=i+1}^{N} \frac{(X(i,j) - \mu_X)(Y(i,j) - \mu_Y)}{\sigma_X \sigma_Y}, \tag{3.10}$$

where μ_X, μ_Y and σ_X, σ_Y are, respectively, the sample mean and standard deviation of matrices X and Y.

Silhouette Method. Silhouettes are a graphical method to compare the average within-cluster dissimilarity versus the average between-cluster dissimilarity. This method was first introduced in [64], and its usefulness relies on the fact that the underlying clusters are known to be clearly separated.

The typical metric used for assessing the dissimilarity between a datapoint i and any other data point belonging to the same cluster $-$ $a(i)$ $-$ or to a different cluster $-$ $b(i)$ $-$ is the Euclidean distance. After defining the average intra-cluster dissimilarity $a(i)$ for every element i as the average distance between i and every other element belonging to the same cluster A, and the average inter-cluster dissimilarity $b(i)$ for every element i as the minimum average distance of i with all the elements of the closer cluster C with $C \neq A$, the silhouette value for i can be calculated as

$$s(i) = \frac{b(i) - a(i)}{\max\{b(i), a(i)\}}, \tag{3.11}$$

resulting in a value ranging from -1, for data points which are in average much closer to the closer cluster than the cluster they have been assigned to (and thus likely to have been misclassified), to 1, for data points which are in average much closer to the

elements of their own cluster than the elements of the closest cluster. The silhouette index is defined as the average of $s(i)$ for all the points N in the dataset:

$$SI = \frac{1}{N}\sum_{i=1}^{N} s(i). \tag{3.12}$$

Dunn's Index. Dunn's index, introduced in [65] as a clustering quality metric for compact and well separated clusters, is defined as:

$$DI = \min_{1\leq i\leq K}\left\{\min_{i+1\leq j\leq K, j\neq i}\left\{\frac{\delta(C_i, C_j)}{\max_{1\leq k\leq K}\Delta(C_k)}\right\}\right\}, \tag{3.13}$$

where the set distance between cluster C_i and C_j is the distance between the two closest elements belonging to cluster C_i and C_j:

$$\delta(C_i, C_j) \equiv \min_{x\in C_i, y\in C_j} d(\mathbf{x}, \mathbf{y}), \tag{3.14}$$

and the diameter of cluster k is the distance between the two farthermost elements in cluster C_k:

$$\Delta(C_k) \equiv \max_{x,y\in C_k} d(\mathbf{x}, \mathbf{y}). \tag{3.15}$$

In the most general form any metric can be chosen to express the distance $d(\mathbf{x}, \mathbf{y})$, as long as it is consistent with the metric used in the cluster generation algorithm.

Based on Equation (3.13) it is clear that low intra-cluster variance and large inter-cluster distance translate into large values of the Dunn's index, and since the number of clusters does not affect the index, the value of k corresponding to the global maximum is the number of clusters which best describes the dataset under study. As is the case for most of the internal criterion indices, the computational burden associated with the calculation of the Dunn's index is considerable, especially when considered in the setting of a statistical analysis, such as for the case of finding

optimal clustering parameters using relative criteria validation methods. Another important aspect to consider when using the Dunn's index is the intrinsic sensitivity to noise which is due to the worst case scenario nature of such index: in the case of outliers or noisy measurements, the denominator in Equation (3.13) can grow excessively large, providing an inaccurate measure and underestimating the overall cluster quality.

In order to improve its robustness to noise, several variants of the Dunn's index have been proposed [66], by applying different definitions of the set distance and cluster diameter: in its original form of Equation (3.14), the set distance $\delta(C_i, C_j)$ is defined as the *single link* interpretation of inter-cluster separation (i.e. the distance between the two closest members of C_i and C_j). The other two variants of cluster separation measure are the *complete linkage*, which considers the distance between the farthermost members of C_i and C_j with similar computational cost, and the *average linkage*, which measures the average centroid to centroid distance at a reduced computational expense. Similarly, the single measure used for the cluster diameter in the original form of the index can be replaced by the average of all the cluster member-to-member distances or cluster member-to-centroid distances to reduce the effect of noisy datapoints on the overall index value.

Davies-Bouldin Index. The Davies-Bouldin index [67] expresses the ratio of a within-cluster dispersion measure S_i for cluster i over an inter-cluster separation measure $M_{i,j}$ between clusters i and j. These two measures can be written, in the most general form, as:

$$S_i = \left\{ \frac{1}{T_i} \sum_{j=1}^{T_i} |x_j - A_i|^q \right\}^{1/q} \tag{3.16}$$

and

$$M_{ij} = \left\{ \sum_{k=1}^{n} |a_{ki} - a_{kj}|^p \right\}^{1/p}, \tag{3.17}$$

where T_i is the size of cluster C_i, x_j is one of $n-$dimensional elements of cluster C_i, A_i is its centroid, and a_{ki} is the $k-$th component of the $n-$dimensional centroid of cluster C_i. In the case of $p = 2$, M_{ij} becomes the Euclidean distance between cluster C_i and C_j. For $q = 1$ the intra-cluster dispersion measure becomes the average Euclidean distance between all elements of a cluster and its centroid. The quality of clustering is then measured for every pair of clusters as

$$R_{ij} = \frac{S_i + S_j}{M_{ij}}, \tag{3.18}$$

and the Davies-Bouldin index is defined as the average of this cluster similarity measure calculated for every cluster with its most similar cluster:

$$DB = \frac{1}{K} \sum_{i=1}^{K} \max_{i \neq j} R_{ij}. \tag{3.19}$$

Therefore a lower index value indicates better cluster separation. It is important to notice how this definition of intra-cluster dispersion measure yields a zero value in the particular case of single element clusters. Thus the Davies-Bouldin index reaches its global minimum at zero in the undesirable scenario of all clusters containing at most one element of the dataset.

Maulik-Bandyopadhyay Index. Also referred to as the $\mathcal{I}$ index, the Maulik-Bandyopadhyay index [68] is the product of three terms and defined as:

$$MB(K) = \left(\frac{1}{K} \cdot \frac{E_1}{E_K} \cdot D_K \right)^p, \tag{3.20}$$

where the first term $\frac{1}{K}$ penalizes a large number of clusters K, the second term is the ratio betweenE_1 (which is constant across different K) and the intra-cluster variance E_K, and the last term measures the cluster separation. The power p is typically set

to 2. The intra-cluster distance E_K an the inter-cluster separation D_K are defined, respectively, as

$$E_K = \sum_{k=1}^{K} \sum_{j=1}^{N} u_{kj} \|x_j - A_k\| \tag{3.21}$$

and

$$D_K = \max_{i,j=1}^{K} \|A_i - A_j\| \tag{3.22}$$

where, following the same convention used above, N is the total number of points in the dataset, u_{kj} is the kj-th element of the partition matrix $U(K) \in \mathbb{R}^{K \times N}$, x_j is the j-th element of the dataset and A_k is the centroid of cluster k.

Matching Measures. Based on the pair-wise matching definitions of true positive (TP), true negative (TN), false positive (FP) and false negative (FN), the following validity index are defined for external validation methods:

Jaccard coefficient. It measures the true positive ratio ignoring true negatives, and its maximum and ideal value (when there are no false positive or false negatives) is 1:

$$JC = \frac{TP}{TP + FN + FP}. \tag{3.23}$$

Rand statistic. Similar to the Jaccard index but it considers the ratio of true positives and true negatives over all possible pairings of the N datapoints. It reaches its maximum at 1 only in the case of perfect clustering:

$$RC = \frac{TP + TN}{M}. \tag{3.24}$$

Fowlkes-Mallows index. Originally proposed as a hierarchical clustering validation method, it can be extended to non-hierarchical clustering techniques in the general form:

$$FM = \sqrt{\frac{TP}{TP + FP} \cdot \frac{TP}{TP + FN}}, \tag{3.25}$$

which represents the geometric mean of precision (the ratio of the true positives over the total number of pairwise combinations in the same cluster) and recall (the ratio of the true positives over the total number of pairwise combinations in the same partition).

In presence of noisy data the Fowlkes-Mallows index provides more accurate results compared to the previous two coefficients.

3.3 Activity Synchronization and Population-Level Analysis

The study of pairwise correlation of calcium traces gives some insight on the level of interconnection of individual neurons, (i.e. how likely are two neurons to be active at the same time), however it fails to capture the degree of synchronization of neuronal ensembles, which can be used as an important parameter to characterize neuronal circuits anatomy and functional connections. In this section we discuss alternative methods to quantify the neuron to neuron interaction at a population level based on the activity synchronization, and compare the results with the correlation-based methods presented above.

3.3.1 Calculating Neural Coactivations

The single calcium traces (derived from the raw images as described in section 3.1.3) are converted to a binary matrix where each calcium transient is represented by a single datapoint located at the crossing of the 5% ΔF/F threshold. The choice for this value is based on three times the average RMS of all calcium traces baselines (see section 4.1.2 for details). In order to compensate for the ± 1 frame uncertainty in the onset of the calcium transient, each event is represented in the binary sequence as a 300 ms pulse centered on the threshold crossing point. In pairwise cell analysis, two events are considered to be simultaneous if they overlap during at least on time instant. A typical binary matrix showing neuronal coactivations is presented in Fig.

3.16, top row. As expected, there is a clear correlation between the average neural activity and the number of cells active simultaneously (Fig. 3.16, middle row).

For a statistical analysis of the degree of synchronization between all the cells in the field of view it is desirable to have a reference statistic to compare against, typically derived from the assumption of independent neuronal activations. In [69] and [70] the authors use Monte Carlo simulations to reject the hypothesis of independent spontaneous activity in the cortical region. Examples of natural test statistics which can be used to describe the level of neuronal synchronization include the total number of pairwise simultaneous activations, the maximum number of activations during a specific time interval ΔT (typically set to the length of each experiment, $\Delta T = 300$ s), the ratio $T_i/\Delta T$, where T_i is the total time of inactivity, or $T_1/\Delta T$, where T_1 is the time during which a minimum number of cells N_s is simultaneously active.

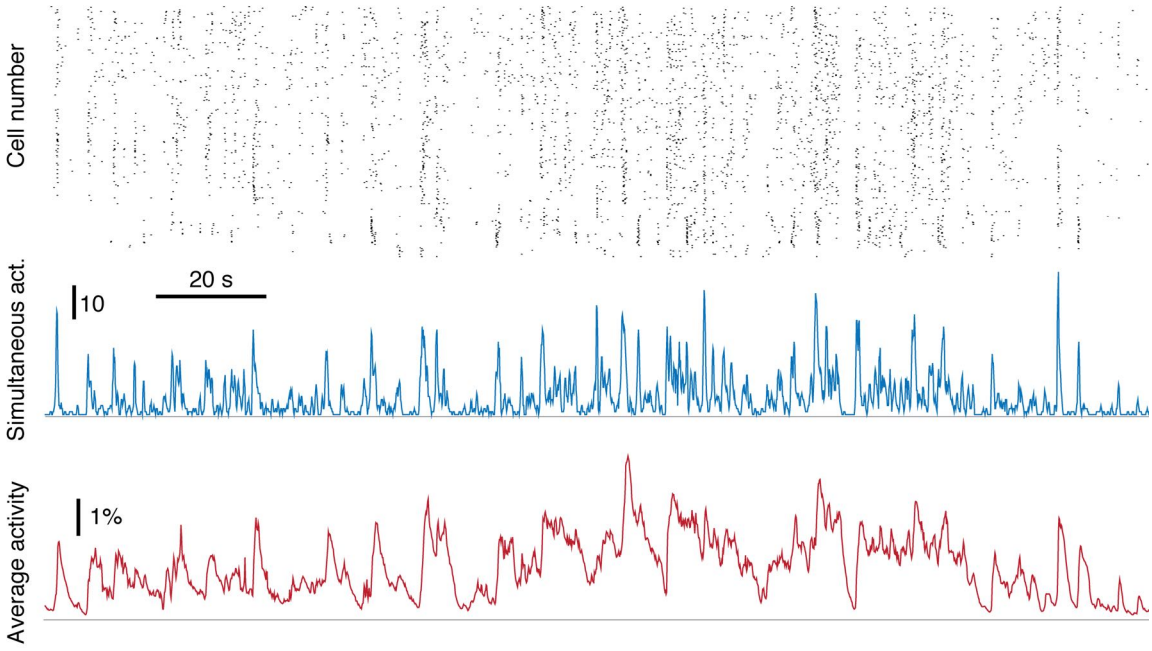

Figure 3.16. Activity synchronization analysis. *Top row*: binary representation of single calcium transient events for a sample D2 mouse. *Middle row*: total number of pairwise synchronous neural activations. *Bottom row*: average fluorescence trace for the 312 neurons in the field of view.

A critical issue in analyzing calcium imaging data is the extremely low rate of calcium events per cell (0.6834 ± 0.9220 activations per minute for D1 cells, 1.0849 ± 1.1399 for D2 cells) which makes statistical analysis of neuronal activity at a single cell level particularly challenging even for large datasets.

To address these issues, the data was filtered in order to exclude from the analysis cells with minimal firing rate (less than 3 every 15 minutes) and spurious simultaneous activations patterns which could be ascribed to multiple events just randomly occurring at the same time.

4. *IN VIVO* IMAGING: THE ROLE OF STRIATAL NEURONAL CIRCUITS IN LOCOMOTOR ACTIVITY

In this chapter we apply the imaging system developed alongside the data analysis techniques presented in the previous chapter to perform a functional study of the dorsal striatum neuronal circuit in the mouse brain.

The striatum is the input structure to the basal ganglia, a group of subcortical nuclei which includes also the globus pallidus, the subtalamic nucleus (STN) and the substantia nigra pars compacta (SNc) and pars reticulata (SNr) (Fig. 4.1). It integrates information from different cortical areas and subcortical regions and plays

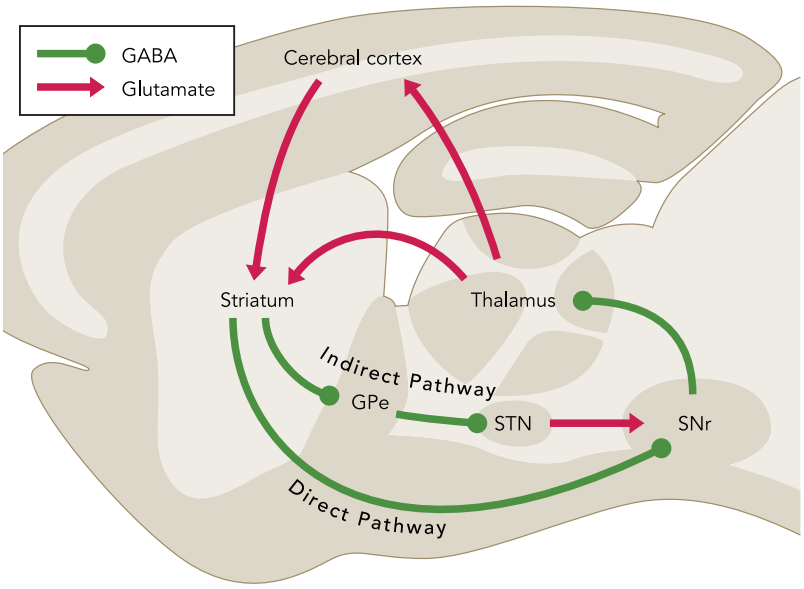

Figure 4.1. The structure of basal ganglia complex, showing the direct and indirect pathways [71].

a prominent role in the control of motor activity, habit formation and goal-directed behavior [72].

More than 95% of neurons in the striatum are GABAergic medium spiny neurons (MSN), which are divided into two subgroups of cells: neurons which express dopamine Drd1 receptors and constitute the direct pathway, projecting directly to the GPi and SNr, and neurons which express dopamine Drd2 receptors and constitute the indirect pathway, which projects to the GPe and connects to the SNr through the STN [71, 73, 74] (Fig 4.1). These pathways are also well known to play a key role (specifically in the ventral striatum) in mediating reward related stimuli associated with drug abuse [75]. The striatum is also involved in a number of neurological diseases associated with dysfunctions in locomotor activity, most importantly the Parkinson Disease [76] and its related motor deficits, in which the two striatal pathways play a crucial role.

Current *in vivo* studies of the direct and indirect pathways lack either the specificity (in the case of single unit recordings) or the single cell resolution (e.g. in the case of optogenetic stimulation) to assess in detail the function of such neural circuits and their effects on locomotor activity.

By integrating the imaging system developed in this work together with the data processing techniques presented above it was possible to overcome the limitations of traditional approaches and uncover in detail the function of striatal neural circuits as well as their relation with locomotor activity.

The experimental results are organized as follows: in the first part of the chapter we present the physiological neural activity in the direct and indirect pathway in freely moving mice, with focus on the heterogeneity of different cell ensembles and their distinct roles in locomotor activity. In the second part of the chapter we study the effect of cocaine on D1 and D2 neurons, revealing much more complex interactions and functional traits in D1 and D2 neural activity than what the traditional model could explain. Finally, using machine learning techniques we demonstrate how single

neuron activity in the dorsal striatum (especially D2 neurons) can explain and predict locomotor activity.

4.1 Physiological Activity of Direct and Indirect Pathway Striatal Neurons

In this section we analyze the physiological activity of D1 and D2 neurons in the dorsal striatum in freely behaving mice, serving the dual purpose of generating a reference dataset of spontaneous neural activity in the dorsal striatum during locomotion and demonstrating the practical effectiveness of the data analysis techniques presented above in the study of large neuronal populations.

4.1.1 Experimental Setup

We first tested the imaging system with open field tests, recording both neural activity and locomotor behavior through an overhead camera synchronized with the microscope.

We used two groups of mice: D1 cre mice to label direct pathway medium spiny neurons (D1 neurons), and D2 cre to label indirect pathway medium spiny neurons (D2 neurons). We injected cre dependent AAV GCaMP6s to D1 cre or D2 cre mice to selectively label D1 or D2 neurons of dorsal striatum with GCaMP6, respectively. Subsequently, we implanted gradient index (GRIN) lens above the dorsal striatum, and mounted the microscope above the GRIN lens (Fig. 4.2a). With this configuration, images from dorsal striatum were relayed via GRIN lens to the microscope (Fig. 4.2b). The spontaneous activity in the dorsal striatum was recorded in 17 mice during 5 days in two different experimental conditions, i.e. before and after IP injection of cocaine (20 mg/kg). The recording pattern for each day is shown in Fig. 4.3. This allowed for studying both the physiological features of the direct and indirect pathways with unprecedented detail, as well as the effect of cocaine on these neural

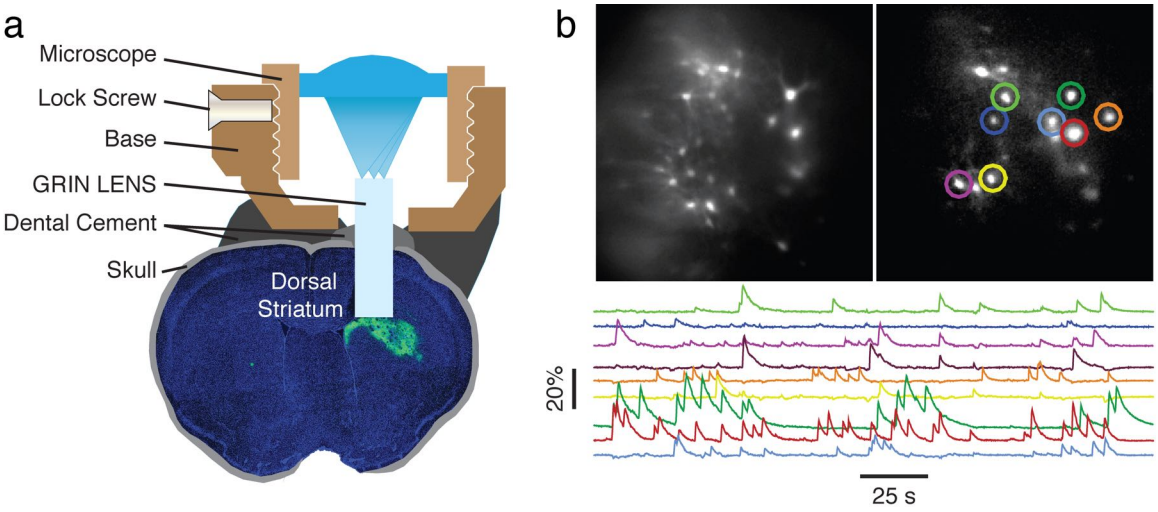

Figure 4.2. **a**, schematic of the microscope mounting on the mouse skull: the GRIN lens was first implanted at the desired depth and anchored with dental cement, then the microscope base was mounted on the mouse skull, and the microscope body was secured to the base through a set screw. In **b** (top panel) two different images are shown: on the left is the average of 5 sequential frames, highlighting the neurons active during a .5s period, and on the right, for the same brain area, a single frame shows the simultaneous activation of several neurons. A detail of the calcium traces for 8 of these neurons are plotted in the bottom panel.

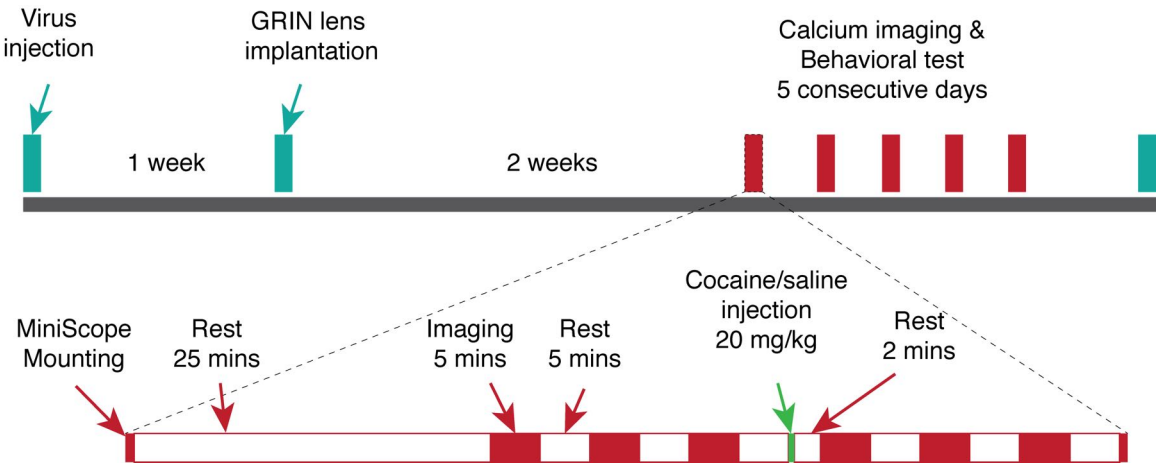

Figure 4.3. Schematic of the daily imaging recording sessions. The same procedure was repeated for 5 consecutive days for a total of 30 recording sessions.

circuits. Throughout this section only the data collected before cocaine injection is considered.

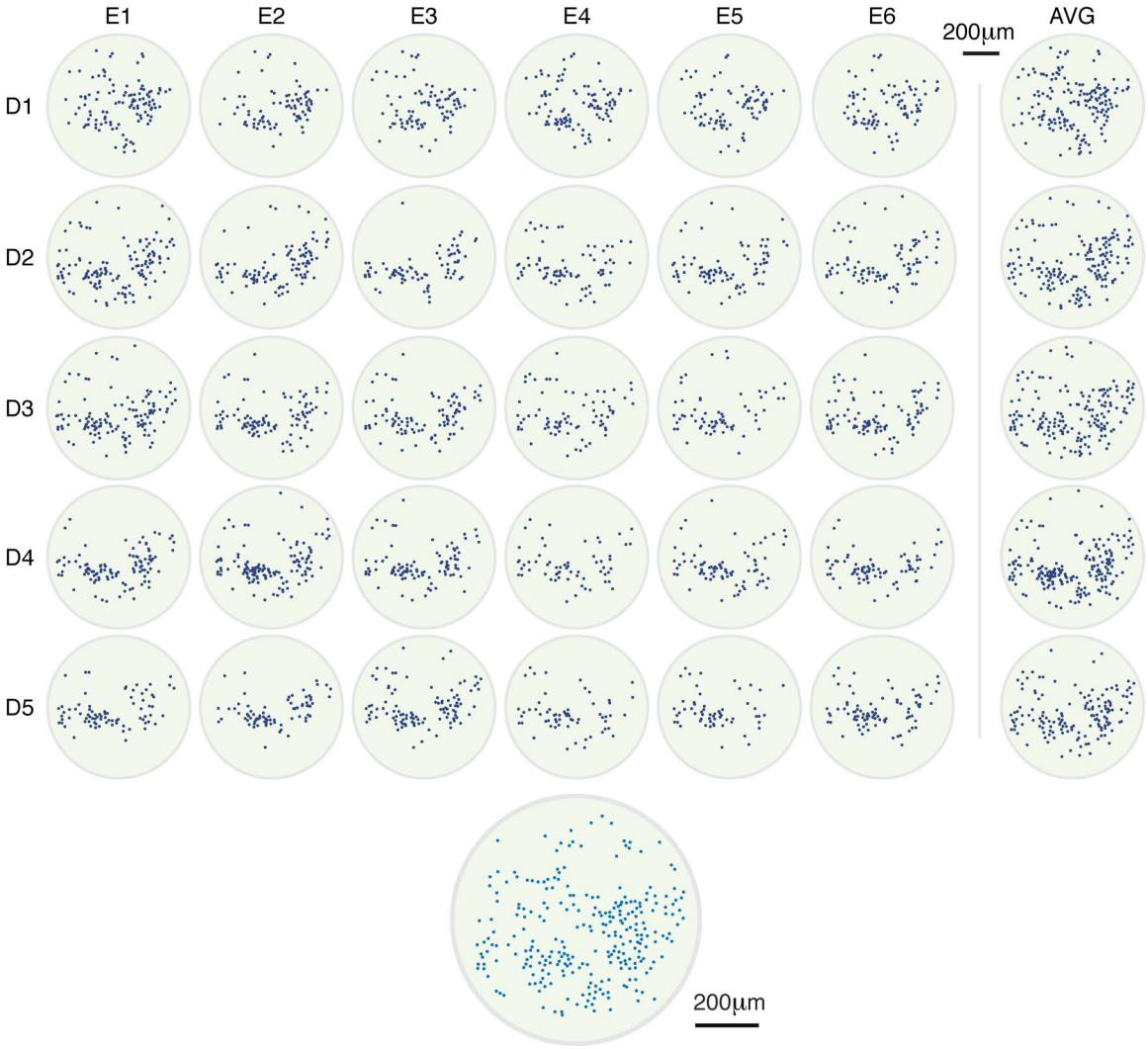

Figure 4.4. Cell map generation for a D1 mouse: rows correspond to different days and columns correspond to a single 5 minute experiment cell maps. The farthest right column shows the overall day map and on the bottom is the total cell map for all days.

4.1.2 Neural Activity Characterization

The steps outlined in Section 3.1 were applied to the raw images captured from the microscope to obtain a map of all active cells for each mouse as well as the calcium traces for each identified cell. After performing image registration along the x and y component of the image, for each 5 minute experiment a cell map was created following the algorithm described in Section 3.1.2. Each group of connected positive matches for x and y cell detection was treated as a single cell, its centroid was taken as the cell position, and a 2x2 pixel mask was overlayed for graphical representation (Fig. 4.4). An overall mask for each day was then generated by grouping together all the cells identified in all 6 experiments. Finally, a global cell mask was created merging the 5 overall day maps. With this procedure it was possible to track the

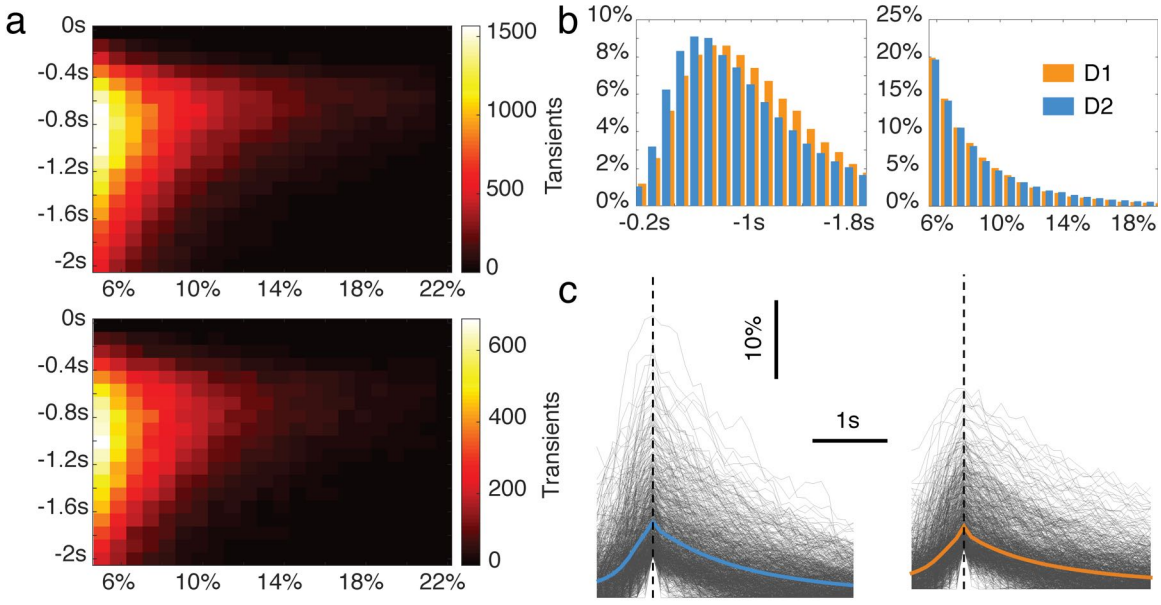

Figure 4.5. **a**, heatmap of the average time decay constant versus $\Delta F/F$ for D2 (top, $n = 39816$) and D1 (bottom, $n = 105288$). **b**, histogram summarizing the average time constant (left) and amplitude (right) for the calcium transients considered in **a**: the only noticeable difference is the slightly longer decay time of D1 neurons. In **c** a sample of 1000 calcium traces aligned at their peak are shown together with their average for D2 (left) and D1 (right) calcium peaks above $5\%\Delta F/F$.

activity of the same cells over long periods of time, a task which is at best daunting with any other traditional technique.

Once the cell map was available for every mouse, the individual neuron calcium traces were calculated according to the procedure outlined in Section 3.1.3. In general, calcium transients from D1 or D2 neurons displayed similar fluorescent amplitude (8.55% $\Delta F/F \pm 4.11\%$ s.d., n = 39816 for D1 neurons, 8.81% $\Delta F/F \pm 4.51\%$ s.d., n = 105288 for D2 neurons), and D1 neurons showed a slightly longer decay time (-1.01s $\pm$ 0.53s s.d. for D1, -0.94s $\pm$ 0.51s s.d. for D2), but no specific attributes were observed which could allow for isolating D1 or D2 cells based solely on their functional features (Fig. 4.5). Therefore, for simultaneous recording of direct and indirect pathway at single cell level the only option would be to label D1 and D2 neurons with two different indicators and collect the neural activity through a dual color microscope.

4.1.3 Direct and Indirect Pathway Activity and Locomotion

Although the importance of the concerted activity of the direct and indirect pathways in planning of locomotor activity rather than two independent opposing pathways is commonly recognized, the debate on the specific role and relationship between D1 and D2 neurons is still open, mainly due to the limitations in the investigation techniques currently available.

The rate-based dual circuit model of the basal ganglia postulates that increased mean firing rates of neurons in the striatal direct pathways facilitates locomotion, whereas that of the indirect pathway suppresses locomotion In this rate-based model, the mean firing rates of neurons is thought to encode information in the direct or indirect pathway. This model has been instrumental in unraveling basal ganglia function, but has recently been challenged [77], which has called for more detailed analysis of direct and indirect pathway function in vivo.

In [76] the authors used optogenetic stimulation to selectively activate D1 and D2 neurons in mouse model of Parkinson's desease, suggesting that the activation of the indirect pathway is associated with the expression of parkinsonian motor deficits (freezing, bradykinesia and decreased locomotor initiations), whereas stimulation of the direct pathway has the effect of recovering from these motor deficits and it is associated with an increase in locomotor activity.

The fact that direct and indirect pathway activity could not be explained by a simple dichotomy of functionally independent neural circuits has been recently observed in [77], where the authors using fiber optics and time-correlated single-photon counting (TCSPC) showed an increase in the overall activity for both D1 and D2 pathways when the mouse is engaged in behaviorally active tasks (e.g. lever pressing or turning). These observations were somewhat challenged by the optogenetic experiments carried out in [78]; however these results might not reflect the true physiological activation of the direct and indirect pathways, mainly because of the independent activation of D1 or D2 neurons only, and because of the large spatial span of neural activation, which could encompass cell subpopulations with different functional characteristics.

For these reasons, these findings only give a general picture of the direct and indirect pathway activity. In this study we unveil the functional traits of D1 and D2 neurons at much finer detail, proving that, in order to have a clear understanding of the big picture, an in depth study at single cell level is required by the great diversity and heterogeneity which characterized these neural circuits.

One of the common features observed in all the mice used in this study is the strong positive correlation between the overall neural activity in the dorsal striatum and the mouse velocity profile (Fig. 4.6). Specifically, all mice showed high neural activity during ambulation (defined for speeds above 2 cm/s) and much lower activity during immobility (defined for speeds below 0.05 cm/s, or twice the speed RMS value). Although this is an expected condition for D1 neurons, it challenges the classical model according to which the activation of the indirect pathway inhibits locomotor activity [79, 80].

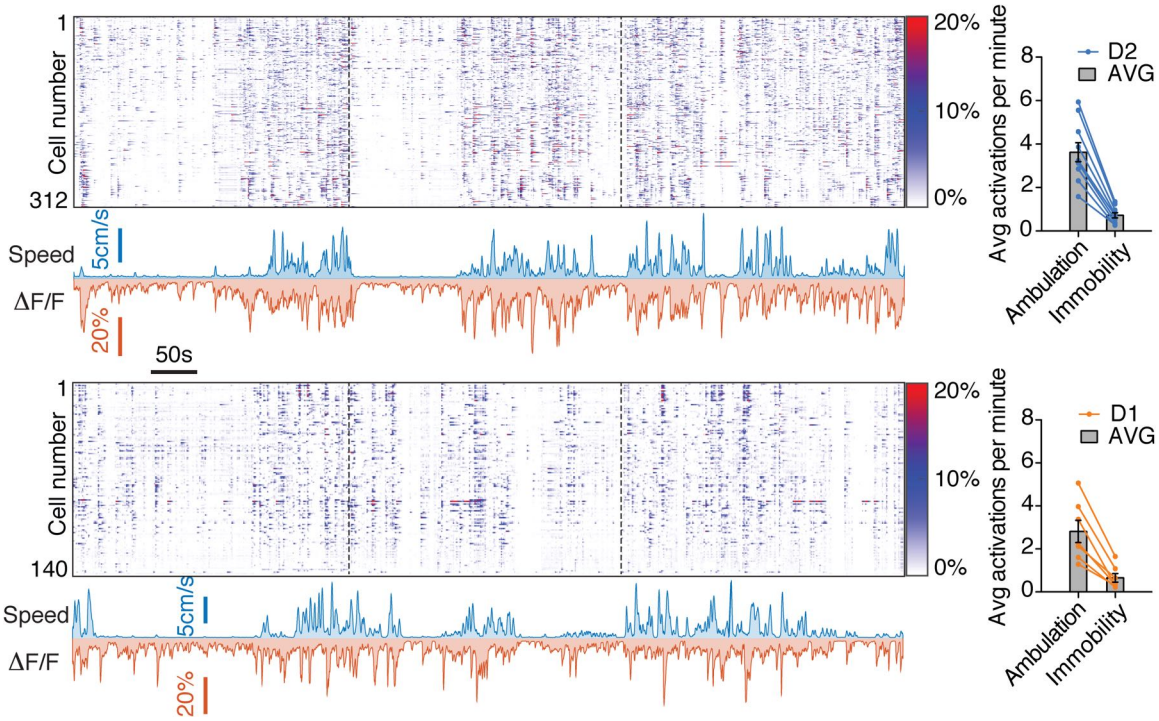

Figure 4.6. Neural activity rasterplot and speed profile for a D2 (top) and a D1 (bottom) mouse: they both show strong positive correlation between average neural activity and speed. Additionally, all mice showed a significant direct and indirect pathway inhibition during immobility compared with ambulation. The bar plot on the right represents the average number of calcium transients per neuron per minute (defined with a threshold of 5% $\Delta F/F$). Vertical dotted lines mark the separation between each 5 minute experiment.

With our findings we demonstrate how the relation between D1 and D2 neural activity and locomotor activity is much more complex to be explained as two neural circuits exerting opposite effects on behavior. We evaluated the average neural activity in 17 mice based on their average calcium trace as a function of their speed (Fig. 4.7), and the results confirm an average positive correlation. In average, D2 neurons surprisingly showed consistently higher neural activity than D1, particularly at higher speeds (> 2 cm/s). When considering individual cell populations, however, it emerges a much more complex relation between neural activity and speed (Fig.

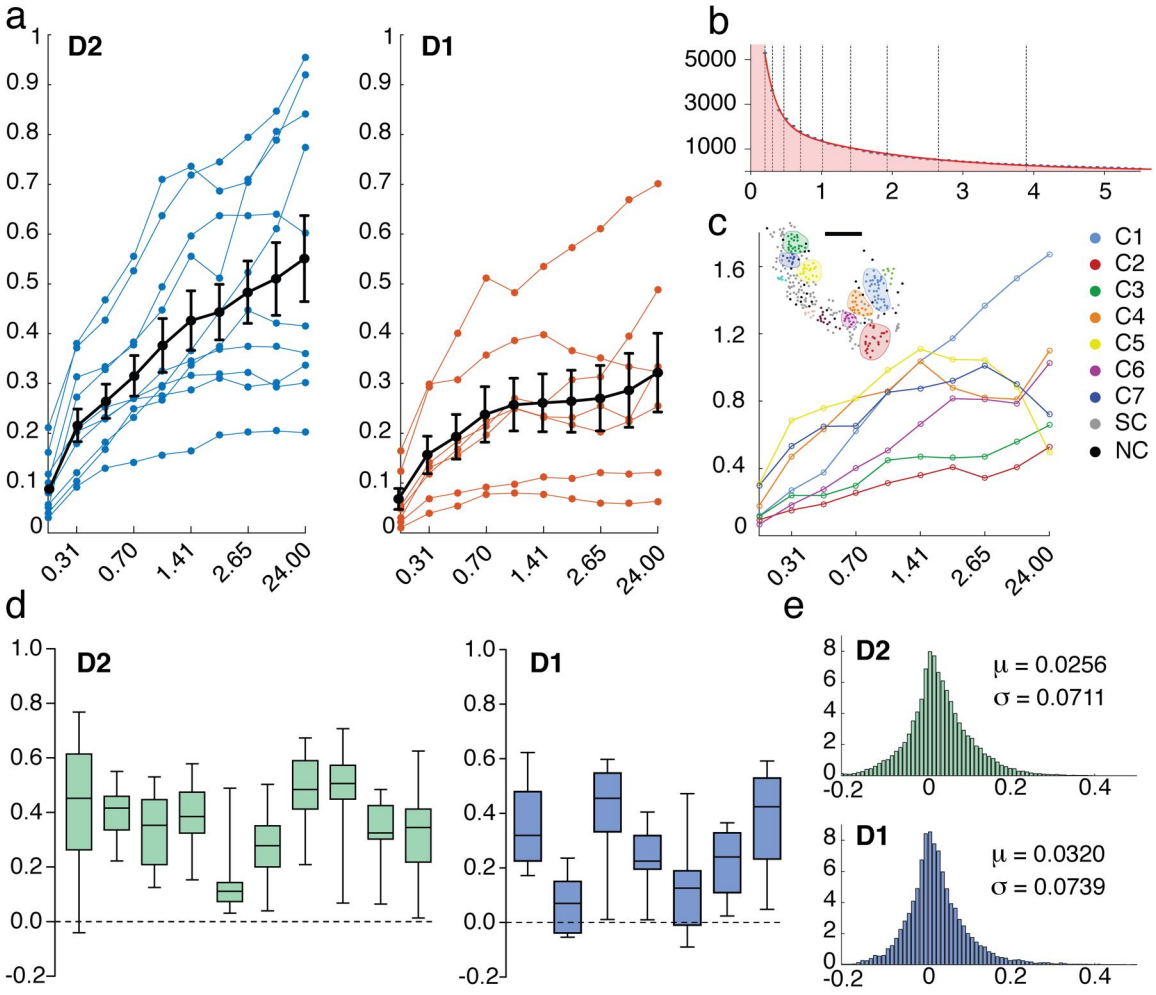

Figure 4.7. Both D1 (**a**) and D2 (**b**) average neural activity shows a positive correlation with speed: the average speed of 17 mice was partitioned into 10 equally spaced bins (4500s each), according to the average speed profile shown in **b**. A closer analysis of a single mouse cell clusters (**c**), however, suggests that the activity pattern is very diverse in different cell groups, consistently with the results presented in Section 4.1.4 (scale bar 200 μm). A positive Pearson's correlation coefficient relates the average calcium activity with the speed (**d**) in both the direct and indirect pathways, with a slightly higher correlation at a single cell level in D2 neurons (**e**). In **d** boxes extend from 25th to 75th percentile, whiskers from minimum to maximum value.

4.7c), in which neuron subpopulations show heterogeneous activity increase rate and some of them (C5 and C7) have a negative trend at higher speeds.

Detailed analysis of D1- and D2- MSN activity around motion initiation (MI), motion termination (MT), and velocity Peak (PK) demonstrated that D1- and D2- MSN displayed similar population activity in relation to MI, MT, and PK (Fig. 4.8). Moreover, the time-averaged GCaMP6 fluorescent signal change, which represents the integrated calcium activity, displayed positive correlations with locomotion speed of the mice for both D1- and D2- MSN (Fig. 4.7a). Together, these results suggest that D1- and D2- MSN activity during locomotion is similar rather than opposite as predicted by the rate-based dual circuit model. Our findings offer clear evidence in refuting the concept in the rate-based dual circuit model that increased mean firing rates of neurons in the striatal indirect pathway suppresses locomotion. Instead, these results could be explained by the alternative model that indirect pathway neurons inhibit unwanted behavior, and that concerted activities of direct and indirect pathway neurons coordinate locomotion.

These findings demonstrate the need for an in depth, single cell resolution analysis of the direct and indirect pathway activity; merging together the neural activity of large neural populations in the striatum, or focusing on a small cell subpopulations, cannot fully explain the wide variety of functional aspects and complex interactions underlying these neural circuits. To this aim we introduce, in parallel with single cell analysis, the study of neural activity of clusters of neurons to provide a way of mining the essential information from large amount of data.

4.1.4 Cell Clustering

For a more compact representation of neural data, the clustering algorithm presented in Section 3.2 was applied to the recorded calcium traces. A cell clustering example for a D2 mouse is shown in Fig. 4.9 (the results of the clustering algorithm for all the mice considered in this work is shown in Appendix A).

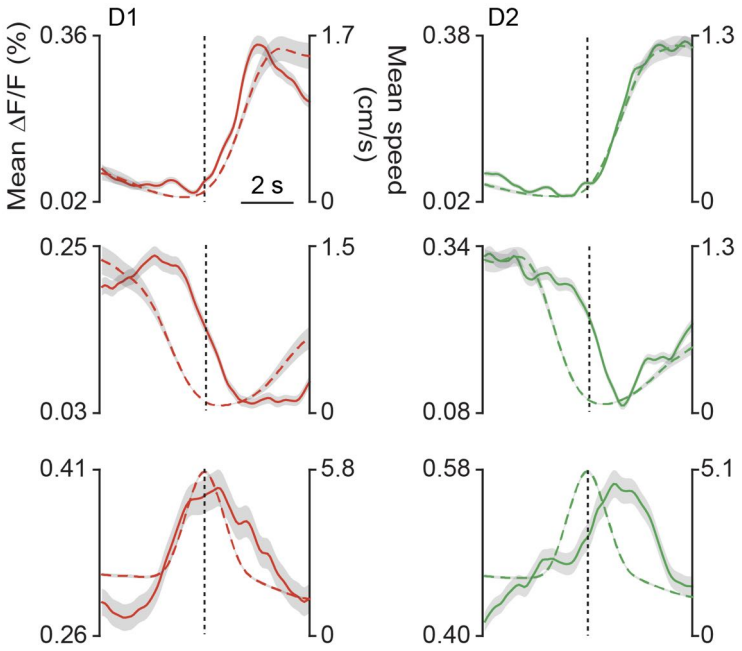

Figure 4.8. D1- and D2- MSN displayed similar population activity around motion initiation (MI), motion termination (MT), and velocity peak (PK). Red traces indicate integrated fluorescent change of all the neurons from all the D1-Cre (Left panels) and D2-Cre (Right panels) mice over time; Blue traces indicate locomotion speed of mice. Vertical dotted lines indicate mouse motion initiation (top panels), motion termination (middle panels), and velocity peak (bottom panels). Horizontal scale bar: 2 seconds.

Since the Pearson's correlation was used as a criterion to determine the closest cluster centroid in the k-means clustering algorithm, it should not be surprising that cells belonging to the same cluster show similar calcium traces (Fig. 4.11a). Furthermore, even though the average intra cluster correlation is predominant, inter cluster similarities are often observed (Fig. 4.11c and B.1), indicating and that such a neuron partitioning does not imply a categorical separation (functional or anatomical) between neuron populations, but more so it is meant to provide an aid to reduce the data dimensionality and help recognizing neural activity patterns.

In the rate-based dual circuit model, the mean firing rates of neurons is thought to encode information in the direct or indirect pathways. However, calcium activities of

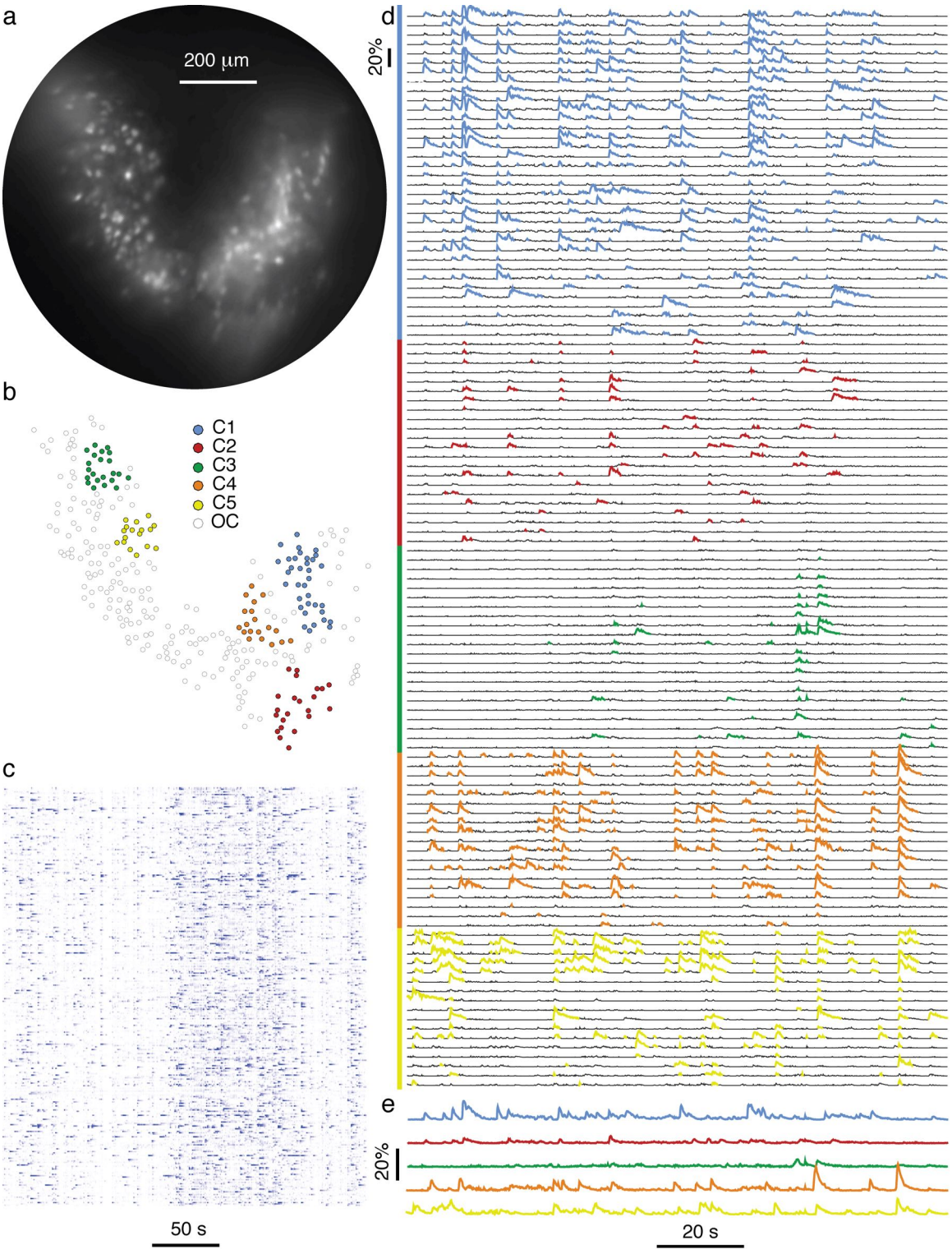

Figure 4.9. Clustering example: **a**, the pixel standard deviation reveals the location of the most active cells. **b**, spatial map of all the active cells over 5 days: colored cells belong to the largest 5 clusters, and an example of their calcium traces and centroids is shown in **d** and **d**, respectively. **c**, the unsorted rasterplot for all detected cells.

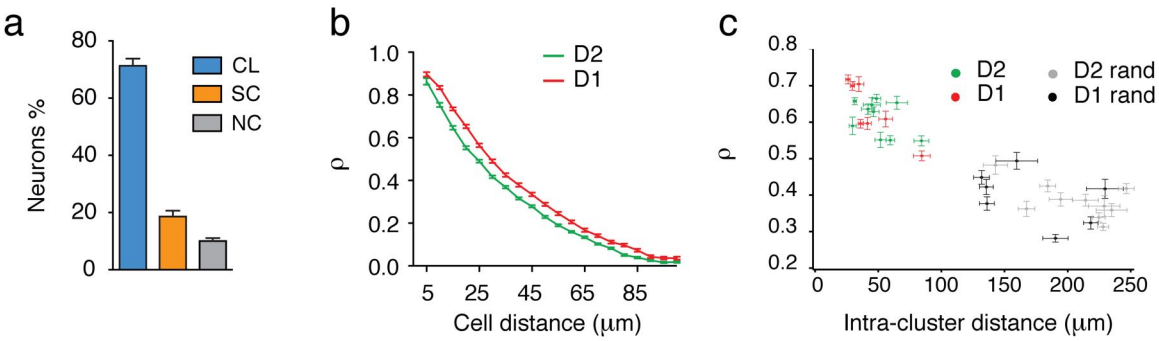

Figure 4.10. Overall clustering evaluation. **a**, average number of cells labeled as clustered (CL), belonging to clusters with less than 3 cells (SC), or unclustered (NC). **b**, the average pairwise correlation coefficient is a decreasing function of the distance between cells, which explains the spatial compactness of the clusters: in **c** the average intracluster correlation versus average cell to centroid spatial distance shows both functional and spatial compactness when compared to the average values of 100 Monte Carlo simulations based on shuffled neural traces and cell index.

individual neurons in either direct or indirect pathway displayed a great deal of heterogeneity (Fig. 4.11), which suggests the existence of subpopulation of MSN within direct or indirect pathway that modulate different behavior output. After clustering, neurons within each cluster displayed similar activities (Fig. 4.11a), whereas differences in activity patterns among clusters are prominent (Fig. 4.11d). Heterogeneity of cluster activity were also apparent in cross-correlation between cluster activity and locomotor activity of the mouse (Fig. 4.11e), as C1, C2, C3, C4 and C7 all demonstrated different cross-correlation coefficient and time lag with locomotor speed of the mouse (Fig. 4.11f). Taking advantage of the single neuron resolution of our imaging method, we anatomically mapped each neuronal cluster to examine their spatial distributions. Interestingly, we found that neurons within each functional cluster were also spatially clustered, suggesting that neurons with similar activity patterns are also spatially close (Fig. 4.11b).

To determine functional implication of neuron clusters in dorsal striatum, we next examine activity of individual clusters around mouse locomotion speed. Of the 11 clusters identified in Fig. 4.11b, activity of cluster C1 closely followed locomotion

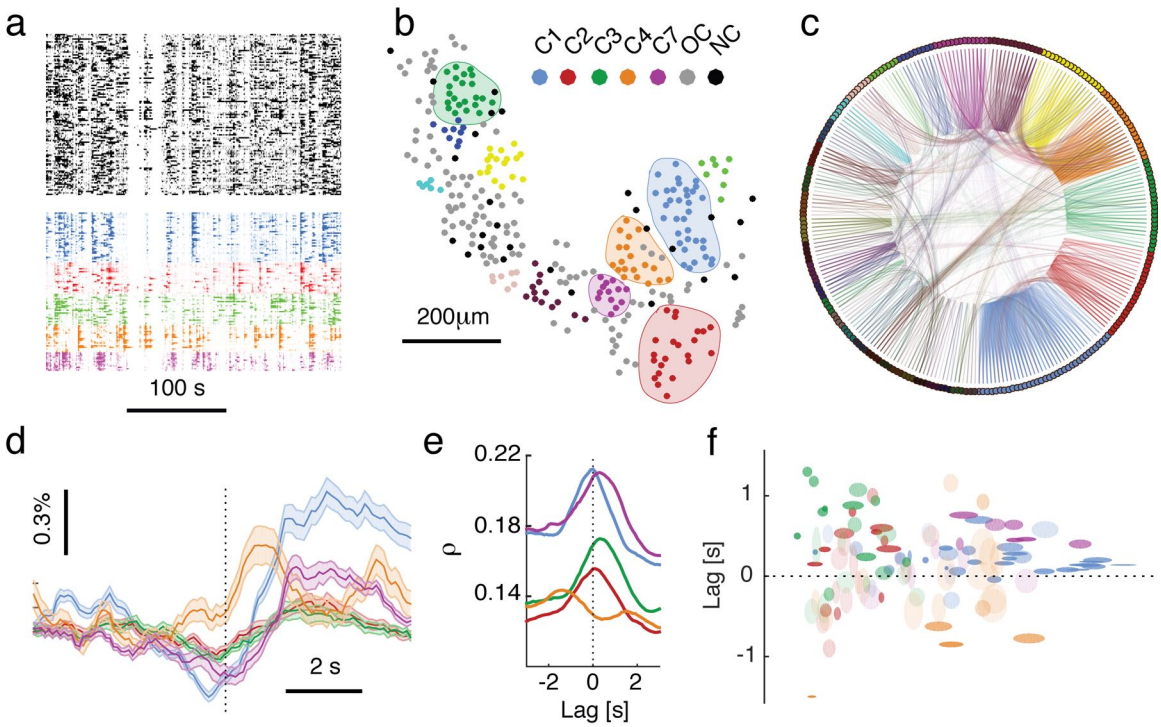

Figure 4.11. Cell clustering results on a D2 mouse. **a**, calcium traces before (top) and after (bottom) clustering, color coded according to the clustering scheme shown in **b**. **c**, pairwise correlation between cells, highlighting a stronger intracluster than intercluster correlation. The heterogeneity of the neural activity of the 5 clusters circled in **b** is shown through the 5 day average of the cluster centroids during motion initiation (**d**), the 5 day average cross correlation between cluster centroids and velocity (**e**), and the 5 day average of the cross correlation peak value versus lag for the single neurons within each cluster (length and width of the ellipse reflect the standard deviation of the peak value and lag, respectively).

speed of the mouse (Fig. 4.12a), which was also apparent in the cross correlation function between the peaks of C1 activity and mouse locomotion speed (Fig. 4.12b, left panel). Conversely, activity of cluster C4 did not closely followed mouse locomotion speed (Fig. 4.12a and b). Of all the D1- and D-2 MSN clusters examined, approximately 50% of clusters demonstrated cross correlation with mouse locomotion speed, with cross correlation coefficient ranging between 0.6 and 0.8, and time lag between the cluster activity and mouse locomotion speed ranging between -1.0 and

1.0 second (Fig. 4.12c and d). These results suggest that activity of MSN clusters encode specific behavior state of the mouse.

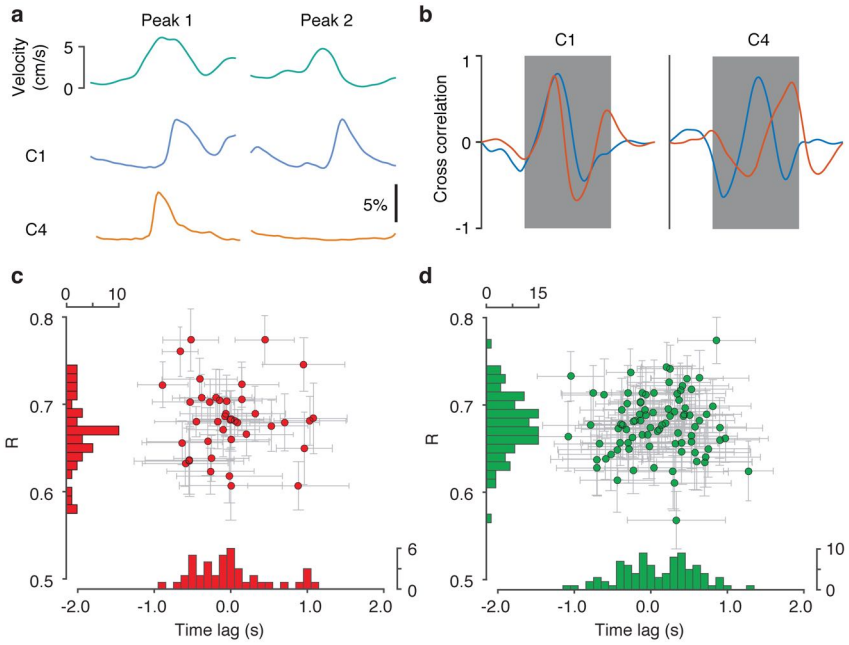

Figure 4.12. **a**, representative cluster activity around mouse locomotion speed peak. Upper panel: two representative speed peaks; Middle: activity of cluster C1 as shown in Fig. 4.11b around the two locomotion speed peaks, demonstrating that cluster C1 activity closely followed locomotion speed peak with a slight time lag; Lower panel: activity of cluster C4 as shown in Fig. 4.11b around the two locomotion speed peaks, demonstrating that cluster C4 activity did not follow locomotion speed peak. **b**. Cross correlation between cluster C1 and C4 activity with mouse locomotion speed. Left panel: cluster C1 activity consistently showed cross correlation with mouse locomotion speed; Right panel: cluster C4 activity did not show consistent cross correlation with mouse locomotion speed. X-axis represents time lag between locomotion speed and cluster activity, Y-axis represents cross correlation coefficient. **c**, Scatter plot of time lag and cross correlation coefficient between all D1-MSN clusters showed consistent cross correlation with mouse locomotion speed. X-axis represents time lag between locomotion speed and cluster activity, Y-axis represents cross correlation coefficient. Histogram plots on X- and Y- axis represent distribution of time lag and cross correlation coefficient, respectively. **d**, Scatter plot of time lag and cross correlation coefficient between all D2-MSN clusters showed consistent cross correlation with mouse locomotion speed. X-axis represents time lag between locomotion speed and cluster activity, Y-axis represents cross correlation coefficient. Histogram plots on X- and Y- axis represent distribution of time lag and cross correlation coefficient, respectively.

4.2 Effect of Cocaine in the Dorsal Striatum

We then recorded both locomotor activity and GCaMP6 fluorescent signals from D1- or D2-Cre mice before and after cocaine injection, as a pharmacological mean to increase locomotor activity (Fig. 4.13).

Based on the observed positive correlation of D1- and D2- MSN activity with mouse locomotor activity, one would expect that under increased locomotor activity conditions, D1- and D2- MSN activity would increase as well.

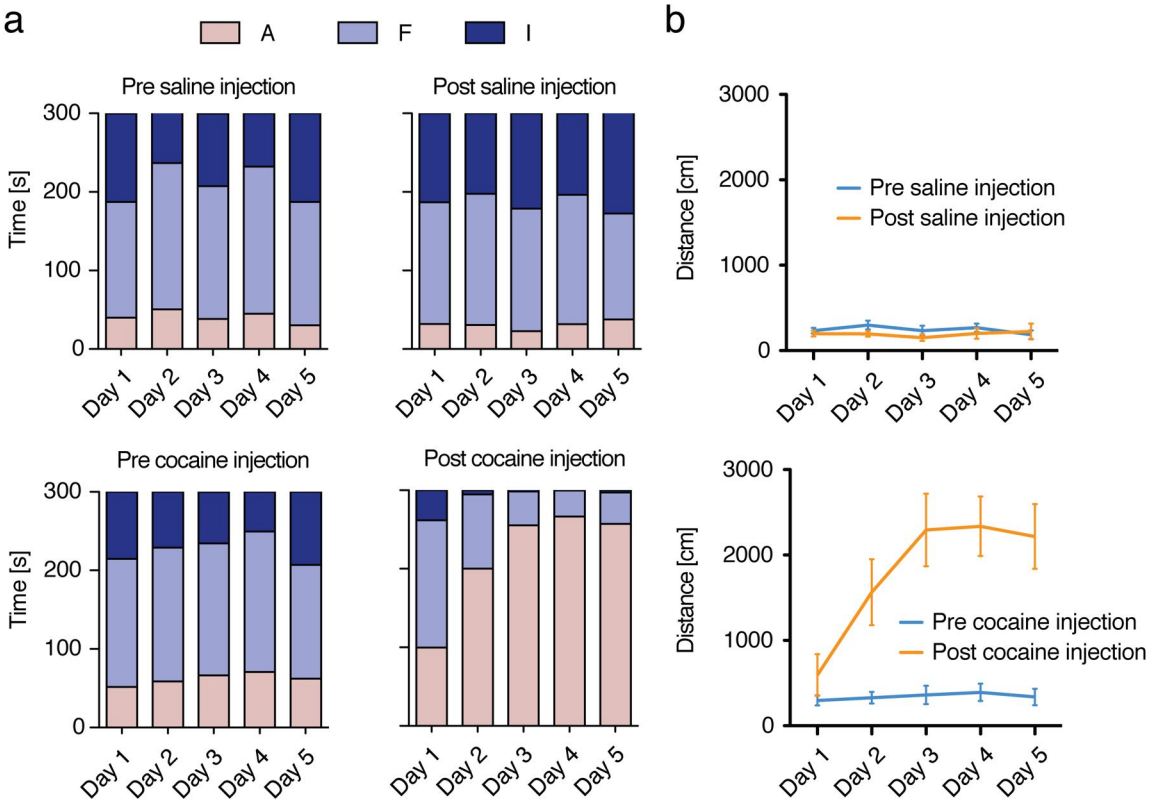

Figure 4.13. Effect of cocaine sensitization on behavior. **a**, after cocaine injection the ratio of average time spent in a 5 minute experiment during ambulation (A, speed greater than 2 cm/s) progressively increases compared to the time spent in fine motion (F, speed between 0.2 cm/s and 2 cm/s) or immobility (I, speed smaller than 0.2 cm/s). Similarly, the total distance travelled increases daily reaching a plateau on day 3.

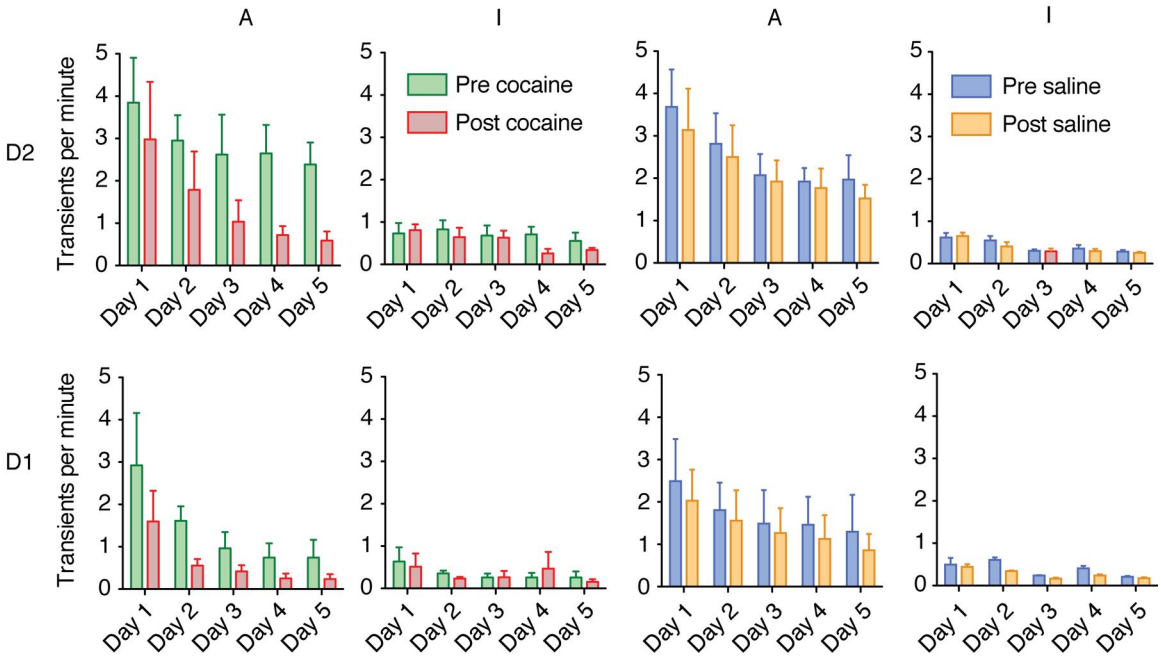

Figure 4.14. Neural activity in D1 (bottom row) and D2 (top row) mice expressed as average calcium transients per cell per minute for every day during ambulation (A) and immobility (I). Cocaine has a strong inhibitory effect in both striatal pathways, causing a more pronounced reduction in activity among D2 neurons.

To our surprises, cocaine injection suppressed overall population activity for both D1- and D2- MSN during ambulation, but did not affect D1- or D2- MSN activity during immobility (Fig. 4.14 and Fig. 4.15).

The fact that cocaine enhanced mouse locomotor activity yet depressed both D1- and D2- MSN activity offers further evidence in refuting the rate-based dual circuit model that mean firing rate of direct pathway neurons facilitates locomotion whereas that of indirect pathway suppresses locomotion. It also suggests that mean firing rate of direct or indirect pathway neurons does not serve the purpose of information encoding as suggested by previous models. Instead, it is likely that specific subpopulation of neurons in the direct or indirect pathways such as neuron clusters, serve the purpose of information encoding. Therefore, we propose to revise the alternative model to incorporate the neuron cluster concept.

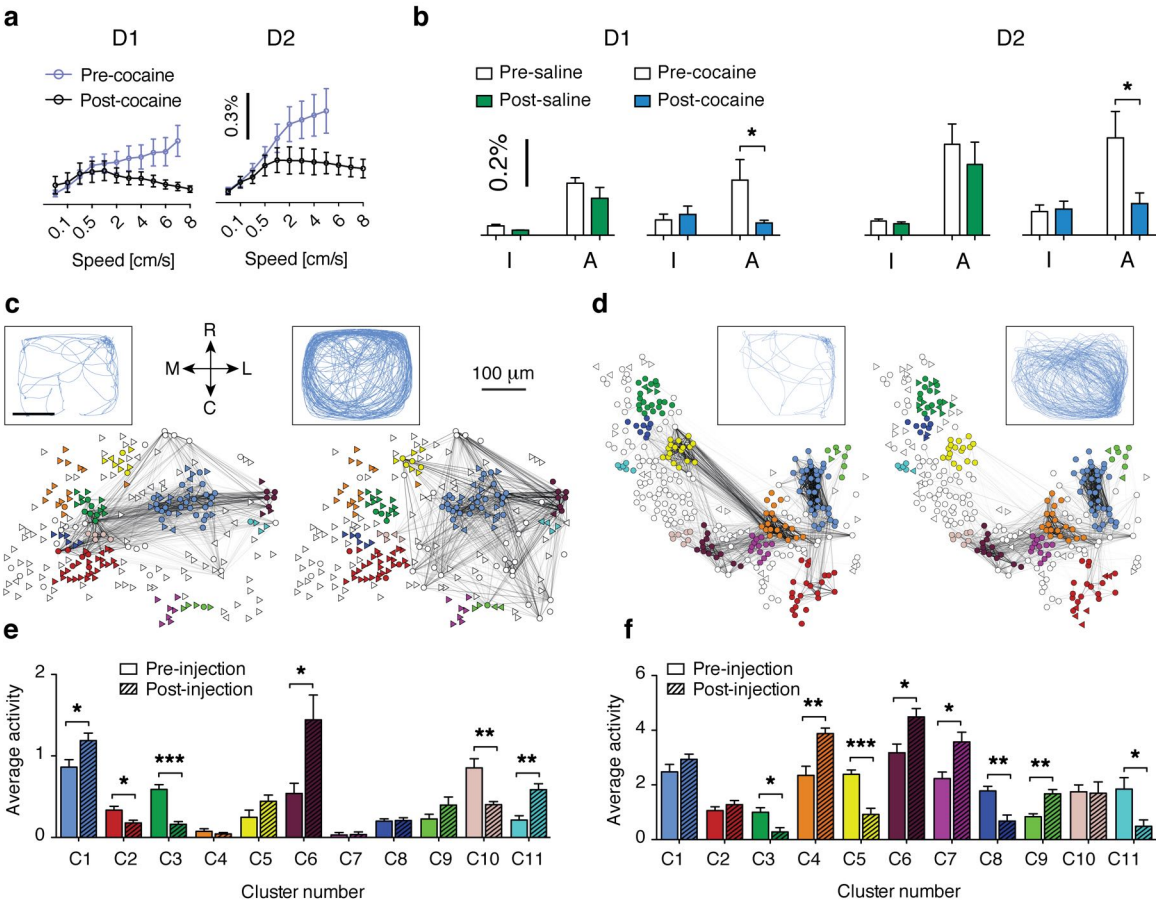

Figure 4.15. Acute cocaine effect in dorsal striatum. **a**, synchronous activity within certain clusters is disrupted after cocaine injection; the inset shows the trajectory of the mouse during the third day, before (left) and after (right) cocaine injection. **b**, asynchronous correlation coefficient for the cells belonging to the 6 largest clusters. **c**, average activity change after cocaine injection for the 11 cluster highlighted in **a**. **d**, average D2 cluster centroid activity change.

Interestingly, before cocaine injection, both D1- and D2- MSN displayed synchronous calcium activity (Fig. 4.15, left panels). Cocaine injection impacted this synchronous activity heterogeneously: decreased, enhanced, as well as unchanged synchronous activities were observed both for D1- and D2- MSN clusters (Fig. 4.15, right panels). Cocaine also influenced individual cluster activity heterogeneously: decreased, enhanced, as well as unchanged cluster activities were observed both for D1- and D2- MSN (Fig. 4.15e and f). In all the D1- and D2- MSN clusters analyzed, a

large number of clusters displayed diminished activity following cocaine injection in both D1- and D2- MSN (Fig. 4.16a and b, and Fig. 4.17).

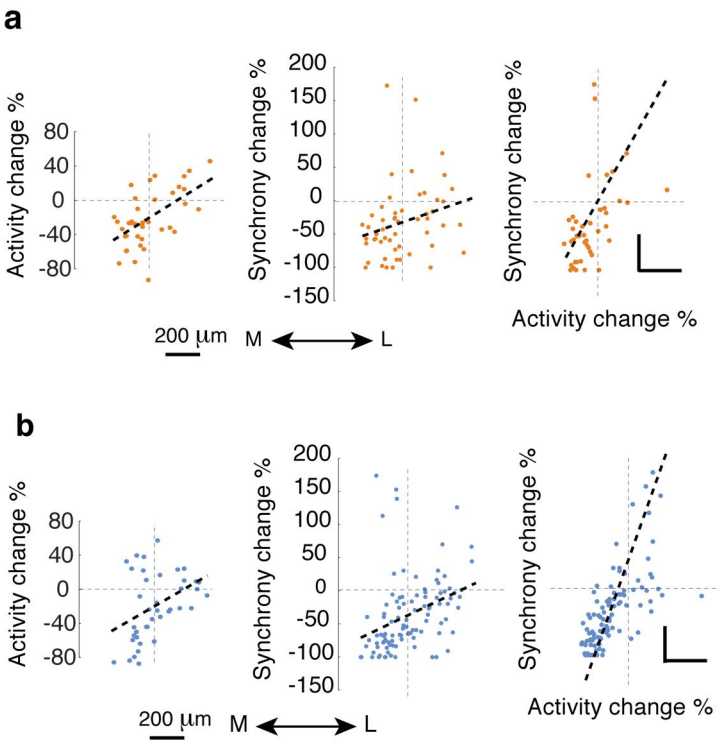

Figure 4.16. **a**, cocaine injection altered both cluster activity and synchronous calcium activity heterogeneously for D1-MSN. Left panel: cluster activity change following cocaine injection; Middle panel: cluster synchronous calcium activity change following cocaine injection; Right panel: scatter plot of cluster activity change vs. synchronous calcium activity change. X-axis represents cluster activity change, Y-axis represents synchronous calcium activity change. A positive correlation between synchronous calcium activity change and cluster activity change is observed. **b**, cocaine injection altered both cluster activity and synchronous calcium activity heterogeneously for D2-MSN. Left panel: cluster activity change following cocaine injection; Middle panel: cluster synchronous calcium activity change following cocaine injection; Right panel: scatter plot of cluster activity change vs. synchronous calcium activity change. X-axis represents cluster activity change, Y-axis represents synchronous calcium activity change. A positive correlation between synchronous calcium activity change and cluster activity change is observed.

Some clusters did demonstrate enhanced activity following cocaine injection both in D1- and D2- MSN. It is possible that the clusters with selectively enhanced activity

following cocaine injection may play more prominent role in controlling locomotion. Interestingly, when we examine cluster activity along medial-lateral axis of dorsal striatum, we found that cluster activity changes following cocaine injection showed a gradient along medial-lateral axis of dorsal striatum both for D1- and D2- MSN: more clusters with prominent diminished activity were observed near dorsal medial striatum, and more clusters with enhanced activity were observed near dorsal lateral striatum (Fig. 4.16a and b). Cluster synchronous calcium activity also displayed a similar gradient along medial-lateral axis of dorsal striatum both for D1- and D2- MSN: more clusters with prominent diminished synchronous calcium activity were observed near dorsal medial striatum, and more clusters with enhanced synchronous calcium activity were observed near dorsal lateral striatum (Fig. 4.16a and b). The synchronous calcium activity change and cluster activity change was positively correlated, suggesting that enhanced cluster activity may lead to more synchronous calcium activity. Given that the dorsal medial striatum participates in goal-directed behavior whereas the dorsal lateral striatum is important in habit formation, this unique D1- and D2- MSN activity change by cocaine may indicate the initiation of transition from goal directed behavior to habitual behavior in addiction.

It is worth noting that the striatal input to globus pallidus (GP) is highly convergent. In rodents, it is estimated that the number of MSN in the striatum is approximately 60 fold of that of GP neurons, and that GP neurons on average receive input from approximately 60 MSN. In light of our findings of functionally heterogeneous and spatially compact neuron clusters in the direct and indirect pathway, it is possible that individual GP neurons receive inputs from neurons in only one or a few functional clusters, and that mean firing rates and patterns of each cluster relay striatal encoded information to GP neurons. Although the biological significance of the synchronous activity in D1- and D2- MSN remains to be further explored, it is possible that synchronous activity may be more efficient in relaying information from dorsal striatum MSN clusters to GP target neurons.

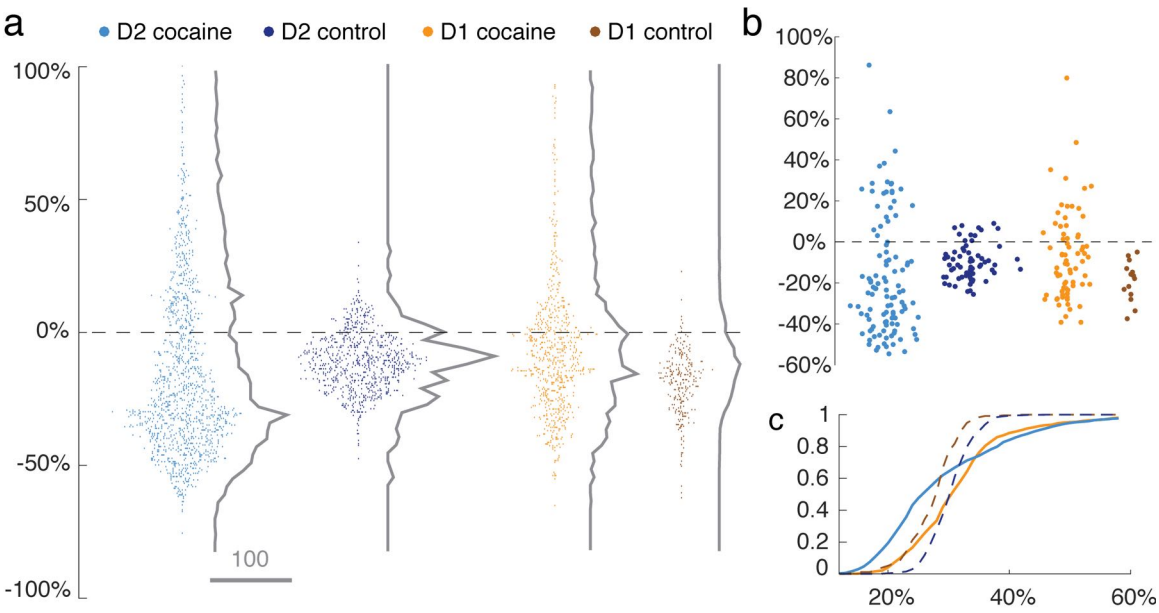

Figure 4.17. Scatterplot of single neuron activity change (5 day average) for 4 different cell groups: D2 cocaine group (1314 cells, 5 mice), D2 control group (815 cells, 5 mice), D1 cocaine group (734 cells, 5 mice) and D1 control group (255 cells, 2 mice). **b** shows the cluster activity change for the same groups is shown, calculated as the average cell activity change within each cluster. The cumulative distribution function of the activity change for these four groups (**c**) suggests that D2 neurons undergo an overall stronger inhibition as acute effect of cocaine injection.

4.3 Machine Learning for Decoding Behavioral Variables

We reasoned that if heterogeneous neuronal activities within D1- and D2- MSN clusters serve the purpose of information encoding, one should be able to predict mouse behavior state based on neuronal activity patterns. As a proof-of-concept experiment, we categorized mouse locomotor behavior into two simple and opposite behavior states: Ambulation (A) and Immobility (I). We trained a machine-learning algorithm using part of our behavior and calcium activity data set. Following training of the machine-learning algorithm, we test the performance of the algorithm using the rest of our data set not used in the initial training (Fig. 4a). The algorithm was able to reliably predict mouse behavior state based on striatal neuron activity data (Fig. 4a and b). Specific neuronal activity patterns that predict specific behavior

state could also be mapped (Fig. 4c). It is noteworthy that the neuronal activity pattern for Ambulation prediction (Fig. 4c, left panel) and that for Immobility prediction (Fig. 4c, middle panel) is largely none-overlapping, and belongs to different functional clusters (Fig. 4c, right panel). Both D1- and D2- MSN activity could be used for behavior prediction, but the accuracy of prediction was higher when the prediction was based on D2-MSN activity (Fig. 4d). The success in using neuronal activity pattern to predict mouse behavior state strongly supports our hypothesis that heterogeneous striatal D1- and D2-MSN cluster activity serves the purpose of information encoding for the behavior state of mouse.

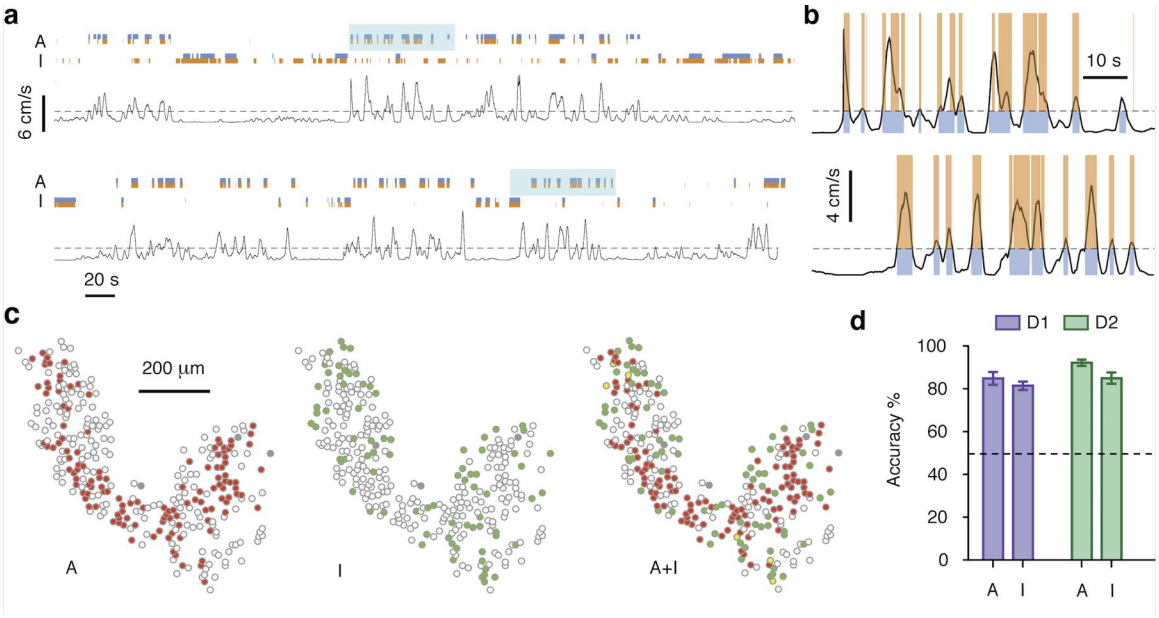

Figure 4.18. **a**, mouse locomotion is categorized into Ambulation (A) and Immobility (I). Blue segments indicate actual behavioral state, red segments indicate the predicted state; speed profiles are shown at the bottom for both D1 (top panel) and D2 (bottom panel) mice. **b**, Zoom-in of green boxed region in **a**. **c**, Weights of neurons that are used for behavior prediction of ambulation (left panel), immobility (center panel) and overlay of the two (right panel). **d**, Prediction accuracy for D1 (blue bars) and D2 (green bars) mice.

4.4 Conclusion

In summary, by developing a custom miniature fluorescence imaging system and employing it to record neuronal activity in dorsal striatum via GRIN lens, we provided strong evidence refuting the long-standing rate-based dual circuit model of basal ganglia. Based on our findings, we propose that dorsal striatal MSN clusters serves the purpose of information encoding, and that coordinated activities between direct and indirect pathway neuron clusters ensure proper behavior output. Our in vivo imaging technique, neuron cluster analysis, and machine-learning algorithm could be applied to many other brain regions and animal behavior models, and will have transformative impact on unraveling how neuronal circuit activity controls behavior.

5. CONTRIBUTION

Miniature fluorescence optical imaging is changing the way neuroscientists can analyze brain activity at a microscopic neural circuit level and link anatomical structure with functional characteristics with unprecedented single cell detail. More importantly, the miniaturization of fluoresce imaging systems opens the possibility to record the activity of intact neural circuits in freely behaving animals, allowing to study in depth the relevance of specific neural circuits to certain behaviors. However the unique potential offered by these tools comes with several challenges which need to be met through a joint multidisciplinary effort across the realms of Biology and Engineering.

The contribution of this work is threefold: the design and manufacturing of a miniature fluorescence imaging system for use with both VSDI and calcium imaging, the introduction of data processing techniques for analyzing the specific type of data generated by functional optical neural recordings, and the application and validation of these tools in providing new insights in the study of a biologically relevant problem, the functional organization and behavioral encoding of D1 and D2 neurons in the dorsal striatum.

5.1 System Design

In this work we propose the first full miniature fluorescence imaging system for application with both voltage sensitive dye imaging (VSDI) and calcium imaging (CI). This allows to perform novel in vivo studies on freely behaving mice while imaging virtually any area in the brain with VSDI or CI at single neuron resolution. The developed system relies on the integration of a custom designed miniature microscope

(Tab. 5.1), an FPGA based custom hardware for both tethered and wireless data transmission, and a cross platform software interface for real time data streaming and behavioral recording.

Table 5.1. Summary of the features of the proposed microscope compared with current state of the art miniature fluorescence imaging systems.

System	Single cell	SNR	Power	Use in mice	VSDI	Untethered
[27]	✗	N/A	2.4 mW	✗	✗	✓
[26]	✓	47 dB	N/A	✓	✗	✗
[38]	✗	61 dB	12 mW	✗	✓	✗
This work	✓	48 dB	320 mW	✓	✓	✓

5.2 Data Processing Tools

An important issue in the interpretation of the single cell neural activity is how to mine relevant information from the large amount of recorded data, and how to correctly extract single neuron activity from the recorded *in vivo* images. We first introduced efficient image preprocessing algorithms targeted to real-time implementation, including image registration, automatic cell detection and calcium traces extraction.

Typical image registration techniques fail to robustly detect image translations due to the unique nature of the recorded brain images, which in general have no distinctive landmarks and can substantially diverge across different frames depending on which cell is active at any given time instant. The proposed algorithm based on the Phase Correlation method offers sub-pixel precision for iterative registration of sequential frames, and it was tested on both synthetic datasets and real neural images affected by motion artifacts typical of *in vivo* applications.

Additionally, we proposed a fast, noise robust cell identification algorithm based on the shape matching of the image gradient which can target specific cell sizes and is robust to the contribution of out of plane fluorescence. This allowed to create stable cell masks for chronically tracking singe neurons for several weeks.

Another data analysis technique introduced is a clustering method which allows to partition neurons into different groups of cell with similar activity, and the application of which brought unprecedented insight on the functional organization of the neural circuit on the dorsal striatum. The proposed algorithm is based on the meta k-means [58, 59], and it improves the consistency of the partitioning scheme within different datasets and the applicability of the algorithm to generic datasets (Fig. 5.1).

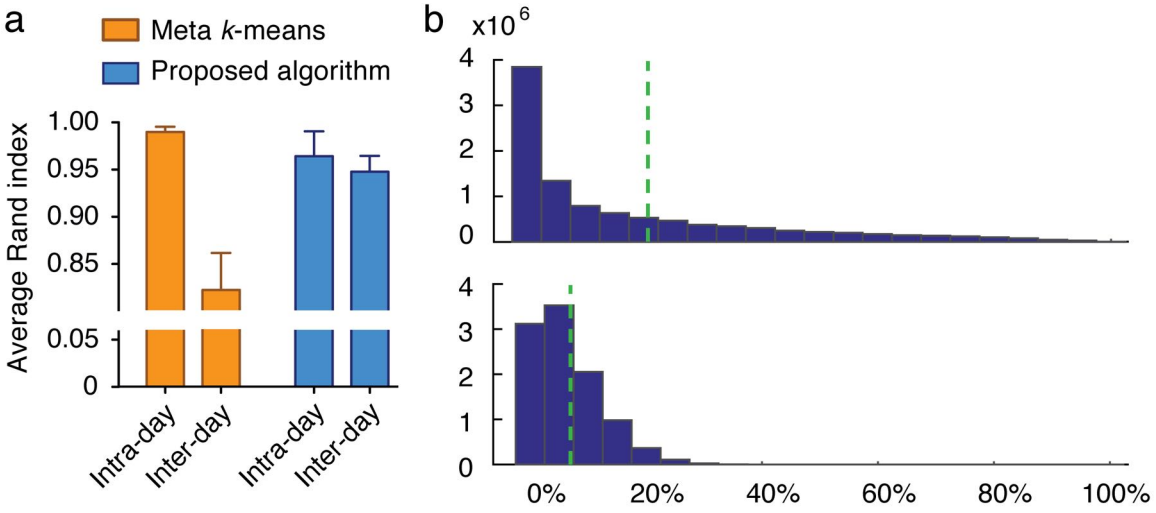

Figure 5.1. Comparison between meta k-means and proposed algorithm. **a**, the average Rand index of the final clustering scheme shows a significant decrease in the inter-dataset variability (across 5 different days) while still maintaining good intra-dataset consistency. **b**, histogram showing the distribution of the average inter-dataset absolute difference in the co-occurence matrix elements for the meta k-means (*top*) and the proposed algorithm (*bottom*): the long tail, which indicates significant differences in the individual partitioning schemes, is considerably reduced. 5 datasets were considered for 5 different days, and the average absolute variance − dotted green line − was 20.48% for the meta k-means and 7.31% for the proposed clustering algorithm.

5.3 Novel *In Vivo* Study on Dorsal Striatum

The application of the developed techniques to the study of the striatal activity in freely moving mice both validated the relevance of the proposed system and data

analysis tools in addressing key questions in Neuroscience, and provided a new perspective on the functioning principles of two important neural circuits in the basal ganglia, the direct and indirect pathways, which can be summarized as follows.

- We investigated the complex relation between the neural activity in the direct and indirect pathways and locomotor activity, providing strong evidence for refuting the classical rate-based model and proposing a new
- The application of the clustering method proposed in this work suggests a functional organization of the dorsal striatum where neurons are clustered into spatially compact sub-populations with very diverse functional traits.
- These identified neuron clusters show very heterogeneous neural activity and correlation with locomotion, indicating encoding of different behaviors.
- The acute effect of cocaine is in general inhibitory for both D1 and D2 neurons, however at a single cluster level the neural response is very diverse, showing a clear positive gradient in the medial-lateral direction.
- Behavioral activity can be precisely predicted by single cell neural activity through the use of neural networks, suggesting the encoding of locomotion and other behaviors from specific groups of cells in the striatum.

LIST OF REFERENCES

LIST OF REFERENCES

[1] K. Deisseroth and M. J. Schnitzer. Engineering approaches to illuminating brain structure and dynamics. *Neuron*, 80:568–577, 2013.

[2] M. R. Warden, J. A. Cardin, and K. Deisseroth. Optical neural interfaces. *Annu. Rev. Biomed. Eng.*, 16:103–129, 2014.

[3] K. Deisseroth. Optogenetics. *Nat. Methods*, 8(1):26–29, 2011.

[4] L. L. Looger and O. Griesbeck. Genetically encoded neural activity indicators. *Curr. Opin. Neurobiol.*, 22:18–23, 2012.

[5] T. Knöpfel. Genetically encoded optical inicators for the analysis of neruonal circuits. *Nat. Rev. Neurosci.*, 13(10):687–700, 2012.

[6] X. Han, X. Qian, J. G. Bemstein, H. Zhou, G. T. Franzesi, P. Stern, R. T. Bronson, A. M. Graybiel, R. Desimone, and E. S. Boyden. Millisecond-timescale optical control of neural dynamics in the nonhuman primate brain. *Neuron*, 62(2):191–198, 2009.

[7] L. Fenno, O. Yizhar, and K. Deisseroth. The development and application of optogenetics. *Annu. Rev. Neurosci.*, 34:389–412, 2011.

[8] L. B. Cohen, B. M. Salzberg, H. V. Davila, W. N. Ross, D. Landowne, A. S. Waggoner, and C. H. Wang. Changes in axon fluorescence during activity: molecular probes of membrane potential. *J. Membrane Biol.*, 19:1–36, 1974.

[9] L. Cohen. Optical approaches to neuron function. *Annu. Rev. Physiol.*, 51:487–490, 1989.

[10] D. S. Peterka, H. Takahashi, and R. Yuste. Imaging voltage in neurons. *Neuron*, 69:9–21, 2011.

[11] R. K. Gupta, B. M. Salzberg, A. Grinvald, L. B. Cohen, K. Kamino, S. Lesher, M. B. Boyle, A. S. Waggoner, and C. H. Wang. Improvements in optical methods for measuring rapid changes in membrane potential. *J. Membrane Biol.*, 58:123–137, 1981.

[12] S. Chemla and F. Chavane. Voltage-sensitive dye imaging: Technique review and models. *J. Physiol.*, 104:40–50, 2010.

[13] B. J. Baker, E. K. Kosmidis, D. Vucinic, C. X. Falk, L. B. Cohen, M. Djurisic, and D. Zecevic. Imaging brain activity with voltage- and calcium-sensitive dyes. *Cell. Mol. Neurobiol.*, 25(2):245–282, 2005.

[14] M. Olivotto, A. Arcangeli, M. Carlà, and E. Wanke. Electric fields at the plasma membrane level: A neglected element in the mechanisms of cell signalling. *Bioessays*, 18:495–504, 1996.

[15] S. Preuss and W. Stein. Comparison of two voltage-sensitive dyes and their suitability for long-term imaging of neuronal activity. *PLOS ONE*, 8(10):1–13, 2013.

[16] R. Y. Tsien. New calcium indicators and buffers with high selectivity against magnesium and protons: design, synthesis, and properties of prototype structures. *Biochemistry*, 19:2396–2404, 1980.

[17] G. Grynkiewicz, M. Poenie, and R. Y. Tsien. A new generation of Ca^{2+} indicators with greatly improved fluorescence properties. *J. Biol. Chem.*, 260(6):3440–3450, 1985.

[18] C. Grienberger and A. Konnerth. Imaging calcium in neurons. *Neuron*, 73:862–885, 2012.

[19] A. Miyawaki, J. Llopis, R. Heim, J. M. McCaffery, J. A. Adams, M. Ikura, and R. Y. Tsien. Fluorescent indicators for Ca^{2+} based on green fluorescent proteins and calmodulin. *Nature*, 388:882–887, 1997.

[20] E. Neher. Quantitative aspects of calcium fluorimetry. *Cold Spring Harb. Protoc.*, 2013.

[21] M. Minderer, W. Liu, L. T. Sumanovski, S. Kügler, F. Helmchen, and D. J. Margolis. Chronic imaging of cortical sensory map dynamics using a genetically encoded calcium indicator chronic imaging of cortical sensory map dynamics using a genetically encoded calcium indicator chronic imaging of cortical sensory map dynamics using a genetically encoded calcium indicator. *J. Physiol*, 590(1):99–107, 2012.

[22] H. Lutcke, D. J. Margolis, and F. Helmchen. Steady or changing? long-term monitoring of neuronal population activity. *Trends in Neurosciences*, 36(7):375–384, 2013.

[23] C. Stosiek, O. Garaschuk, K. Holthoff, and A. Konnerth. In vivo two-photon calcium imaging of neuronal networks. In *Proc. Natl. Acad. sci. USA*, volume 100(12), pages 7319–7324, 2003.

[24] Y. Ziv, L. D. Burns, E. D. Cocker, E. O. Hamel, K. K. Gosh, L. J. Kitch, A. El Gamal, and M. J. Schnitzer. Long-term dynamics of CA1 hippocampal place codes. *Nat. Neurosci.*, 16(3):264–268, 2013.

[25] R. P. Barretto, T. H. Ko, J. C. Jung, T. J. Wang, G. Capps, A. C. Walters, Y. Ziv, A. Attardo, L. Recht, and M. J. Schnitzer. Time-lapse imaging of disease progression in deep brain areas using fluorescence microendoscopy. *Nat. Med.*, 17(2):1–15, 2011.

[26] K. K. Ghosh, L. D. Burns, E. D. Cocker, A. Nimmerjahn, Y. Ziv, A. El Gamal, and M. J. Schnitzer. Miniaturized integration of a fluorescence microscope. *Nat. Methods*, 8(10):871–882, 2011.

[27] K. Murari, R. Etienne-Cummings, G. Cauwenberghs, and N. Thakor. An integrated imaging microscope for untethered cortical imaging in freely-moving animals. In *32nd Annual International Conference of the IEEE EMBS*, pages 5795–5798, 2010.

[28] W. Piyawattanametha, E. D. Cocker, L. D. Burns, R. P. Barretto, J. C. Jung, H. Ra, O. Solgaard, and M. J. Schnitzer. *In vivo* brain imaging using a portable 2.9g two-photon microscope based on a microelectromechanical systems scanning mirror. *Optics letters*, 34(15):2309–2311, 2009.

[29] A. J. Theuwissen. CMOS image sensors: State-of-the-art. *Solid-state electronics*, 52:1401–1406, 2008.

[30] E. R. Fossum. Active pixel sensors: are CCD's dinosaurs? In *Proc. of SPIE: Electronic imaging, charge-coupled devices and solid state optical sensors III*, volume 1900, pages 2–14, 1993.

[31] G. P. Weckler. Operation of p-n junction photodetectors in a photon flux integrating mode. *IEEE Journal of solid-state circuits*, SC-2(67):65–73, 1967.

[32] B. C. Burkey, W. C. Chang, J. Littlehale, T. H. Lee, T. J. Tredwell, J. P. Lavine, and E. A. Trabka. The pinned photodiode for an interline-transfer CCD image sensor. In *Proc. IEDM*, pages 28–31, 1984.

[33] E. R. Fossum and D. B. Hondongwa. A review of the pinned photodiode for CCD and CMOS image sensors. *IEEE Journal of the electron devices society*, 2(3):33–43, 2014.

[34] I. P. Clements, A. G. Gnade, A. D. Rush, C. D. Patten, M. C. Twomey, and A. V. Kravitz. Miniaturized LED sources for in vivo optogenetics experimentation. In *Proc. of SPIE*, volume 8586, 2013.

[35] T. Kim, J. McCall, Y. H. Jung, X. Huang, E. R. Siuda, Y. Li, J. Song, Y. M. Song, H. A. Pao, R. Kim, C. Lu, S. D. Lee, I. Song, G. Shin, R. Al-Hasani, S. Kim, M. P. Tan, Y. Huang, F. Omenetto, J. A. Rogers, and M. R. Bruchas. Injectable, cellular-scale optoelectronics with applications for wireless optogenetics. *Science*, 340:211–216, 2013.

[36] N. McAlinden, D. Massoubre, E. Richardson, E. Gu, S. Sakata, M. D. Dawson, and K. Mathieson. Thermal and optical characterization of micro-LED probes for in vivo optogenetic neural stimulation. *Optics letters*, 38(6):992–994, 2013.

[37] E. Stark, T. Koos, and G. Buzsàki. Diode probes for spatiotemporal optical control of multiple neurons in freely moving animals. *J. Neurophysiol.*, 108:349–363, 2012.

[38] A. Osman, J. H. Park, D. Dickensheets, J. Platisa, E. Culurciello, and V. A. Pieribone. Design constraints for mobile, high-speed fluorescence brain imaging in awake animals. *IEEE Transactions on biomedical circuits and systems*, 6(5):446–453, 2012.

[39] R. Y. Tsien. Fluorescent probes of cell signaling. *Ann. Rev. Neurosci.*, 12:227–253, 1989.

[40] E. F. Civillico and D. Contreras. Integration of evoked responses in supragranular cortex studied with optical recordings in vivo. *J. Neurophysiol.*, 96:336–351, 2006.

[41] J. H. Park, E. Culurciello, D. Kim, J. V. Verhangen, S. H. Gautam, and V. A. Pieribone. Voltage sensitive dye imaging system for awake and freely moving animals. In *IEEE Biomedical circuits and systems conference*, pages 2429–2432, 2008.

[42] Z. Han, L. Jin, J. Platisa, L. B. Cohen, B. J. Baker, and V. A. Pieribone. Fluorescent protein voltage probes derived from arclight that respond to membrane voltage changes with fast kinetics. *PLOS ONE*, 8(11), 2013.

[43] Aptina. *1/3-inch wide-VGA CMOS digital image sensor MT9V022, Rev. H 6/10 EN*, 2005.

[44] J. B. A. Maintz and M. A. Viergever. A survey of medical image registration. *Medical Image Analysis*, 2(1):1–36, 1998.

[45] L. G. Brown. A survey of image registration techniques. *ACM Computing Surveys*, 24(4):325–376, 1992.

[46] S. P. Kim and W. Su. Subpixel accuracy image registration by spectrum cancellation. In *Proc. ICASSP '93*, volume V, pages 153–156, 1993.

[47] B. Zitová and J. Flusser. Image registration methods: a survey. *Image and Vision Computing*, 21:977–1000, 2003.

[48] H. S. Stone, M. T. Orchard, E. Chang, and S. A. Martucci. A fast direct fourier-based algorithm for subpixel registration of images. *IEEE Transactions on geoscience and remote sensing*, 39(10):2235–2243, 2001.

[49] C. D. Kuglin and D. C. Hines. The phase correlation image alignment method. In *Proc. Int. Conf. on Cybernetics and Society*, pages 163–165, 1975.

[50] Q. Tian and M. N. Huhns. Algorighms for subpixel registration. *Computer Vision, Graphics and Image Processing*, 35:220–233, 1986.

[51] H. Shekarforoush, M. Berthold, and J. Zerubia. Subpixel image registration by estimating the polyphase decomposition of cross power spectrum. In *IEEE Computer Society Conference on Computer Vision and Pattern Recognition*, pages 532–537, 1996.

[52] H. Jia, N. L. Rochefort, X. Chen, and A. Konnerth. In vivo two-photon imaging of sensory-evoked dendritic calcium signals in coritcal neurons. *Nat. Protoc.*, 6(1):28–35, 2011.

[53] D. Smetters, A. Majewska, and R. Yuste. Detecting action potentials in neuronal populations with calcium imaging. *Methods*, 18:215–221, 1999.

[54] B. F. Grewe, D. Langer, H. Kasper, B. M. Kampa, and F. Helmchen. High-speed *in vivo* calcium imaging reveals neuronal network activity with near-millisecond precision. *Nat. Methods*, 7(5):399–405, 2010.

[55] J. MacQueen. Some methods for calssification and analysis of multivariate observations. In *Proceedings of 5th Berkeley Symposium on Mathematical Statistics and Probablity*, pages 281–297, 1967.

[56] S. P. Lloyd. Least squares quantization in pcm. *IEEE Transactions on Information Theory*, 28(2):129–137, 1982.

[57] C. M. Bishop. *Pattern recognition and machine learning*. Springer, 2006.

[58] I. Ozden, H. M. Lee, M. R. Sullivan, and S. S. H. Wang. Identification and clustering of event patterns from in vivo multiphoton optical recordings of neuronal ensembles. *J. Neurophysiol.*, 100:495–503, 2008.

[59] D. A. Dombeck, M. S. Graziano, and D. W. Tank. Functional clustering of neurons in motor cortex determined by cellular resolution imaging in awake behaving mice. *J. Neurosci.*, 29(44):13751–13760, 2009.

[60] D. Arthur and S. Vassilvitskii. k-means++: The advantages of careful seeding. In *Proceedings of the eighteenth annual ACM-SIAM symposium on Discrete algorithms*, pages 1027–1035, 2007.

[61] A. Coates and A. Y. Ng. Learning feature representations with k-means. In *Neural Networks: Tricks of the Trade*. Springer LNCS, 2012.

[62] S. Theodoridis and K. Koutroubas. *Pattern Recognition*. Academic Press, 1999.

[63] L. Vendramin, R. J. G. B. Campello, and E. R. Hruschka. On the comparison of relative clustering validity criteria. In *Proceedings of the 2009 SIAM International Conference on Data Mining*, pages 733–744, 2009.

[64] P. J. Rousseeuw. Silhouettes: a graphical aid to the interpretation and validation of cluster analysis. *Computational and Applied Mathematics*, 20:53–65, 1987.

[65] J. Dunn. Well separated clusters and optimal fuzzy partitions. *Journal of Cybernetics*, 4:95–104, 1974.

[66] J. C. Bezdek and N. R. Pal. Some new indexes of cluster validity. *IEEE Trans. Systems, Man and Cybernetics*, 28(3):301–315, 1998.

[67] D. L. Davies and D. W. Bouldin. A cluster separation measure. *IEEE Transactions on Pattern Analysis and Machine Intelligence*, 1(2):224–227, 1978.

[68] U. Maulik and S. Bandyopadhyay. Performance evaluation of some clustering algorithms and validity indices. *IEEE Transactions on Pattern Analysis and Machine Intelligence*, 24(12):1650–1654, 2002.

[69] T. H. Schwartz, D. Rabinowitz, V. Unni, V. S. Kumar, D. K. Smetters, A. Tsiola, and R. Yuste. Networks of coactive neurons in developing layer 1. *Neuron*, 20:541–552, 1998.

[70] A. Aguiló, T. H. Schwartz, V. S. Kumar, Z. A. Peterlin, A. Tsiola, E. Soriano, and R. Yuste. Involvement of cajal-retzius neurons in spontaneous correlated activity of embryonic and postnatal layer 1 from wild-type and reeler mice. *J. Neurosci.*, 19(24):10856–10868, 1999.

[71] A. V. Kravitz and A. C. Kreitzer. Striatal mechanisms underlying movement, reinforcement, and punishment. *Physiology*, 27:166–177, 2012.

[72] K. Nakano, T. Kayahara, T. Tsutsumi, and H. Ushiro. Neural circuits and functional organization of the striatum. *J Neurol*, 247(5 Supplement):V1–V15, 2000.

[73] C. Gerfen, R. Paletzki, and N. Heintz. Gensat bac cre-recombinase driver lines to study the functional organization of cerebral cortical and basal ganglia circuits. *Neuron*, 80(6):1368–1383, 2013.

[74] A. V. Kravitz, L. D. Tye, and A. C. Kreitzer. Distinct roles for direct and indirect pathway striatal neurons in reinforcement. *Nat. Neurosci.*, 15(6):816–819, 2012.

[75] N. D. Volkow and M. Morales. The brain on drugs: from reward to addiction. *Cell*, 162:712–725, 2015.

[76] A. V. Kravitz, B. S. Freeze, P. R. L. Parker, K. Kay, M. T. Thwin, K. Deisseroth, and A. C. Kreitzer. Regulation of parkinsonian motor behaviours by optogenetic control of basal ganglia circuitry. *Nature*, 466:622–626, 2010.

[77] G. Cui, S. B. Jun, X. Jin, M. D. Pham, S. S. Vogel, D. M. Lovinger, and R. M. Costa. Concurrent activation of striatal direct and indirect pathways during action initiation. *Nature*, 494(7436):238–242, 2013.

[78] B. S. Freeze, A. V. Kravitz, N. Hammack, J. D. Berke, and A. C. Kreitzer. Control of basal ganglia output by direct and indirect pathway projection neurons. *J. Neurosci.*, 33(47):18531–18539, 2013.

[79] R. L. Albin, A.B. Young, and J. B. Penney. The functional anatomy of basal ganglia disorders. *TINS*, 12(10):366–375, 1989.

[80] G. E. Alexander and M. D. Crutcher. Functional architecture of basal ganglia circuits: neural substrates of parallel processing. *TINS*, 13(7):266–271, 1990.

APPENDICES

A. NEURON CLUSTERS

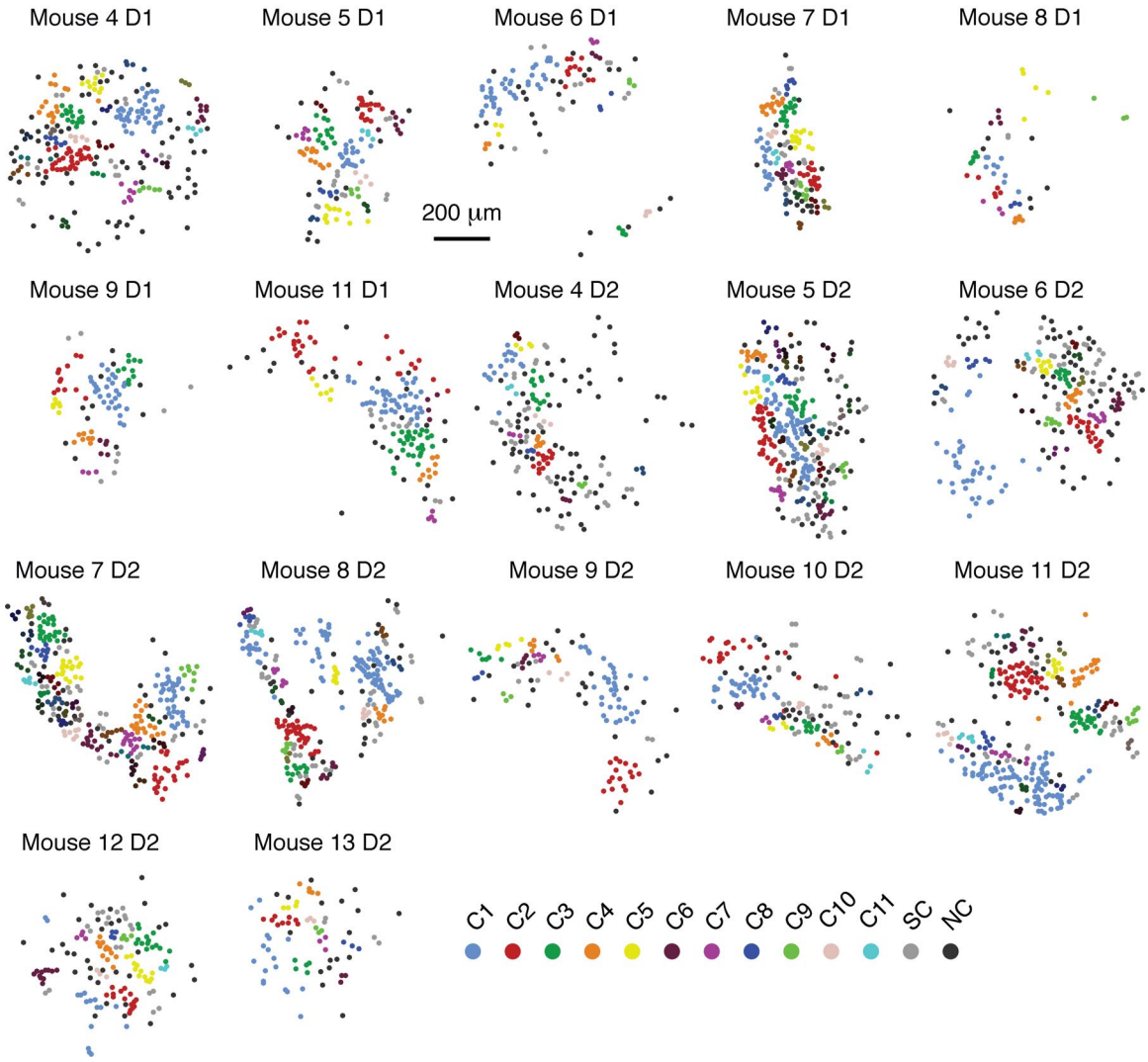

Figure A.1. Cell clustering based on calcium traces correlation for all D1 and D2 mice.

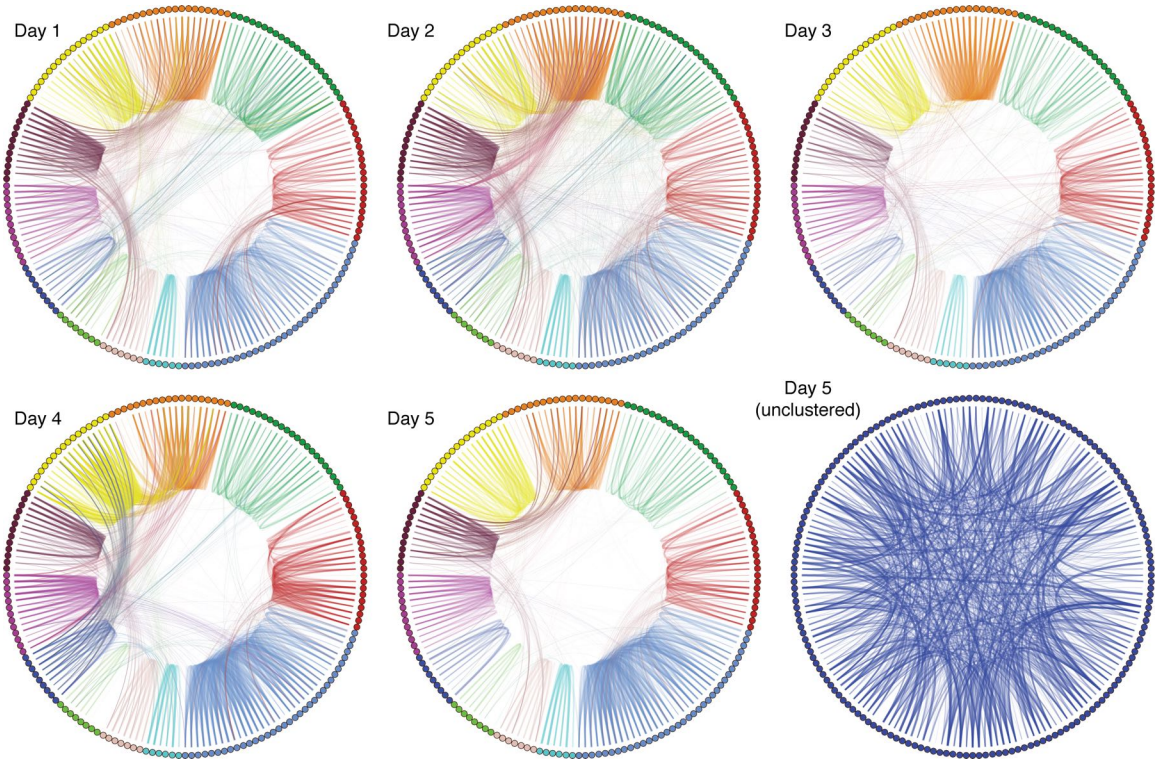

Figure B.1. The average Pearson's correlation coefficient between the calcium traces of all neurons within the largest 11 clusters for a D2 mouse: the intra-cluster correlation is the dominant component, and a weaker inter-cluster correlation varying from day to day is also observed. If the same neurons were not clustered, no clear correlation pattern would be detectable in this representation.

VITA

VITA

Giovanni Barbera received his B.S. degree and M.S. degree in Automation Engineering from University of Padova, Italy, and his Ph.D. degree in Mechanical Engineering from Purdue University. He is currently a visiting fellow at NIDA (Baltimore, MD), where he has been developing tools for in vivo, single cell resolution brain imaging. His research interests include the development of biomedical imaging tools for studying neural circuits, in conjunction with the application of machine learning techniques for data analysis and pattern recognition.